

# **Dynamics of microdroplets under oscillatory and quasi-static deformation**

by

Sanket Biswas

A THESIS SUBMITTED IN PARTIAL FULFILLMENT OF  
THE REQUIREMENTS FOR THE DEGREE OF  
MASTER OF APPLIED SCIENCE

in

The Faculty of Graduate and Postdoctoral Studies  
(Chemical and Biological Engineering)

THE UNIVERSITY OF BRITISH COLUMBIA  
(Vancouver)

December 2025

© Sanket Biswas, 2025

The following individuals certify that they have read, and recommend to the Faculty of Graduate and Postdoctoral Studies for acceptance, the thesis entitled:

Dynamics of microdroplets under oscillatory and quasi-static deformation

---

submitted by Sanket Biswas in partial fulfillment of the requirements for  
the degree of Master of Applied Science  
in Chemical and Biological Engineering

---

**Examining Committee:**

John M. Frostad, Associate Professor, Chemical & Biological Engineering and Food Science, UBC  
*Supervisor*

Gwynn J. Elfring, Associate Professor, Mechanical Engineering and Mathematics, UBC  
*Co-supervisor*

James J. Feng, Professor, Chemical & Biological Engineering and Mathematics, UBC  
*Supervisory Committee Member*

Anthony Wachs, Professor, Chemical & Biological Engineering and Mathematics, UBC  
*Supervisory Committee Member*

# Abstract

Soft microparticles are deformable (“squishy”) microscale entities that are ubiquitous in nature and technology. Unlike macroscopic particles, the force response of microparticles under external loading depends on both bulk material properties and interfacial tension, allowing force measurements to probe these properties. Traditional devices such as the biomembrane force probe, optical and magnetic tweezers, the atomic force microscope and the microcantilever tensiometer each have limitations in force range, accessible particle size, reliability of attachment, or commercial availability. Consequently, even simple microparticle subclasses such as Newtonian and viscoelastic microdroplets remain challenging to characterize accurately at the single-particle level.

The cantilevered capillary force apparatus (CCFA) overcomes these limitations by fixing soft microparticles via capillary rim pinning or gentle suction, imposing controlled quasi-static or oscillatory deformations and resolving the resulting forces with high accuracy. However, analytical frameworks for interpreting CCFA force signals and inferring material properties under these deformations have been lacking. To address this, we first perform a small-strain regular perturbation expansion of the Young–Laplace equation, the force response, and the bridge volume-conservation constraint to obtain the leading nonlinear force and shape of an initially spherical Newtonian microdroplet quasi-statically deformed while pinned between two coaxial substrates. Comparison with numerical solutions demonstrates excellent agreement and substantially extends the range of validity of earlier analytical models, enabling accurate interfacial tension measurements over a wider range of deformations.

Second, we develop an asymptotic model for the small-strain oscillatory deformation of an initially cylindrical Maxwell viscoelastic microdroplet pinned between two coaxial substrates. Regular perturbation in strain amplitude and aspect ratio gives a force response with a static capillary part and a dynamic part comprising in-phase contributions from bulk elasticity and interfacial curvature, and an out-of-phase contribution from bulk viscosity. In time-resolved CCFA measurements, the force offset yields the interfacial tension, while the amplitude and phase lag yield the storage and loss moduli. Together, these models provide a unified analytical framework for extracting interfacial and bulk material properties of single microdroplets using the CCFA, and they can be extended to more complex soft microparticles and related instruments.

# Lay summary

Soft microparticles are tiny, squishy entities found in foods, drug formulations, and nature. How much force they exert under gentle loading depends on their bulk and interfacial material properties, so precise force measurements can reveal those properties. Traditional instruments struggle to handle such small, highly deformable particles. To address this, we develop mathematical models for a specialized device called the cantilevered capillary force apparatus (CCFA), which gently stretches or oscillates single microparticles and accurately measures the resulting force. For simple (viscous) microdroplets under gentle stretching, the first model shows how interfacial tension can be extracted from the force signal over moderate strains. For complex (viscoelastic) microdroplets under oscillatory squeezing, the second model shows how bulk viscosity, elasticity, and interfacial tension can all be extracted from the force signal. Together, these models provide a unified framework for characterizing single microdroplets using the CCFA, and can be extended to more complex microparticles.

# Preface

The research presented in this thesis was conducted by the author, Sanket Biswas, under the joint supervision of Professor John M. Frostad and Professor Gwynn J. Elfring. Publication plans are as follows:

- A manuscript based on Chapter 2, provisionally entitled *A second-order asymptotic theory for the nonlinear quasi-static deformation of axisymmetric capillary bridges*, is in preparation for submission to a peer-reviewed journal. The submitted version may include an additional major section that is in progress and not included in this thesis. The author developed the analytical and numerical models and drafted the manuscript. Professors J. M. Frostad and G. J. Elfring jointly supervised the research and contributed to its analysis and revision. The additional section, if included, will follow the same division of responsibilities.
- A manuscript based on Chapter 3, provisionally entitled *A theory for characterizing the bulk rheology and interfacial tension of viscoelastic microdroplets under oscillatory deformation*, is in preparation for submission to a peer-reviewed journal. The author developed the analytical model and drafted the manuscript. Professors J. M. Frostad and G. J. Elfring jointly supervised the research and contributed to its analysis and revision.

Generative artificial intelligence (GenAI) tools were used in a limited way in preparing this thesis. Specifically, ChatGPT (OpenAI) was used as a writing assistant to improve phrasing, grammar, and overall clarity in selected sections of the thesis. All scientific ideas, mathematical derivations, modeling, data analysis, coding, and figure preparation are the author's own work, and any GenAI-generated suggestions were critically reviewed, edited, and integrated by the author. No GenAI tools were used to generate or analyze research data or to draw scientific conclusions.

# Table of contents

<b>Abstract</b> . . . . .	iii
<b>Lay summary</b> . . . . .	iv
<b>Preface</b> . . . . .	v
<b>Table of contents</b> . . . . .	vii
<b>List of figures</b> . . . . .	viii
<b>Acknowledgements</b> . . . . .	xi
<b>Dedication</b> . . . . .	xiii
<b>1 Introduction</b> . . . . .	1
<b>2 A second-order asymptotic theory for the nonlinear quasi-static deformation of axi-symmetric capillary bridges</b> . . . . .	7
2.1 Introduction . . . . .	7
2.2 Problem setup . . . . .	10
2.3 Non-dimensionalization and asymptotic analysis . . . . .	15
2.4 Results and discussion . . . . .	17
2.4.1 Force response . . . . .	19
2.4.2 Mean curvature and pinning angle . . . . .	25
2.4.3 Bridge shape . . . . .	27
2.4.4 Limitations . . . . .	31
2.5 Conclusions . . . . .	31
2.5.1 Key findings . . . . .	31
2.5.2 Future directions . . . . .	32
<b>3 A theory for characterizing the bulk rheology and interfacial tension of viscoelastic microdroplets under oscillatory deformation</b> . . . . .	33
3.1 Introduction . . . . .	33
3.2 Problem setup . . . . .	36
3.3 Analytical framework . . . . .	39
3.3.1 Non-dimensionalization . . . . .	39
3.3.2 Asymptotic analysis and anatomy of the interfacial stress balance . . . . .	41
3.3.3 Post-transient response . . . . .	45
3.4 Results and discussion . . . . .	47
3.4.1 Validation . . . . .	47

3.4.2	Determination of the material properties . . . . .	48
3.4.3	Limitations . . . . .	49
3.5	Conclusions . . . . .	51
3.5.1	Key findings . . . . .	51
3.5.2	Future directions . . . . .	52
<b>4</b>	<b>Conclusions . . . . .</b>	<b>54</b>
4.1	Key findings . . . . .	55
4.2	Limitations . . . . .	56
4.3	Future directions . . . . .	58
<b>Bibliography</b>	. . . . .	<b>59</b>
<b>Appendices</b>	. . . . .	<b>73</b>
<b>A</b>	<b>Asymptotic expansion of the interface mean curvature</b>	<b>74</b>
<b>B</b>	<b>Validity of the bridge volume conservation constraint</b>	<b>76</b>
B.1	Pinned droplet case . . . . .	76
B.2	Constant capillary suction pressure case . . . . .	78

# List of figures

1.1	(a) Schematic of the cantilevered capillary force apparatus (CCFA). A <i>rigid capillary</i> is positioned opposite a second capillary bent at 90° near its tip, referred to as the <i>cantilevered capillary</i> . (b) Close-up photograph of the capillaries. The rigid capillary has an outer diameter of 360 $\mu\text{m}$ and the cantilevered capillary 150 $\mu\text{m}$ ; the inner diameters at which the particle is pinned or aspirated remain the same (50 $\mu\text{m}$ ). The motion of the cantilever is tracked by reflecting a laser off a mirror attached to it and monitoring the beam position digitally. Adapted from Frostad et al. [1]. . . . .	2
2.1	(a) Schematic of an undeformed (spherical) microdroplet (or microbubble) of radius $R_d$ pinned at equilibrium at the rims of coaxial capillaries of inner radius $R = 10\text{--}100 \mu\text{m}$ . (b) and (c) The capillaries are quasi-statically displaced by $\Delta L/2$ in opposite directions from this initial state, dilating the droplet [(b) $\Delta L > 0$ ] or compressing it [(c) $\Delta L < 0$ ], and the system is allowed to reach a new equilibrium. . . . .	11
2.2	(a) Dimensionless force response $\hat{F} = F/(2\pi\gamma R_d)$ versus displacement $\varepsilon = \Delta L/R_d$ (bottom axis) and strain $\bar{\varepsilon} = \Delta L/L_0$ (top axis) for capillary radius $\hat{R} = R/R_d = 0.45$ . The numerical Young–Laplace solution ( <i>solid red</i> ) is compared with the linear model of Kusumaatmaja and Lipowsky [2] ( <i>blue dashed</i> ), the quadratic model of Sariola [3] ( <i>orange dash-dot</i> ), and the present second-order asymptotic approximation ( <i>magenta open circles</i> ). Curves are shown up to the compression limit ( $\theta = 180^\circ$ ) and to the onset of dilation where the present model departs from the numerical solution. (b) Numerical $\hat{F}$ plotted against $\varepsilon$ across the CCFA-relevant range: $\hat{R} \in \{0.3, 0.4, 0.5, 0.6\}$ ( <i>solid lines, distinct colours</i> ), overlaid with <i>matching-colour open circles</i> from the present asymptotic model. Truncation limits as in panel (a). . . . .	19
2.3	(a,b) Dimensionless displacement $\varepsilon = \Delta L/R_d$ at which the % relative error between the analytical models and the numerical solution, $100 \times  \hat{F}_{\text{analytical}}/\hat{F}_{\text{numerical}} - 1 $ , reaches a fixed threshold, plotted against capillary radius $\hat{R} = R/R_d$ . (a) Dilation threshold 2%; (b) compression threshold 1%. Models: Kusumaatmaja and Lipowsky [2] ( <i>blue squares</i> ), Sariola [3] ( <i>orange triangles</i> ), present second-order asymptotic model ( <i>magenta open circles</i> ); <i>solid lines (with colours matching the markers)</i> are quadratic fits. The capillary radius is varied over the CCFA-relevant range $\hat{R} \in [0.3, 0.6]$ . The chosen error thresholds correspond to the smallest values for which all models yield consistent, non-fluctuating trends across the entire radius range. The black dashed line in panel (b) indicates the point of maximum compression ( $\theta = 180^\circ$ ). . . . .	20

- 2.4 (a) Log–log plot of the absolute error between the analytical models and the numerical solution versus displacement  $\varepsilon$  during dilation for capillary radius  $\hat{R} = R/R_d = 0.45$ . Models: Kusumaatmaja and Lipowsky [2] (*blue squares*), Sariola [3] (*orange triangles*), and the present quadratic model (*magenta circles*). Linear fits (*black solid line*) to the error curves over the range  $\varepsilon \in [0.15, 0.3]$  for the first two models yield slopes of 2.00 and 2.01, respectively. For the present model, the linear fit over the range  $\varepsilon \in [0.5, 0.8]$  (where the errors stabilize) yields a slope of 3.47. (b) Error between the present model and the numerical model, normalized by  $\varepsilon^3$ , plotted versus  $\hat{R}$  for  $\varepsilon = 0.6$  (*circles*), 0.7 (*squares*), and 0.8 (*triangles*). Data points collapse onto a single quadratic fit (*black solid line*):  $2.496\hat{R}^2 - 1.527\hat{R} + 0.248$ . . . . .

2.5 (a) First- (linear) and second-order (quadratic) coefficients of the regular perturbation expansion for the dimensionless force response  $\hat{F}$ , denoted  $\hat{F}_1$  (*blue dashed*) and  $\hat{F}_2$  (*magenta solid*), plotted versus capillary radius  $\hat{R} \in [0, 1]$  [bottom axis] and the corresponding zero-force pinning angle  $\theta_0$  (top axis). Also shown is the quadratic coefficient of Sariola [3] (*orange dash-dot-dash*), given by  $-k_2/(2\pi\gamma/R_d)$ . (b) Absolute normalized error between the present analytical model and the numerical solution,  $|(\hat{F}_{\text{analytical}} - \hat{F}_{\text{numerical}})/\varepsilon^3|$ , plotted versus the absolute displacement  $|\varepsilon| = |\Delta L/R_d|$  for dilation (*circles*) and compression (*triangles*) at the CCFA mean radius  $\hat{R} = 0.45$ . *Solid lines (with colours matching the markers)* are linear fits. The *vertical black dotted line* marks the absolute displacement at the maximum compression limit ( $\theta = 180^\circ$ ). . . . .

2.6 (a) Numerical profiles of the dimensionless mean curvature  $\hat{\mathcal{H}} = R_d\mathcal{H}$  versus displacement  $\varepsilon = \Delta L/R_d$  for capillary radii  $\hat{R} \in \{0.3, 0.4, 0.5, 0.6\}$  (*solid lines, distinct colours*), spanning the CCFA-relevant range. Corresponding present asymptotic model curves are overlaid as *matching-colour open circles*. Curves are shown up to the compression limit ( $\theta = 180^\circ$ ) and to the dilation range beyond which the asymptotic model deviates from the numerical solution. (b) The same comparison is presented for the pinning angle  $\theta$  (in degrees) plotted versus  $\varepsilon$ , using the same line/marker conventions. . . . .

2.7 Normalized error between second-order asymptotic predictions and numerical results for (a) the mean curvature and (b) pinning angle, plotted versus capillary radius  $\hat{R} = R/R_d$  for displacements  $\varepsilon = 0.6$  (*circles*), 0.7 (*squares*), and 0.8 (*triangles*). Errors are normalized by  $\varepsilon^3$ . In both panels, the data collapse onto a single quadratic fit (*black solid line*), consistent with cubic error scaling in displacement. Fitted curves: mean curvature  $-0.095\hat{R}^2 + 0.023\hat{R} - 0.025$ ; pinning angle  $1.246\hat{R}^2 - 0.956\hat{R} + 0.252$ . . . . .

2.8 Comparison of bridge profiles  $\hat{\mathcal{R}}(\hat{z})$  from the numerical solution (*red solid*) and the second-order asymptotic expansion (*thick orange solid*) as the droplet evolves from the undeformed state [panel (c)] to maximum compression ( $\theta = 180^\circ$ ) [panel (a)] and to an equally dilated state [panel (e)]. The capillary radius selected is  $\hat{R} = 0.45$ , representative of the CCFA-relevant range  $\hat{R} \in [0.3, 0.6]$ . The absolute displacement between adjacent equilibrium states is fixed at  $|\Delta\varepsilon| = 0.17$ . For each panel, the corresponding pinning angle  $\theta$ , force response  $\hat{F}$ , and displacement  $\varepsilon$  are listed at the top of each panel for reference. . . . .

2.9 Comparison of numerical (*red solid*) and analytical (*thick orange solid*) bridge profiles for capillary radii  $\hat{R} \in \{0.3, 0.4, 0.5, 0.6\}$  at fixed force magnitude:  $\hat{F} = -0.10$  during dilation [panels (a) to (d)] and  $\hat{F} = 0.10$  during compression [panels (e) to (h)]. The capillary radius  $\hat{R}$ , pinning angle  $\theta$ , and displacement  $\varepsilon$  are indicated at the top of each panel for reference. . . . .



# Acknowledgements

When I arrived at UBC in fall 2023, fresh from my undergraduate degree, I had some prior research experience in theoretical fluid mechanics and applied mathematics through short-term internships. Those projects gave me the impression that being a “good” theorist meant cranking through complicated mathematics as quickly as possible to get the “right” answer, without worrying too much about whether the underlying physics really made sense. Whenever I presented my work—whether as a paper, poster, or talk—I would pack in long derivations and feel proud of that, even though I often lost the audience along the way. In short, I believed that theoretical research in fluid mechanics and, more broadly, transport processes, was mostly about mathematics, with physics coming second.

I am deeply grateful to my advisors, Prof. Gwynn J. Elfring and Prof. John M. Frostad, for transforming that view over the past two years. From them I learned that good theory starts with careful physical reasoning and only then moves to the advanced mathematics needed to support and sharpen that intuition, a lesson I will carry throughout my academic career. Gwynn’s graduate fluid mechanics course, the clarity and structure of his lectures and talks, and his detailed feedback on my writing have set the standard for how I hope to learn and communicate science. John’s perspective as an experimentalist pushed me to explain my mathematical results in simple, concrete physical terms and to develop better habits for documenting my work and using a clear, reusable structure when presenting it. Together they helped me grow from an enthusiastic undergraduate into a more independent and well-rounded researcher, and I am genuinely thankful for the chance to be their graduate student and to keep drawing on their lessons.

I would also like to sincerely thank my supervisory committee members, Prof. James J. (Jimmy) Feng and Prof. Anthony Wachs, for their support and thoughtful input at many stages of my time at UBC. Their comments on my thesis and the deep scientific questions they raised during my defense were crucial in polishing this final version. Working closely with Jimmy as a graduate teaching assistant (GTA) for his undergraduate numerical methods course showed me how much care and empathy he brings to teaching, and his sharp, fundamental questions in the weekly Fluids seminar set a standard I aspire to follow in my own research. Anthony’s graduate numerical methods course played a key role in shaping the numerical part of the first project in this thesis; its structure—weekly assignments, a mini-project, a presentation, and peer review—was an excellent model for training graduate students, and his dedication to teaching has given me tools I will rely on in both research and teaching. I am also grateful to Prof. Mark Martinez, whose graduate transport phenomena course broadened my view of transport processes and with whom I later worked as a GTA for the undergraduate version, and to Prof. Neil Balmforth, whose course on asymptotic analysis and perturbation methods provided much of the mathematical backbone for this thesis.

One of the most rewarding and perhaps underrated parts of my MASc journey has been the people I shared it with in the lab (CEME 1051). I am especially grateful to Dr. Mouad Boudina and Dr. Jiahao Gong, whose mentorship and friendship continued even after they graduated, and to Dr. Zhouyang Ge, from whom I learned a great deal through his scientific insights and broader perspectives. Long late-night study sessions with Xudong Yuan while we were both taking Gwynn’s

fluid mechanics course made a demanding first semester much more manageable. I am also thankful to Dr. Guodong Gai for the relaxed conversations and jokes that helped balance intense research days. When Ricardo Tavares Domingos, the newest member of our group, joined the lab it felt more lively, and our many conversations—especially about football (soccer)—along with his grit and dedication to research were a constant source of energy and inspiration.

I am especially thankful to my dear friend Yeganeh Moussavi, who stood by me through the ups and downs of my time at UBC and whose kindness and resilience were a constant source of strength. My roommate, Ripudaman Singh, was another huge support—from listening to endless research rants to sharing long hikes, spontaneous trips around Vancouver, and deep conversations about politics and science. Reuniting with my high school friend Souptik Mudi at UBC was an unexpected gift; his support and sense of humour—from Tim Hortons coffee chats to our long snowy hike in Pacific Spirit Park—made life much lighter. I would also like to thank Ritu Thombre for her friendship and many coffee chats filled with discussions about academia, inclusivity, and science memes. I am also grateful to Niloofar Taleghani and Dr. Layal Jbara, whom I met while working as a GTA for the undergraduate numerical methods course in my final term; we quickly became close friends through our shared experience as international students in the same department, and the warm farewell they gave me before I moved to Berkeley was deeply meaningful. Without these people, surviving in Vancouver—let alone focusing on and enjoying research—would have been much harder.

I would also like to thank my other lab colleagues—Dr. Yun-Han Huang, Lanxin Mo, Cheng-hao Li, Alice Tong, Julianne Clark, Lily Santos O’Keefe, Yash Mali, and Bofan Chen—for their thoughtful feedback during group meetings and for being such supportive labmates, as well as all the members of Prof. Frigaard’s group for sharing space and helping create a welcoming, collegial environment over the past two years. Among them, I especially want to acknowledge Fatemeh Bararpour, whose consistency, work ethic, and dedication as a PhD student were truly inspiring, and Yosef Rezaei, whose regular check-ins and stories brought a lot of warmth and humour into the workspace. The CHBE Graduate and Undergraduate Office staff—Marlene Chow, Kristi Chow, Enpei Hsu, and Brittany Ji—also deserve special thanks for handling so much administrative work behind the scenes for both my studies and my GTA duties, which made my life much easier and kept everything running smoothly. I would also like to thank the many undergraduate students I have taught and interacted with as a GTA; I have learned a great deal from them, and our discussions were often very insightful.

I want to express my heartfelt thanks to my childhood friends—Swapnil Maiti and Ronak Singha—and to my undergraduate friends—Harshita Tiwari, Pradumn Kumar, Pramod Kumar, Sushant Kumar, and Piyush Gupta—who have been constant, irreplaceable parts of my life. I am also thankful to Shivanshi Tiwari, Harshita’s elder sister and a physics PhD student at the University of Rochester, and to my junior from my undergraduate program, Neharika Puri, for regularly checking in on me and offering steady encouragement. Above all, I am most grateful to my parents, whose love, encouragement, and unwavering support have carried me through this chapter and every one before and after it. Our daily calls—no matter how busy they are or when I am calling—have been an anchor and source of energy for me; those 30–35 minutes of talking while I walk home from university or cook dinner keep me going, and I genuinely would not have reached this point without them.

To conclude, I gratefully acknowledge the financial support of the Mitacs Globalink Graduate Fellowship, the Tri-Agency (NSERC, CIHR, and SSHRC), and UBC, which together funded my studies, research, and living expenses during this degree. Their support allowed me to focus on learning and research without constant financial stress, and without it this thesis would quite literally not exist.

# Dedication

*To my family for their unwavering love and support,  
to my friends who stood by me through highs and lows,  
and to my mentors who believed in me and welcomed me into the scientific community.*

# Chapter 1

## Introduction

Soft microparticles are deformable (or *squishy*) entities with typical sizes between 10 µm and 1 mm [4, 5]. They are ubiquitous in nature and industry, appearing either as isolated inclusions or as constituents of dense multiphase materials. Representative isolated examples include biological cells [6], vesicles [7], and polymeric or protein microgels [8]; embedded examples include emulsion droplets and bubbles in food products [9], personal-care formulations [10], coatings [11], and printing inks [12]. Under external mechanical loading, the (normal) force exerted by the particle on the loading surfaces, often referred to as the *force response*, is governed not only by bulk stresses set by the particle’s rheology, as in macroscopic particles, but also by capillary stresses arising from interfacial tension  $\gamma$  [13, 14].

This follows from the fact that capillary stresses scale as  $\gamma/R_d$ , where  $R_d$  is the characteristic particle size, and hence they typically become comparable to, or dominant over, bulk contributions at micrometer scales [15, 16]. Moreover, under typical controlled loadings at these length scales, inertial and gravitational forces of both the particle and the ambient fluid are vanishingly small compared to bulk and interfacial stresses, and thus have negligible influence on the dynamics [17, 18]. These fundamental yet subtle distinctions between soft microparticles and their macroscopic counterparts have motivated extensive studies since the mid-1990s on their mechanical behaviour under different types of loading [1, 13, 19–25].

A natural question, then, is why this succession of studies has addressed the mechanical behaviour, or force response, of a soft microparticle under different loading protocols—for example, step [26], uniaxial [27], quasi-static [2], or oscillatory [13]. Broadly, these studies have pursued two complementary motivations, sometimes one, sometimes both. The first is purely mechanistic: to understand how, under a given controlled loading, bulk rheological stresses couple with capillary stresses to produce the observed deformation and measured force response.

The second follows directly from the first and stems from the fact that the material properties of a clean-interface (free of surface active agents or surfactants) microparticle, namely its bulk rheology and interfacial tension, regulate its transport and deformation at the single-particle scale and, when present in ensembles, govern the stability and texture of the host multiphase material. Thus, to advance our understanding of single-particle behaviour and to enable optimization of the macroscopic properties of multiphase products, it is essential to devise methods that disentangle the material properties from the measured force response. Detailed accounts of these two complementary aspects are given in the reviews by Liu [28] and Kim and Lee [5].

From the wide array of soft microparticles outlined above, the mechanical behaviour of even the simplest subclasses—purely viscous (Newtonian) microdroplets [29, 30] and viscoelastic microdroplets [31–34]—remains poorly understood at the single-particle scale, both theoretically and experimentally. This stands in sharp contrast to their macroscopic counterparts, whose behaviour

has been extensively characterized [14, 31, 35–38]. The primary obstacle has been the absence of experimental apparatus capable of perturbing microparticles while accurately resolving their force response, which typically lies between 1 nN and 1 mN.

Traditional devices—such as compressional rheometers [39, 40], uniaxial compression testers [41–44], the micro-Fourier rheometer (MFR) [45], filament stretching rheometers (FiSER) [46], capillary breakup extensional rheometers (CaBER) [47–50], rotational shear rheometers [36, 51–54], squeeze flow rheometers (SFR) [36, 51–54], and oscillatory squeeze flow rheometers (OSFR) [37, 55–60]—are designed primarily for probing macroscopic samples of size  $\sim 1\text{--}10\text{ mm}$ . Other instruments, such as pendant- or spinning-drop tensiometers [61–63], bicone or magnetic-needle interfacial shear rheometers [64–68], and interfacial dilatational rheometers (IDR) [69, 70], are restricted to measuring properties of fluid-fluid interfaces alone thus cannot provide information on the bulk rheology (or the combined force response of the particle). Comprehensive reviews of these and related techniques can be found in Drellich et al. [71], Fuller and Vermant [72], Sagh and Fischer [73], and Jaensson et al. [74]. Finally, techniques such as the biomembrane force probe [19, 75], the surface force apparatus (SFA) [76, 77], and optical or magnetic tweezers [78, 79] were developed primarily for particles of size  $\lesssim 10\text{ }\mu\text{m}$ , rendering them unsuitable for most soft microparticles of interest.

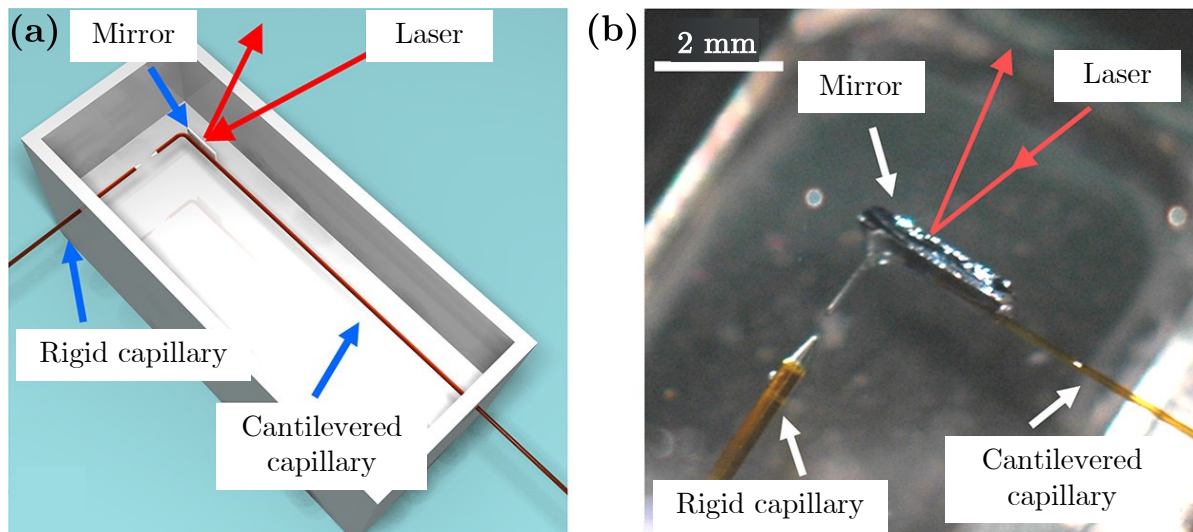


**Figure 1.1:** (a) Schematic of the cantilevered capillary force apparatus (CCFA). A *rigid capillary* is positioned opposite a second capillary bent at  $90^\circ$  near its tip, referred to as the *cantilevered capillary*. (b) Close-up photograph of the capillaries. The rigid capillary has an outer diameter of  $360\text{ }\mu\text{m}$  and the cantilevered capillary  $150\text{ }\mu\text{m}$ ; the inner diameters at which the particle is pinned or aspirated remain the same ( $50\text{ }\mu\text{m}$ ). The motion of the cantilever is tracked by reflecting a laser off a mirror attached to it and monitoring the beam position digitally. Adapted from Frostad et al. [1].

To address the lack of practical apparatus capable of probing soft microparticles and measuring their small force responses with high accuracy, Frostad et al. [1] introduced the cantilevered capillary force apparatus (CCFA). The CCFA is inspired by the designs and operating procedures of the micropipette tensiometer [24, 80, 81], the microcantilever tensiometer developed by Moran et al. [20], the series of micromanipulation techniques pioneered by Zhang and coauthors [82–84], and colloidal-probe atomic force microscopy (AFM) [21, 85, 86]. However, it mitigates several practical limitations: fragility, operational difficulty, and limited replicability in the first three methods, and the difficulty of reliably attaching such highly deformable particles to the flat or sharpened tip of the AFM cantilever (often requiring fixation to a planar substrate and pre-stressing). As illustrated in

Fig. 1.1, the CCFA employs two coaxial borosilicate capillaries: one rigid (the *rigid capillary*) and the other acting as a calibrated cantilever (the *cantilevered capillary*). A particle of size between 10  $\mu\text{m}$  and 1 mm is pinned or gently aspirated (via suction) between the two capillaries, and laser interferometry resolves cantilever deflections to nanometer precision, enabling force measurements spanning 1 nN to 1 mN.

A distinctive feature of the CCFA is its versatility: it can probe not only Newtonian and viscoelastic microdroplets subjected to quasi-static, oscillatory, or uniaxial deformations [1, 25, 87], but also more complex microparticles. Examples include microgels [88–90], which exhibit *poroviscoelasticity* by coupling fluid flow through a porous elastic network [91, 92]; core–shell microcapsules with elastic and/or viscous cores enclosed by one or more membranes with similar behaviours [25, 87, 93, 94]; neurospheres, which are multicellular neural spheroids behaving as (active) poroviscoelastic tissues with an effective tissue surface tension [95, 96]; and particles with surfactant-laden interfaces [15, 72, 97–99].

However, as with most rheometers and tensiometers, the CCFA measures only the force response directly, either as a function of time or of the imposed capillary displacement. To extract bulk and interfacial material properties, analytical or numerical models are required to relate the measured force response to the underlying coupling between bulk rheological stresses, interfacial stresses, ambient fluid stresses, and the resulting particle deformation. Such models are also essential for validating the accuracy of CCFA measurements. Yet, given that the CCFA is a relatively young apparatus (introduced just over a decade ago), comprehensive models remain undeveloped for most of the deformation protocols listed above, even for the simplest microparticles.

Motivated by the lack of analytical frameworks to model the behaviour of even the simplest microparticles—namely Newtonian and viscoelastic microdroplets—under different deformations in the CCFA, this thesis seeks to address this gap by posing and answering the following fundamental questions. (i) For a Newtonian microdroplet pinned at the rims of two coaxial capillaries (or circular substrates) of equal radii, quasi-statically displaced from its undeformed (spherical) state by moving the rigid capillary by  $\Delta L$  (or displacing both substrates mirror-symmetrically by  $\Delta L/2$ ), i.e., maintaining equilibrium at each displacement so that all bulk viscous stresses have dissipated, can we develop an analytical framework that predicts the droplet force response (on the cantilevered capillary or one of the substrates) and shape at arbitrary displacements, and thereby recover its constant interfacial tension  $\gamma$  (assuming a surfactant-free interface with the ambient fluid)?

For typical microdroplets of undeformed radius  $R_d$ , gravitational forces are negligible compared with capillary forces since the Bond number  $\text{Bo} = \Delta\rho g R_d^2 / \gamma \sim \Delta\rho g R^2 / \gamma \sim 10^{-5}\text{--}10^{-3} \ll 1$ . Here,  $R \sim R_d$  is the capillary/substrate radius,  $\Delta\rho = \rho - \rho_a$  is the density difference between the droplet and the ambient fluid, and  $g$  is gravitational acceleration. Consequently, the dynamics remain unaltered whether the substrates are aligned parallel to gravity (as in most macroscopic rheometers and in AFM) or perpendicular to it (as in the micro-cantilever tensiometer or the CCFA).

(ii) In the same configuration, if the Newtonian droplet is replaced by a viscoelastic one initially pinned in a cylindrical configuration, and one substrate (or the rigid capillary) is oscillated about this position while the force response is recorded on the fixed substrate (or cantilevered capillary)—as in the OSFR and related macroscopic rheometers capable of oscillatory perturbations such as the compressional rheometer, MFR, and FiSER—can we develop an analytical framework that predicts the droplet’s oscillatory force response and shape, and thereby recovers both its interfacial tension  $\gamma$  and its bulk viscosity and elasticity?

Question (i) has been partially addressed by the theory of Kusumaatmaja and Lipowsky [2], which predicts the force response  $F$  as a function of the displacement  $\Delta L$  from the undeformed spherical state, but only in the small-displacement regime,  $|\Delta L| \lesssim 0.1R_d$ , wherein  $F$  varies linearly with  $\Delta L$ . They showed that the proportionality (spring) constant of the linear force–displacement

curve depends solely on the undeformed pinning angle  $\theta_0$ , and validated this prediction using numerical solutions obtained with the Surface Evolver package [100, 101]. Here, in the limit  $Bo \ll 1$ , the droplet shapes attained at each displacement are governed by the axisymmetric Young–Laplace equation [16, 17], which admits as solutions the family of axisymmetric constant-mean-curvature (CMC) surfaces, commonly referred to as *Delaunay surfaces* [102, 103]. In this case, the force exerted by the droplet on either capillary rim plane (or equivalently, on either circular substrate) is the sum of two contributions: the Laplace pressure jump across the droplet–ambient fluid interface acting over the rim area, and the normal line tension with which the droplet attracts the capillaries (or substrates) along the rim perimeter. Importantly, this force response is spatially uniform across any cross-section of the droplet bridge, i.e., the force transmitted across one portion of the droplet to another remains constant along the bridge [103, 104].

However, once the small linear regime of the force–displacement curve is exceeded, the response becomes nonlinear, and capturing this behaviour—and validating CCFA measurements in this regime—requires solving the full nonlinear Young–Laplace boundary-value problem at each prescribed displacement [20, 100, 101, 105, 106]. While numerically tractable, such calculations remain cumbersome for routine experimental analysis in the CCFA. A closed-form analytical expression that captures the leading-order nonlinear force response would therefore be of substantial practical value, as it would both reveal the essential physical trends and facilitate CCFA-based measurements in this regime.

Beyond this leading-order nonlinear correction, further analytical progress becomes algebraically unwieldy and is unlikely to provide additional physical insights, rendering numerical solutions the preferred route. The only prior analytical effort in this direction is the quadratic force–displacement model of Sariola [3], obtained via a second-order Taylor expansion of the force response in  $\Delta L$  about the undeformed (zero-force) state. While their first-order coefficient correctly recovers the linear spring constant derived by Kusumaatmaja and Lipowsky [2], the second-order term fails to account for key shape-mediated contributions and therefore does not capture the leading nonlinear behaviour accurately.

In Chapter 2, we address this limitation by deriving second-order asymptotic expansions not only for the force response in terms of the dimensionless displacement  $\varepsilon = \Delta L/R_d$ , but also for the mean curvature and the pinning angle. These expansions, in turn, allow us to obtain second-order approximations for the shape of the microdroplet. In each case, the coefficients depend solely on the zero-force pinning angle  $\theta_0$ . Comparison with numerical solutions of the full Young–Laplace boundary-value problem shows excellent agreement across the range of capillary radii relevant to the CCFA, for both compression and dilation. Our model further captures the nonlinear trend whereby the incremental force required to displace a droplet between successive equilibrium states increases under compression and decreases under dilation, with the magnitude of this incremental force growing with capillary radius. Thus, this work provides the first closed-form analytical description of the leading-order nonlinear behaviour of not only the droplet–CCFA system, but of any axisymmetric capillary bridge with fixed contact lines under quasi-static deformation, requiring only the initial pinning angle  $\theta_0$  or, equivalently, the capillary-to-droplet radius ratio  $R/R_d$  as input.

Next, to elaborate Question (ii), we aim to develop an analytical framework that prescribes a procedure for extracting the intrinsic material properties of a viscoelastic microdroplet—namely, the zero-shear viscosity  $\mu_0$ , infinite-frequency modulus  $G_0$ , and relaxation time  $\lambda$ —from its oscillatory force response. This setup is analogous to the operating principle of the OSFR and related macroscopic rheometers capable of operating in the same manner [37, 55, 58]. The key distinction, however, is that such rheometers are designed exclusively for macroscopic droplets and cannot resolve the sensitive force responses characteristic of microdroplets. For this reason, we employ the CCFA, which has already been used to deform microdroplets in an oscillatory fashion and mea-

sure the resulting force response on the cantilevered capillary [1], making it an ideal instrument for implementing this framework.

Before proceeding further, we briefly outline the operation of the OSFR for macroscopic droplets. In this device, a small volume of fluid (typically 10–100 mL) is confined between two coaxial, millimeter-sized circular substrates of radius  $R$ . The fluid is pinned at the rims of the substrates, and the upper substrate is adjusted so that the fluid maintains a pinning angle of  $\pi/2$  at both rims (i.e., a cylindrical shape), with a thin gap  $H_0$  established between them, corresponding to a small aspect ratio  $\delta = H_0/R \ll 1$ . The upper substrate is then driven in an oscillatory fashion with a small strain amplitude, ensuring that nonlinearities in the resulting flow field remain negligible at leading order, thereby yielding a lubrication flow [29]. The post-transient oscillatory force response exerted on the lower substrate is subsequently measured as a function of time, from which the frequency-dependent storage modulus  $G'(\omega)$  and loss modulus  $G''(\omega)$  can be obtained directly.

The storage modulus  $G'(\omega)$  represents the in-phase (with the imposed strain) elastic component of the response that quantifies the energy stored per oscillation cycle, whereas the loss modulus  $G''(\omega)$  represents the out-of-phase viscous component associated with energy dissipation [31, 32, 34, 36, 58]. Both moduli are directly related to the intrinsic rheological parameters  $\mu_0$ ,  $G_0$ , and  $\lambda$ , and thus enable their characterization by measuring these moduli at a given frequency or, more commonly, across an entire frequency sweep. At the macroscopic scale, however, capillary stresses are small compared with bulk viscous and elastic stresses, since the elasto-capillary and capillary numbers are typically large,  $Ec = G'R/\gamma \gg 1$  (or  $Ec_0 = G_0R/\gamma \gg 1$ ) and  $Ca = G''R/\gamma \gg 1$  (or  $Ca_0 = \mu_0R\omega/\gamma \gg 1$ ). Consequently, interfacial effects are negligible in this regime, and the interfacial tension  $\gamma$  cannot be inferred. We briefly remark here that the CCFA has not yet been implemented in the thin-gap, initially cylindrical configuration characteristic of the OSFR, however, such an adaptation is, in principle, feasible.

The first study to investigate the operation of the OSFR in the low-to- $\mathcal{O}(1)$  capillary number regime ( $\bar{Ca} = \mu R\omega/\gamma \lesssim 1$ ) was conducted by Barakat et al. [13]. Although their work considered macroscopic Newtonian droplets, significant effects from capillary stresses emerged because they assumed either sufficiently small droplet viscosity or sufficiently low oscillation frequency to render  $\bar{Ca} \lesssim 1$ . This approach enabled them to extract both the dynamic viscosity  $\mu$  and the interfacial tension  $\gamma$  directly from the measured force response. Importantly, the dynamics captured by Barakat et al. [13] for macroscopic Newtonian droplets with low viscosity or driven at low frequency are equally representative of Newtonian microdroplets, since both cases lie in the  $\bar{Ca} \lesssim 1$  regime.

In Chapter 3, we address Question (ii) by extending this analytical framework to viscoelastic microdroplets whose linear viscoelastic behaviour at low strain amplitudes is described by the (single-mode) Maxwell model. In doing so, we address the current scarcity of analytical approaches that simultaneously probe both the bulk rheology—namely  $G'(\omega)$  and  $G''(\omega)$ , and hence  $\mu_0$ ,  $G_0$ , and  $\lambda$ —together with the interfacial tension  $\gamma$ . More broadly, the framework applies to any viscoelastic droplet (or thin film) subjected to oscillatory deformation in the OSFR configuration where interfacial stresses remain significant, i.e., in the  $Ec \lesssim 1$  and  $Ca \lesssim 1$  regimes. The flow field within the droplet is modeled using a regular perturbation expansion in the small strain amplitude ( $\varepsilon \ll 1$ ) and small aspect ratio ( $\delta^2 \ll 1$ ), with the bulk deviatoric stress given by the Maxwell model at leading order. The thin-gap geometry, small-amplitude oscillations, and initially cylindrical base state ensure that interface slopes remain small, such that the leading-order post-transient velocity field within the droplet is governed entirely by the oscillatory motion of the upper substrate.

The resulting force response consists of a static component—arising from Laplace pressure and contact-line tension—together with a dynamic component composed of linear in-phase contributions from interfacial curvature and bulk elasticity, and an out-of-phase contribution from bulk viscosity. The dynamic component arises through the lubrication pressure. From this response, the interfacial

tension  $\gamma$  can be extracted from the static contribution, which then serves to determine the frequency-dependent storage and loss moduli,  $G'(\omega)$  and  $G''(\omega)$ , from the dynamic component. In turn, the intrinsic bulk material parameters—the zero-shear viscosity  $\mu_0$ , infinite-frequency modulus  $G_0$ , and relaxation time  $\lambda = \mu_0/G_0$ —can be inferred. This framework therefore provides the first simple yet robust analytical method for simultaneously determining both the bulk rheology and the interfacial tension of a viscoelastic microdroplet solely from its oscillatory force response in the OSFR configuration.

Following this chapter, the thesis is organized as follows. Chapter 2 develops an asymptotic model that captures the leading nonlinear force response and morphology of a pinned, axisymmetric Newtonian microdroplet (or microbubble) confined between two equivalent coaxial capillaries, as the droplet departs quasi-statically from its undeformed (spherical, zero-force) state while remaining in equilibrium at each deformation. Chapter 3 then presents an asymptotic model for the leading-order dynamic behaviour and force response of a pinned, axisymmetric viscoelastic microdroplet under small-amplitude, thin-gap oscillatory deformation, as is typical in the OSFR. In this context, we outline a procedure to decouple the interfacial tension and the storage and loss moduli of the droplet from its measured force response. Finally, Chapter 4 summarizes the key findings of the two analytical frameworks, highlights their limitations and implications, and discusses potential extensions.

# Chapter 2

## A second-order asymptotic theory for the nonlinear quasi-static deformation of axisymmetric capillary bridges

### 2.1 Introduction

The macroscopic behaviour of multiphase systems—such as foams, emulsions, and suspensions—is governed by microscale interfacial phenomena, including aggregation, coalescence, break-up, adhesion and arrested drainage of the constituent droplets, bubbles, or particles. These microscale interactions control bulk properties such as stability, texture, and shelf-life in a wide range of consumer products, from cosmetic formulations—e.g., moisturizing creams, sunscreen lotions, and shampoos—to foodstuffs such as mayonnaise, ice cream, and whipped toppings [107–109]. Accurate quantification of fluid–fluid and fluid–solid interactions at the single-particle scale is therefore essential for the rational design of such formulations and for engineering the next generation of multiphase materials, such as capillary suspensions that solidify into porous, 3D-printable scaffolds [110, 111].

At the heart of these interfacial processes lies *capillarity*: the balance between interfacial tension and the pressure difference across a static fluid–fluid interface. This balance was independently quantified in the early 1800s by Young [112] and Laplace [113], culminating in the classical Young–Laplace equation, which relates the pressure jump (commonly referred to as the Laplace pressure) to the mean curvature of the interface [16, 17]. Shortly thereafter, Gauss [114], in 1830, rederived this relation by minimizing the total surface energy of a static interface at fixed enclosed volume, yielding a differential equation for its equilibrium shape. Poisson [115] soon provided a molecular-mechanical interpretation, while Cauchy [116] recast the law within the framework of continuum mechanics. Building on these theoretical foundations, the soap-film experiments of Plateau [117] in the early 1840s posed the celebrated minimal-surface (zero mean curvature) *Plateau’s problem*, which catalyzed the broader study of constant-mean-curvature (CMC) surfaces.

Within this programme, Delaunay [102] showed that the only axisymmetric CMC surfaces are those formed by rotating the roulettes of conics—planes, cylinders, spheres, catenoids, unduloids, and nodoids. Subsequently, Howe [118] employed variational calculus to determine which nodoidal pendular rings maximize or minimize enclosed volume at fixed interfacial area. Nearly a century later, Orr et al. [119] analytically classified all axisymmetric menisci between coaxial substrates using elliptic integrals, reporting their shapes, curvatures, areas, enclosed volumes, and capillary forces. Kenmotsu [120] elliptic-integral-based parameterization of the full Delaunay family in terms of the bulge parameter, mean curvature, and pinning angle. Many significant contributions emerged in

the intervening century, which are thoroughly synthesized in the monograph by Finn [103]. These *Delaunay surfaces* remain a cornerstone of contemporary capillary mechanics, as they describe the equilibrium shapes of axisymmetric capillary bridges formed when a droplet, bubble, or small volume of fluid is held between two coaxial substrates in the absence of significant gravitational forces.

Axisymmetric capillary bridges arise in diverse settings: pendular rings that bind wet sand grains [121], liquid threads linking micron-scale anchor particles in inkjet and 3D printing [12], transient necks between coalescing droplets or bubbles in emulsification equipments [122], and sub-millimeter menisci responsible for adhesion in insect pads [123] and soft robotic grippers [124]. When the two coaxial substrates that pin the contact lines of the bridge are held at their equilibrium spacing, the interfacial free energy is minimized, and the bridge adopts a spherical profile. In this undeformed state, the Laplace pressure balances the normal component of the line tension at the contact lines, resulting in zero net axial force on the substrates. A small quasi-static displacement of the substrates perturbs this balance and generates a finite axial force that depends on the interfacial tension as well as the evolving CMC bridge shape. Measuring the resulting force–displacement curve, therefore, offers a direct mechanical route to infer interfacial tension, while simultaneously encoding information about the evolving bridge geometry.

Over the past four decades, a succession of instruments has led to the development of the cantilevered-capillary force apparatus (CCFA), introduced by Frostad et al. [1], which is well suited to measuring the axial force exerted by highly deformable soft microparticles—including, but not limited to, micrometer-sized droplets or bubbles confined as axisymmetric capillary bridges. Among the earliest predecessors were micropipette tensiometers [80], inspired by the biomembrane force probe [19, 75], in which a glass pipette held a single emulsion droplet by suction and inferred the interfacial tension from the critical suction pressure. However, this technique did not yield a force–displacement relationship and was limited by the fragility of the flame-pulled pipette tips. The micro-cantilever tensiometer introduced by Moran et al. [20] adapted this design by employing two suction pipettes to hold the droplet, one of which acted as an elastic beam of known spring constant (a calibrated cantilever), enabling displacements up to  $\approx 50\text{ }\mu\text{m}$  and measurable forces in the range  $10\text{ nN}\text{--}5\text{ }\mu\text{N}$ . This facilitated the first quasi-static force–displacement measurements for  $10\text{--}40\text{ }\mu\text{m}$  droplets, though each trial required carefully pulled tips and detachments were common on hydrophobic interfaces, which limited operational robustness and replicability.

The atomic force microscope (AFM) extended the lower force limit to  $\sim 10\text{ pN}$  with sub-nanometer displacement resolution [21, 85]. In this configuration, a spherical bead mounted on an AFM cantilever is brought into contact with a substrate, forming a water–air or water–oil bridge whose axial force is inferred optically. While invaluable for nanodroplets, AFM becomes impractical for radii  $\gtrsim 10\text{ }\mu\text{m}$  owing to meniscus pinning along the probe shank and snap-to-contact instabilities. More generally, reliably attaching highly deformable microparticles to the flat or sharpened tip of the AFM cantilever is difficult, and often requires fixation to a planar substrate and pre-stressing, which can introduce significant deformations and bias the inferred material properties. Surface force apparatuses (SFA) [76, 77] and optical or magnetic tweezers [79] offer even finer force resolution ( $< 1\text{ nN}$ ), but their effective particle size range ( $\lesssim 5\text{ }\mu\text{m}$ ) renders them less suitable for typical emulsion droplets or foam bubbles.

The CCFA mitigates many of these limitations—fragility, accessible particle size, particle attachment issues, and replicability. As discussed in Chapter 1 and illustrated in Fig. 1.1, it employs two coaxial borosilicate capillaries—one rigid and the other acting as a calibrated cantilever—to pin or gently aspirate (via suction) a droplet or bubble of radius between  $10\text{ }\mu\text{m}$  and  $1\text{ mm}$ . Laser interferometry resolves cantilever deflections down to nanometer precision, enabling force measurements spanning  $1\text{ nN}$  to  $1\text{ mN}$ . The apparatus has been successfully employed to record quasi-static force–displacement curves under compressions up to the maximum compression limit—where the

pinning angle reaches  $180^\circ$ —and under dilations comparable to the undeformed droplet or bubble radius  $R_d$ . To date, its accuracy has been validated in the small-displacement regime,  $|\Delta L| \lesssim 0.1R_d$ , by comparison with the linear force–displacement theory of Kusumaatmaja and Lipowsky [2], with excellent agreement observed.

However, beyond this small linear regime lies the nonlinear regime, where validating the apparatus requires solving the full nonlinear Young–Laplace boundary-value problem at each prescribed displacement. This can be accomplished using (i) standard ordinary differential equation (ODE) solvers, such as shooting methods with Runge–Kutta integrators [20]; (ii) variational approaches, including finite-element collocation [105] or mesh-based optimization using the Surface Evolver [100, 101]; or (iii) hydrodynamic relaxation methods, such as those employing lattice–Boltzmann formulations [106]. While all of these methods are numerically tractable, they remain cumbersome for routine analysis. A closed-form analytical expression that captures the leading-order nonlinear force response would offer substantial practical advantages for CCFA-based measurements.

The only prior analytical effort to probe the nonlinear regime is the quadratic force law proposed by Sariola [3], who performed a second-order Taylor expansion of the force response in the displacement  $\Delta L$  about the zero-force (undeformed) state. While their first-order coefficient correctly recovers the linear spring constant derived by Kusumaatmaja and Lipowsky [2], to reduce algebraic complexity, their second-order term accounts solely for shape variations due to the Kenmotsu bulge parameter  $B$  [120] and neglects concomitant changes in mean curvature and pinning angle. As a result, the model omits key shape-mediated contributions at second-order and performs only marginally better than the linear theory, failing to accurately capture the leading-order nonlinear behaviour.

Incorporating the missing shape-mediated corrections within their Taylor series framework would be algebraically intractable, as the existing computations are already unwieldy. On the other hand, the method of Kusumaatmaja and Lipowsky [2] proceeds by expanding the shape-mediated boundary conditions and volume constraint of the Young–Laplace equation in a small dimensionless force parameter, eliminating first-order variations in mean curvature and pinning angle to yield a closed-form linear correction of the force. However, this systematic elimination procedure does not generalize easily to second order.

These limitations motivate the present work: to derive a closed-form analytical expression that accurately captures the leading-order nonlinear force–displacement relationship by systematically incorporating all shape-mediated corrections. To this end, we adopt the parameterization scheme of Kusumaatmaja and Lipowsky [2] in terms of the local tilt angle  $\phi$ , which fully characterizes the shape of the axisymmetric capillary bridge—pinned between two coaxial capillaries of equal radius in the CCFA—in terms of the force  $F$ , mean curvature  $\mathcal{H}$ , and pinning angle  $\theta$  at any displacement from the undeformed state. This parameterization allows us to express the two capillary rim boundary conditions and the bridge volume conservation constraint in terms of the parameterized shape, thereby yielding three governing relations for  $F$ ,  $\mathcal{H}$ , and  $\theta$ . However, these relations involve elliptic integrals inherited from the parameterized shape and cannot, in general, be expressed using elementary functions, except in the special case of the zero-force spherical state.

To proceed analytically, we first note that the dimensionless displacement  $\varepsilon = \Delta L/R_d$  remains small ( $|\varepsilon| \ll 1$ ) throughout the leading-order nonlinear regime. This allows us to expand  $F$ ,  $\mathcal{H}$ , and  $\theta$  as regular perturbation series in  $\varepsilon$  about their values in the undeformed state, where each coefficient is a function of the zero-force pinning angle  $\theta_0$ . Substituting these expansions into the governing relations and solving order by order in  $\varepsilon$ , we recover the linear spring constant of Kusumaatmaja and Lipowsky [2] at first order of the force response and derive a second-order correction that accurately captures the leading-order nonlinear behaviour. Additionally, we obtain corresponding first- and second-order corrections to the mean curvature, pinning angle, and bridge shape. For completeness,

we also solve separately for the shape of the droplet caps confined within the capillaries.

Comparing our model with numerical solutions of the full Young–Laplace boundary-value problem using a fourth–fifth order Runge–Kutta (RK45) shooting method reveals excellent agreement across the range of capillary radii typical of the CCFA ( $0.3 \leq R/R_d \leq 0.6$ ). Specifically, the displacement  $\Delta L$  at which the analytical force response incurs a 2% relative error during dilation ranges from approximately  $0.7R_d$  at  $R/R_d = 0.3$  to  $0.3R_d$  at  $R/R_d = 0.6$ . Under maximum compression, the relative error remains  $\approx 1\%$  across this entire range.

By contrast, the models of Kusumaatmaja and Lipowsky [2] and Sariola [3] attain similar accuracy only at displacements  $|\Delta L| \lesssim 0.05R_d$ . Our model further captures the nonlinear trend that the incremental force required to displace a droplet between adjacent equilibrium states increases under compression and decreases under dilation, with this incremental force growing with capillary radius at each step. Thus, our work provides the first closed-form analytical description of the leading-order nonlinear behaviour of not only the droplet–CCFA system, but of any axisymmetric capillary bridge with fixed contact lines under quasi-static deformation, using only the initial pinning angle  $\theta_0$  or the capillary-to-droplet radius ratio  $R/R_d$  as input.

Following this section, the chapter is organized as follows. In Section 2.2, we describe the geometry of the CCFA–droplet system and solve the axisymmetric Young–Laplace equation for the shapes of the droplet caps and the parameterized bridge. We then formulate the three governing relations for the force response  $F$ , mean curvature  $\mathcal{H}$ , and pinning angle  $\theta$ —the parameters that completely characterize the bridge shape. In Section 2.3, we nondimensionalize the system and posit that these parameters can be expressed as regular perturbation series in the small dimensionless displacement  $\varepsilon = \Delta L/R_d$  about their zero-force (undeformed) state values. We then substitute these expansions into the dimensionless governing relations and solve them order by order to obtain the first- and second-order coefficients of the three parameters.

These second-order expansions are subsequently used to derive the corresponding expansion of the parameterized bridge shape. In Section 2.4, we assess the accuracy of our model against RK45 shooting solutions for the force response under both compression and dilation, compare its performance with the linear model of Kusumaatmaja and Lipowsky [2] and the quadratic model of Sariola [3], and discuss the nonlinear physical trends captured by the model. We then perform the same analysis for the mean curvature, pinning angle, and bridge shape for completeness. We close this section by outlining the limitations of the present analytical framework and their implications. Finally, in Section 2.5, we summarize the key findings and briefly discuss potential extensions to surfactant-laden Newtonian droplets (or bubbles) and, more generally, to axisymmetric capillary bridges under quasi-static deformation.

## 2.2 Problem setup

We consider a Newtonian microdroplet (or microbubble) of constant density  $\rho$  pinned at equilibrium between two coaxial cylindrical capillaries of inner radius  $R = 10\text{--}100\,\mu\text{m}$ . This setup is immersed in an ambient Newtonian fluid of constant density  $\rho_a$ , which also fills the interiors of the capillaries. The Bond number of the droplet is given by  $\text{Bo} = \Delta\rho g R_d^2 / \gamma \sim \Delta\rho g R^2 / \gamma \sim 10^{-5}\text{--}10^{-3} \ll 1$ , where  $R_d \sim R$  is the radius of the undeformed droplet,  $\Delta\rho = \rho - \rho_a$  is the density difference,  $g$  is the gravitational acceleration, and  $\gamma$  is the constant interfacial tension between the droplet and the ambient fluid. The small Bond number indicates that gravitational forces are negligible compared to interfacial curvature forces. As a result, the undeformed equilibrium shape of the droplet is a perfect sphere with its center aligned along the common axis of the capillaries.

We define this *undeformed state*, shown in Fig. 2.1(a), as the initial equilibrium configuration.

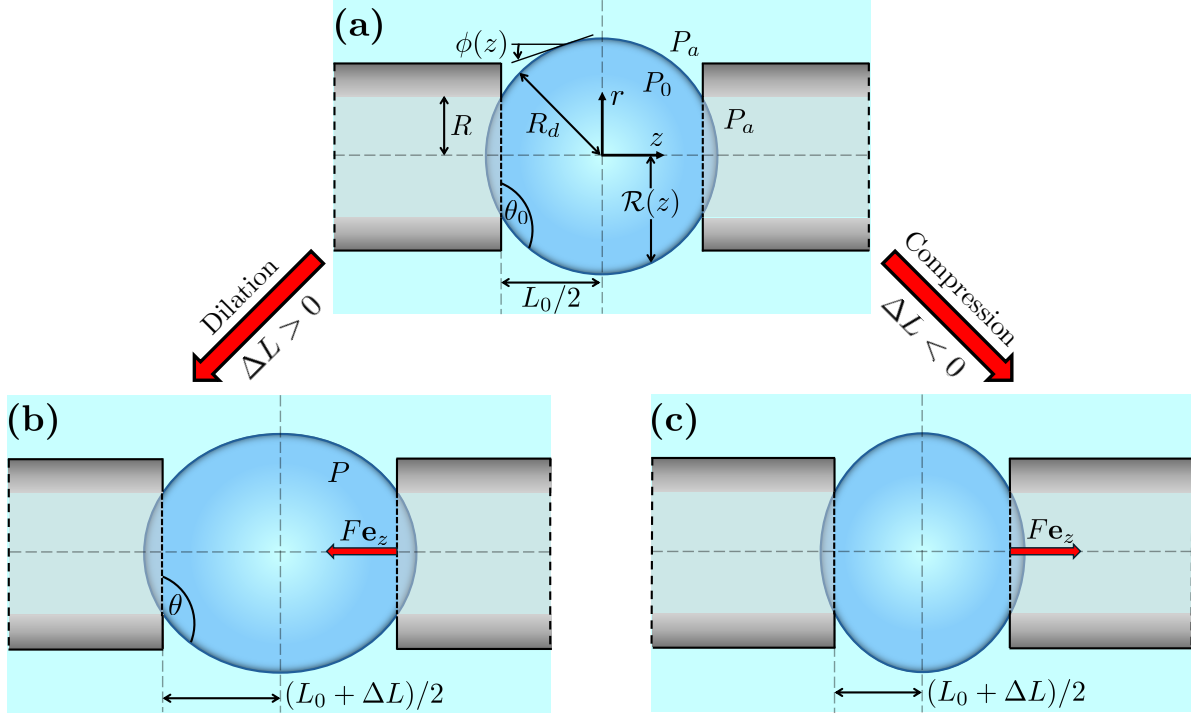


**Figure 2.1:** (a) Schematic of an undeformed (spherical) microdroplet (or microbubble) of radius  $R_d$  pinned at equilibrium at the rims of coaxial capillaries of inner radius  $R = 10\text{--}100\,\mu\text{m}$ . (b) and (c) The capillaries are quasi-statically displaced by  $\Delta L/2$  in opposite directions from this initial state, dilating the droplet [(b)  $\Delta L > 0$ ] or compressing it [(c)  $\Delta L < 0$ ], and the system is allowed to reach a new equilibrium.

In the absence of gravity, the hydrostatic pressures within the droplet and the ambient fluid (both inside and outside the capillaries) are spatially uniform, denoted by  $P_0$  and  $P_a$ , respectively. The axial separation between the capillary rims is  $L_0$ , and the pinning angle is  $\theta_0$ . We refer to the region of the droplet between the capillaries as the *bridge*, and the portions of the droplet extending into the capillaries as the *caps*. It is well established that a spherical bridge exerts zero net force on either capillary rim plane (which includes the capillary rim and the droplet fluid enclosed within it) [16, 17, 125]. Accordingly, we synonymously refer to this initial configuration as the *zero-force state*.

From the undeformed state, the two capillaries are displaced axially in opposite directions by a distance  $\Delta L/2$  [see Figs. 2.1(b) and (c)], such that the overall strain remains small, i.e.,  $|\Delta L/L_0| \ll 1$ . The system is then allowed to attain a new equilibrium, where all transient flow fields have dissipated and viscous stresses are negligible. Owing to the small Bond number ( $\text{Bo} \ll 1$ ), gravitational effects remain insignificant throughout, and the droplet–ambient fluid interface preserves its axisymmetric shape about the common axis of the capillaries in the small-strain regime.

This interface is thus described by the function  $r = \mathcal{R}(z)$  in an axisymmetric cylindrical coordinate system  $(r, z)$ , with the origin located at the center of the undeformed droplet. Since the capillaries have equal inner radii, the interface is also symmetric about the  $r$ -axis, and a single pinning angle  $\theta$  suffices to describe its contact with both rims. The local inclination of the interface is given by the tilt angle  $\phi(z) = \arctan(\mathcal{R}')$ , where  $\mathcal{R}' = d\mathcal{R}/dz$ . The axial separation between the capillary rims becomes  $L = L_0 + \Delta L$ , with the left and right rims located at  $z = -L/2$  and  $z = L/2$ , respectively.

The ambient fluid maintains a nearly constant pressure at  $P_a$ , while the pressure inside the

droplet adjusts to  $P$  to satisfy the new mechanical equilibrium. Once equilibrium is attained, the force exerted by the droplet on the right capillary rim plane at  $z = L/2$  is measured—this is referred to as the *force response*. This procedure is repeated for different values of  $\Delta L$  within the small-strain regime to determine the variation of force response with displacement from the undeformed state. The framework described here captures the essential physics of quasi-static deformation experiments performed with the CCFA [1] or the microcantilever tensiometer [20], as well as a broad class of quasi-statically deformed axisymmetric liquid bridges encountered in natural and industrial settings [14].

The equilibrium shapes  $\mathcal{R}(z)$  attained by the droplet–ambient fluid interface at any displacement from the undeformed state are governed by the classical Young–Laplace equation, which expresses the static balance between the Laplace pressure jump  $\Delta P = P - P_a$  and the curvature-induced stresses at the interface:

$$\frac{\Delta P}{\gamma} = 2\mathcal{H} = \frac{1}{\mathcal{R}(1 + \mathcal{R}'^2)^{1/2}} - \frac{\mathcal{R}''}{(1 + \mathcal{R}'^2)^{3/2}}, \quad (2.1)$$

where  $\mathcal{R}'' = d^2\mathcal{R}/dz^2$ , and  $\mathcal{H}$  denotes the mean curvature of the interface. In the  $Bo \ll 1$  regime, hydrostatic pressure variations due to gravity are negligible, so that  $\Delta P$ , and hence  $\mathcal{H}$ , are constant along the interface. Here, the first term on the right-hand side represents the azimuthal (circumferential or hoop) curvature, which quantifies the rotation of the interface normal as one traverses a ring of constant meridional coordinate. The second term is the meridional (axial) curvature, associated with the rotation of the interface normal along the meridional arc [15–17].

To uniquely determine the interface shape, we solve Eqn. (2.1) separately for the bridge and the two caps. For the bridge, this equation is solved subject to boundary conditions at the capillary rim planes:  $\mathcal{R}(z = \pm L/2) = R$ . Alternatively, one of these may be replaced by the reflection symmetry condition  $\mathcal{R}'(z = 0) = 0$ . However, the mean curvature  $\mathcal{H}$  is not known *a priori*, except in the undeformed state where  $\mathcal{H}(\Delta L = 0) = \mathcal{H}_0 = 1/R_d$ , and hence an additional constraint is required to close the system. This constraint arises from mass conservation, which mandates that the total volume of the droplet remains constant for all displacements. This in turn determines the bridge volume  $V_b$  as a function of the mean curvature  $\mathcal{H}$  and capillary radius  $R$  [see Eqn. (B.1)].

In the small-strain regime ( $|\Delta L/L_0| \ll 1$ ), and for typical CCFA capillary radii satisfying  $R/R_d \in [0.3, 0.6]$ , this constraint simplifies to the condition that the bridge volume remains approximately equal to its undeformed value (details in Appendix B.1). The shapes of the caps are computed by utilizing the capillary rim boundary conditions, along with the axisymmetry condition that the interface meets the  $z$ -axis perpendicularly, i.e., at  $\mathcal{R} = 0$ , the local tilt angle  $\phi = \pi/2$  for the left cap and  $\phi = -\pi/2$  for the right cap. In this case, the mean curvature  $\mathcal{H}$  is already determined from the bridge shape, and thus no further constraint is necessary.

In terms of the tilt angle  $\phi$ , Eqn. (2.1) can be rewritten as

$$2\mathcal{H} = \frac{\cos \phi}{\mathcal{R}} - \phi' \cos \phi,$$

where  $\phi' = d\phi/dz$ . Introducing the differential arc length along the meridian,  $ds = \sqrt{(d\mathcal{R})^2 + (dz)^2}$ , we obtain the geometric identities:  $dz/ds = \cos \phi$ ,  $d\mathcal{R}/ds = \sin \phi$ , and  $d\phi/ds = \phi' \cos \phi$ . Using these identities, it can be shown that the above form of the Young–Laplace equation admits the following *first integral*:

$$\mathcal{A} = \mathcal{R} \cos \phi - \mathcal{H} \mathcal{R}^2, \quad (2.2)$$

where  $\mathcal{A}$  is a constant (with dimensions of length) along the interface [102–104]. However, its value differs between the bridge and the caps, due to the distinct boundary constraints in each region.

For the caps, imposing the axisymmetry boundary condition in Eqn. (2.2) yields  $\mathcal{A} = 0$ , indicating that the cap surfaces are arcs of a sphere of radius  $1/\mathcal{H}$ . Using the rim boundary condition, the cap profiles can be parameterized in terms of the tilt angle as:

$$\mathcal{R}(\phi) = \frac{\cos \phi}{\mathcal{H}}, \quad z(\phi) - Z_0 = -\frac{\sin \phi}{\mathcal{H}}, \quad (2.3)$$

where  $\phi \in [\arccos(\mathcal{H}R), \pi/2]$  for the left cap and  $\phi \in [-\pi/2, -\arccos(\mathcal{H}R)]$  for the right cap. The cap centers are located at  $(0, \pm Z_0)$ , with  $Z_0 = L/2 - (1/\mathcal{H}^2 - R^2)^{1/2}$ , with the upper and lower signs corresponding to the right and left caps, respectively. This fully characterizes the cap profiles, except that the mean curvature  $\mathcal{H}$  is fixed by enforcing the bridge volume constraint while solving for the bridge shape.

For the bridge, the value of the constant  $\mathcal{A}$  is determined by imposing either of the rim conditions,  $\mathcal{R} = R$  at  $\phi = \pi/2 - \theta$  (or equivalently, at  $\phi = \theta - \pi/2$ ), which yields:

$$\mathcal{A} = R \sin \theta - \mathcal{H}R^2 = -\frac{F}{2\pi\gamma}, \quad (2.4)$$

where  $F\mathbf{e}_z$  is the force exerted by the droplet bridge on the right capillary rim plane located at  $z = L/2$ , with  $\mathbf{e}_z$  denoting the unit vector in the positive  $z$ -direction. The term  $-2\pi\gamma R \sin \theta \mathbf{e}_z$  represents the line interfacial tension force with which the bridge interface pulls the capillary rim along its perimeter  $2\pi R$ , while the term  $2\pi\gamma\mathcal{H}R^2 \mathbf{e}_z$  corresponds to the Laplace pressure force exerted by the bridge on the fluid cross-section of area  $\pi R^2$  enclosed by the capillary rim.

We solve the quadratic equation for the parameterized radial profile  $\mathcal{R}(\phi)$  obtained from the first integral (2.2) after substituting the value of the constant  $\mathcal{A}$  from Eqn. (2.4). The negative branch degenerates to the non-physical solution  $\mathcal{R} = 0$  as the force response  $F \rightarrow 0$ . The positive branch yields the correct profile,

$$\mathcal{R}(\phi) = \frac{1}{2\mathcal{H}} \left[ \cos \phi + (\cos^2 \phi - 4\mathcal{F})^{1/2} \right], \quad \pi/2 - \theta \leq \phi \leq \theta - \pi/2, \quad (2.5)$$

as it recovers the undeformed state (spherical) profile  $\mathcal{R}_0(\phi) = \cos \phi / \mathcal{H}$  in the limit  $F \rightarrow 0$ , where  $\mathcal{H} = \mathcal{H}_0 = 1/R_d$  and  $\phi \in [\pi/2 - \theta_0, \theta_0 - \pi/2]$ . Here, the dimensionless force parameter  $\mathcal{F}$  is defined as  $\mathcal{F} = \mathcal{H}\mathcal{A} = -F/(2\pi\gamma\mathcal{H}^{-1})$ .

To obtain the parameterized axial bridge profile  $z(\phi)$ , we begin with the slope relation  $d\mathcal{R}/dz = \tan \phi$ , which gives us

$$\frac{dz}{d\phi} = \cot \phi \frac{d\mathcal{R}}{d\phi} = -\frac{1}{2\mathcal{H}} \left[ \cos \phi + \cos^2 \phi (\cos^2 \phi - 4\mathcal{F})^{-1/2} \right].$$

Integrating this expression from  $\phi = 0$ , where  $z = 0$  by reflection symmetry, we obtain

$$z(\phi) = -\frac{1}{2\mathcal{H}} \left[ \sin \phi + \int_0^\phi \left\{ \cos^2 \xi (\cos^2 \xi - 4\mathcal{F})^{-1/2} \right\} d\xi \right], \quad \pi/2 - \theta \leq \phi \leq \theta - \pi/2. \quad (2.6)$$

In the undeformed state ( $F = 0$ ), the axial profile reduces to the spherical form  $z = z_0(\phi) = -\sin \phi / \mathcal{H} = -R_d \sin \phi$ .

Before proceeding further, we note that Eqns. (2.5) and (2.6) imply that the axisymmetric bridge profile is physically valid only when  $\mathcal{F} < \cos^2 \phi / 4$ . This imposes a constraint on the maximum stretching force  $-F$  ( $F < 0$ ) that can be applied before the bridge either loses axisymmetry or starts

pinching off, i.e., the inequality  $-F < \pi\gamma\cos^2\phi/(2\mathcal{H})$  must be satisfied along the entire interface. In particular, axisymmetry is first lost at the capillary rims when  $-F \geq \pi\gamma\sin^2\theta/(2\mathcal{H})$ .

Now, applying either of the rim boundary conditions to the radial profile (2.5) recovers the force response equation (2.4) in terms of the dimensionless force parameter  $\mathcal{F}$ , and relates the three displacement ( $\Delta L$ )-dependent unknowns: the force response  $F$ , the mean curvature  $\mathcal{H}$ , and the pinning angle  $\theta$ :

$$R\mathcal{H} = \frac{1}{2} \left[ \sin\theta + (\sin^2\theta - 4\mathcal{F})^{1/2} \right]. \quad (2.7)$$

Similarly, applying either of the rim boundary conditions to the axial profile (2.6) gives us the capillary separation  $L$ , providing a second relation among the same three unknowns:

$$L\mathcal{H} = -\cos\theta - \int_0^{\frac{\pi}{2}-\theta} \left\{ \cos^2\xi (\cos^2\xi - 4\mathcal{F})^{-1/2} \right\} d\xi. \quad (2.8)$$

The third relation is obtained by enforcing the volume constraint that the bridge volume remains approximately constant in the small-strain limit and for typical CCFA capillary radii (as discussed in Section 2.2):

$$\begin{aligned} V_b\mathcal{H}^3 &= -\pi \left[ \cos\theta - \frac{1}{3}\cos^3\theta - \mathcal{F}\cos\theta \right. \\ &\quad \left. + \frac{1}{4} \int_0^{\frac{\pi}{2}-\theta} \left\{ 3\cos^2\xi (\cos^2\xi - 4\mathcal{F})^{1/2} + \frac{\cos^4\xi}{(\cos^2\xi - 4\mathcal{F})^{1/2}} \right\} d\xi \right] \\ &= \frac{2\pi\cos\theta_0(\cos^2\theta_0 - 3)}{3} (R_d\mathcal{H})^3. \end{aligned} \quad (2.9)$$

Together, Eqns. (2.7)–(2.9) uniquely determine the force response  $F$ , the mean curvature  $\mathcal{H}$ , and the pinning angle  $\theta$ . Once these quantities are obtained, they can be substituted into Eqns. (2.5) and (2.6) to construct the parameterized bridge profile in terms of the tilt angle  $\phi$ . However, the integrals appearing in the axial profile  $z(\phi)$ , in the capillary separation equation, and in the bridge volume constraint generally cannot be expressed in terms of elementary functions. For instance, the axial profile takes the form

$$z(\phi) = -\frac{1}{2\mathcal{H}} \left[ \sin\phi + \frac{4\mathcal{F}}{c} E_1(\phi, 1/c) + cE_2(\phi, 1/c) \right], \quad c = (1 - 4\mathcal{F})^{1/2},$$

where

$$E_1(\varphi, s) = \int_0^\varphi (1 - s^2 \sin^2\xi)^{-1/2} d\xi, \quad E_2(\varphi, s) = \int_0^\varphi (1 - s^2 \sin^2\xi)^{1/2} d\xi,$$

are the incomplete elliptic integrals of the first and second kind, respectively [126].

These functions are non-elementary for general values of  $s$ , and reduce to elementary forms only in special cases: when  $s = 1$ , which corresponds to  $c = 1$  and thus  $\mathcal{F} = 0$ , i.e., the undeformed state; when  $s = 0$ , corresponding to  $c \rightarrow \infty$  and hence  $\mathcal{F} \rightarrow \infty$ , implying unbounded forces and is therefore unphysical; and when  $s = -1$ , corresponding to  $c = -1$ , which violates the condition  $c \geq 0$ . As a consequence, although the parametric representation of the bridge profile and the three governing equations for  $F$ ,  $\mathcal{H}$ , and  $\theta$  are exact, they are not readily amenable to analytical treatment or experimental application except for the undeformed spherical state. In the next section, we address

this limitation by employing perturbation expansions in the small-strain limit about the undeformed (zero-force) state, enabling us to approximate the elliptic integrals and derive closed-form expressions for the force response, mean curvature, pinning angle, and the bridge profile [2].

Before proceeding to the perturbation expansions, we briefly remark that instead of the droplet being pinned at the capillary rims, it can also be held at the rims by applying a constant capillary suction pressure, as is commonly implemented in the CCFA or microcantilever technique [1, 20]. In other words, the ambient pressure inside the capillaries is maintained at a constant value  $P_c$  that is lower than the ambient pressure  $P_a$  outside, thereby imposing a constant suction pressure  $\Delta P_c = P_a - P_c$  on the droplet caps. In Appendix B.2, we show in detail that for the typical range of suction pressures and capillary radii used in the CCFA, the relative change in bridge volume remains confined to within 5% in the small-strain regime.

Consequently, the shape-mediated equations governing the force response, bridge mean curvature, and pinning angle—Eqns. (2.7)–(2.9)—remain unchanged from the pinned droplet case, except that the zero-force state bridge radius  $R_b$  is now smaller than the undeformed droplet radius  $R_d$ , giving us the zero-force state profile:

$$\mathcal{R}_0(\phi) = R_b \cos \phi, \quad z_0(\phi) = -R_b \sin \phi,$$

where  $\phi \in [\pi/2 - \theta_0, \theta_0 - \pi/2]$ , and  $\theta_0$  is the new pinning angle in this zero-force configuration. Accordingly, the asymptotic analysis that we will discuss next carries over without modification. Similarly, the profile of the caps is obtained by replacing the bridge mean curvature  $\mathcal{H}$  by the cap mean curvature  $\mathcal{H}_c = (P - P_c)/2\gamma$  in Eqn. (2.3).

## 2.3 Non-dimensionalization and asymptotic analysis

We non-dimensionalize all variables with dimensions of length by the undeformed droplet radius  $R_d$  and the force response  $F$  by  $2\pi\gamma R_d$ . All dimensionless variables are denoted with a hat ‘ $\hat{\cdot}$ ’ to distinguish them from their dimensional counterparts. In the limit of small strain,  $|\Delta L/L_0| \ll 1$ , the dimensionless displacement  $\varepsilon = \Delta L/R_d = -2 \cos \theta_0 (\Delta L/L_0)$  also satisfies  $|\varepsilon| \ll 1$ . Accordingly, in this regime, we posit that the dimensionless force response  $\hat{F}$ , mean curvature  $\hat{\mathcal{H}}$ , and pinning angle  $\theta$  can be expressed as regular perturbation expansions in  $\varepsilon$  about their respective values in the undeformed (zero-force) configuration. In these expansions, the coefficient at the  $i^{\text{th}}$  order is denoted by  $\hat{F}_i$ ,  $\hat{\mathcal{H}}_i$ , and  $\theta_i$ , respectively, for all integers  $i \geq 0$ . Each coefficient depends hierarchically on lower-order corrections and is thus ultimately a function of the undeformed (zero-force) pinning angle  $\theta_0$ , or equivalently, the dimensionless capillary radius  $\hat{R} = \sin \theta_0$ .

Substituting the aforementioned regular perturbation expansions into the dimensionless forms of the governing equations (2.7)–(2.9), and collecting terms at successive orders in  $\varepsilon$ , yields a hierarchy of algebraic relations among the perturbation coefficients. At  $\mathcal{O}(\varepsilon)$ , we obtain the following three independent equations relating the first-order corrections  $\hat{F}_1$ ,  $\hat{\mathcal{H}}_1$ , and  $\theta_1$ :

$$\hat{\mathcal{H}}_1 \sin \theta_0 = \theta_1 \cos \theta_0 + \hat{F}_1 \csc \theta_0, \tag{2.10a}$$

$$1 - 2\hat{\mathcal{H}}_1 \cos \theta_0 = 2\theta_1 \sin \theta_0 + 2\hat{F}_1 \ln(\cot \theta_0 + \csc \theta_0), \tag{2.10b}$$

$$\hat{\mathcal{H}}_1 (\cos^3 \theta_0 - 3 \cos \theta_0) = \theta_1 \sin^3 \theta_0 - \hat{F}_1 \cos \theta_0. \tag{2.10c}$$

Similarly, at  $\mathcal{O}(\varepsilon^2)$ , the expansions yield the following three relations among the second-order coefficients  $\hat{F}_2$ ,  $\hat{\mathcal{H}}_2$ , and  $\theta_2$ :

$$\begin{aligned} \hat{\mathcal{H}}_2 \sin \theta_0 &= \theta_2 \cos \theta_0 - \frac{\theta_1^2}{2} \sin \theta_0 - \hat{F}_1 \theta_1 \cot \theta_0 \csc \theta_0 - \mathcal{F}_2 \csc \theta_0 \\ &\quad - \hat{F}_1^2 \csc^3 \theta_0, \end{aligned} \tag{2.11a}$$

$$\begin{aligned}\hat{\mathcal{H}}_1 - 2\hat{\mathcal{H}}_2 \cos \theta_0 &= \theta_1^2 \cos \theta_0 + 2\theta_2 \sin \theta_0 - 2\hat{F}_1 \theta_1 \left( \frac{\csc^2 \theta_0 + \csc \theta_0 \cot \theta_0}{\csc \theta_0 + \cot \theta_0} \right) \\ &\quad - 2\mathcal{F}_2 \ln(\cot \theta_0 + \csc \theta_0) \\ &\quad - 3\hat{F}_1^2 [\ln(\cot \theta_0 + \csc \theta_0) + \csc \theta_0 \cot \theta_0],\end{aligned}\tag{2.11b}$$

$$(\hat{\mathcal{H}}_1^2 + \hat{\mathcal{H}}_2) (\cos^3 \theta_0 - 3 \cos \theta_0) = \hat{F}_1 \theta_1 \sin \theta_0 + \frac{3\theta_1^2}{2} \cos \theta_0 \sin^2 \theta_0 + \theta_2 \sin^3 \theta_0 + \mathcal{F}_2 \cos \theta_0,\tag{2.11c}$$

where  $\mathcal{F}_2 = -(\hat{\mathcal{H}}_1 \hat{F}_1 + \hat{F}_2)$  is the second-order coefficient of the regular expansion of the dimensionless force parameter  $\mathcal{F} = -\hat{\mathcal{H}}\hat{F}$ , introduced here for notational convenience.

Simultaneous solution of the first-order system (2.10) yields closed-form expressions for the coefficients  $\hat{F}_1$ ,  $\hat{\mathcal{H}}_1$ , and  $\theta_1$  in terms of the zero-force pinning angle  $\theta_0$ :

$$\hat{F}_1 = \frac{1}{2 \left[ -\frac{\cos \theta_0}{1 + \cos^2 \theta_0} + \ln(\cot \theta_0 + \csc \theta_0) \right]},\tag{2.12a}$$

$$\hat{\mathcal{H}}_1 = \frac{1}{2 \left[ -\cos \theta_0 + (1 + \cos^2 \theta_0) \ln(\cot \theta_0 + \csc \theta_0) \right]},\tag{2.12b}$$

$$\theta_1 = \frac{1}{\sin \theta_0 - (\tan \theta_0 + \sin \theta_0 \cos \theta_0) \ln(\cot \theta_0 + \csc \theta_0)}.\tag{2.12c}$$

Likewise, solving the second-order system (2.11) yields closed-form expressions for the coefficients  $\hat{F}_2$ ,  $\hat{\mathcal{H}}_2$ , and  $\theta_2$  in terms of  $\theta_0$  and the first-order coefficients:

$$\begin{aligned}\hat{F}_2 &= -\hat{\mathcal{H}}_1 \hat{F}_1 + \left[ \hat{\mathcal{H}}_1^2 X_1 + \frac{\hat{\mathcal{H}}_1}{2} (1 + \cos^2 \theta_0) - \theta_1^2 \cos^3 \theta_0 + 2\theta_1 \hat{F}_1 \sin \theta_0 \right. \\ &\quad \left. + \hat{F}_1^2 \left\{ \frac{3}{2} X_2 (1 + \cos^2 \theta_0) - \frac{3}{2} \cos \theta_0 + X_3 \right\} \right] / X_4,\end{aligned}\tag{2.13a}$$

$$\begin{aligned}\hat{\mathcal{H}}_2 &= - \left[ \hat{\mathcal{H}}_1^2 \left\{ X_2 (2 - \sin^2 \theta_0 - \sin^4 \theta_0) - X_1 \right\} - \frac{1}{2} \hat{\mathcal{H}}_1 \right. \\ &\quad \left. + \theta_1^2 \left\{ X_2 \sin^2 \theta_0 \left( \frac{3}{2} - \sin^2 \theta_0 \right) + \cos \theta_0 \left( \frac{1}{2} - \sin^2 \theta_0 \right) \right\} \right. \\ &\quad \left. - 2\theta_1 \hat{F}_1 \sin \theta_0 (1 - X_2 \cos \theta_0) - \frac{1}{2} \hat{F}_1^2 (X_2 + X_3) \right] / X_4,\end{aligned}\tag{2.13b}$$

$$\begin{aligned}\theta_2 &= -\sin \theta_0 \cos \theta_0 \left[ \hat{\mathcal{H}}_1^2 (X_1 X_2 \sec \theta_0 + 2X_3 + \cos \theta_0) \right. \\ &\quad \left. + \hat{\mathcal{H}}_1 \csc^2 \theta_0 + \theta_1^2 \{ \cos \theta_0 (1 - X_2 \cos \theta_0) - X_3 \} \right. \\ &\quad \left. - \theta_1 \hat{F}_1 \{ X_2 (2X_3 \csc \theta_0 + \cot \theta_0 - \tan \theta_0) - \csc \theta_0 (2 + \csc^2 \theta_0) \} \right. \\ &\quad \left. + 2\hat{F}_1^2 \csc^2 \theta_0 (X_3 - X_2 \cot^2 \theta_0) \right] / X_4.\end{aligned}\tag{2.13c}$$

Here, for compactness of notation, we have introduced the auxiliary functions  $X_1 = \cos \theta_0 (2 + \sin^2 \theta_0)$ ,  $X_2 = \ln(\cot \theta_0 + \csc \theta_0)$ ,  $X_3 = \cot \theta_0 \csc \theta_0$ , and  $X_4 = (1 + \cos^2 \theta_0) \ln(\cot \theta_0 + \csc \theta_0) - \cos \theta_0$ .

Having established second-order accurate regular perturbation expansions for the force response  $\hat{F}$ , mean curvature  $\hat{\mathcal{H}}$ , and pinning angle  $\theta$  in terms of the small displacement  $\varepsilon$ , we now derive analogous expansions for the dimensionless parameterized bridge profile  $\{\hat{\mathcal{R}}(\phi), \hat{z}(\phi)\}$ , where  $\phi$  denotes the local tilt angle. In particular, substituting the expansions for  $\hat{F}$ ,  $\hat{\mathcal{H}}$ , and  $\theta$  into the parametric representations (2.5) and (2.6), the bridge profile itself admits a regular expansion in  $\varepsilon$ . Here, the leading-order terms,  $\hat{\mathcal{R}}_0(\phi) = \cos \phi$  and  $\hat{z}_0(\phi) = -\sin \phi$ , describe the undeformed spherical bridge of unit radius (i.e., radius  $R_d$  prior to non-dimensionalization), centered at the origin and defined over the angular domain  $\phi \in [\pi/2 - \theta_0, \theta_0 - \pi/2]$ .

Substituting the regular perturbation expansions of  $\hat{\mathcal{R}}(\phi)$  and  $\hat{z}(\phi)$  into the dimensionless expressions for the radial and axial profiles in Eqns. (2.5) and (2.6), respectively, and collecting terms at  $\mathcal{O}(\varepsilon)$ , we obtain the first-order corrections to the bridge shape in terms of the first-order coefficients  $\hat{F}_1$  and  $\hat{\mathcal{H}}_1$  [given in Eqns. (2.12a) and (2.12b), respectively]:

$$\hat{\mathcal{R}}_1(\phi) = -\hat{\mathcal{H}}_1 \cos \phi + \hat{F}_1 \sec \phi, \quad (2.14a)$$

$$\hat{z}_1(\phi) = \hat{\mathcal{H}}_1 \sin \phi + \hat{F}_1 \ln(\tan \phi + \sec \phi). \quad (2.14b)$$

Similarly, collecting terms at  $\mathcal{O}(\varepsilon^2)$  yields the second-order corrections to the bridge profile in terms of the second-order coefficients  $\hat{F}_2$  and  $\hat{\mathcal{H}}_2$  [provided in Eqns. (2.13a) and (2.13b), respectively], along with the first-order coefficients  $\hat{F}_1$  and  $\hat{\mathcal{H}}_1$ :

$$\hat{\mathcal{R}}_2(\phi) = -\hat{\mathcal{H}}_1 \hat{\mathcal{R}}_1 + \hat{F}_1^2 \sec^3 \phi - \hat{\mathcal{H}}_2 \cos \phi + (\hat{\mathcal{H}}_1 \hat{F}_1 + \hat{F}_2) \sec \phi, \quad (2.15a)$$

$$\hat{z}_2(\phi) = -\hat{\mathcal{H}}_1 \hat{z}_1 - \left( \frac{3}{2} \hat{F}_1^2 - \hat{\mathcal{H}}_1 \hat{F}_1 - \hat{F}_2 \right) \ln(\tan \phi + \sec \phi) - \frac{3}{2} \hat{F}_1^2 \tan \phi \sec \phi + \hat{\mathcal{H}}_2 \sin \phi. \quad (2.15b)$$

In both Eqns. (2.14) and (2.15), the local tilt angle  $\phi \in [\pi/2 - \theta, \theta - \pi/2]$ , where the pinning angle  $\theta$  is approximated via its regular perturbation expansion with first- and second-order coefficients  $\theta_1$  and  $\theta_2$  [given in Eqns. (2.12c) and (2.13c), respectively]. Taken together, these expressions furnish a complete second-order accurate parametric representation of the deformed droplet bridge in the small-strain regime.

## 2.4 Results and discussion

In Sections 2.2 and 2.3, we developed an analytical framework to estimate the dimensionless force response  $\hat{F} = F/(2\pi\gamma R_d)$ , mean curvature  $\hat{\mathcal{H}} = R_d \mathcal{H}$ , and pinning angle  $\theta$  of the droplet bridge, along with its parameterized shape  $\{\hat{\mathcal{R}}(\phi), \hat{z}(\phi)\}$  in terms of the local tilt angle  $\phi$ , under quasi-static deformation in the small-strain regime  $|\bar{\varepsilon}| = |\Delta L/L_0| \ll 1$ . The core idea underpinning this framework is that, at any displacement from the undeformed spherical state, the bridge profile can be fully characterized by the triplet  $\{\hat{F}, \hat{\mathcal{H}}, \theta\}$  [see Eqns. (2.5) and (2.6)]—parameters that admit regular perturbation expansions in the small displacement  $\varepsilon = \Delta L/R_d$  about the zero-force state. This formulation allows us to systematically express the two capillary rim boundary conditions and the bridge volume conservation constraint in terms of the bridge shape. These appear respectively as the force response equation (2.7), the capillary separation equation (2.8), and the volume constraint (2.9), which together form a closed nonlinear system (involving elliptic integrals) for determining  $\hat{F}$ ,  $\hat{\mathcal{H}}$ , and  $\theta$  at each deformation state.

Upon substituting the perturbation series for these variables into the above *shape-mediated* governing relations, we obtain a hierarchy of equations at each order in  $\varepsilon$ . This hierarchy yields a

linear system that determines the  $i^{\text{th}}$ -order corrections  $\hat{F}_i$ ,  $\hat{\mathcal{H}}_i$ , and  $\theta_i$ , for all integers  $i \geq 1$ , in terms of the lower-order coefficients, thereby incorporating *shape-mediated feedback* from preceding orders. This recursive structure enables the accurate capture of shape-mediated physics at each order. Furthermore, the triplet  $\{\hat{F}_i, \hat{\mathcal{H}}_i, \theta_i\}$  provides the corresponding corrections to the bridge shape  $\{\hat{\mathcal{R}}_i(\phi), \hat{z}_i(\phi)\}$  through their regular expansions, thus completing the description of the deformed droplet bridge profile at that order.

We now contrast our formulation with that of Sariola [3], who expressed the dimensionless force response  $\hat{F}$  as a function of the Kenmotsu parameter  $B$ —a dimensionless quantity that characterizes the bulging of the bridge [120]—and the dimensionless mean curvature  $\hat{\mathcal{H}}$ , i.e.,  $\hat{F} = \hat{F}(B, \hat{\mathcal{H}})$ . They then expanded  $\hat{F}$  as a Taylor series in the small displacement  $\varepsilon$  about the undeformed state. At  $\mathcal{O}(\varepsilon)$ , by accounting for variations in both  $B$  and  $\hat{\mathcal{H}}$ , their coefficient coincided with our first-order force coefficient  $\hat{F}_1$ .

However, at  $\mathcal{O}(\varepsilon^2)$ , they considered only variations in  $B$  while neglecting nonzero contributions from first-order changes in  $\hat{\mathcal{H}}$ . Consequently, their model omits contributions to the leading-order nonlinear force arising from mean-curvature evolution at the linear order. Moreover, by formulating  $\hat{F}$  solely as a function of  $B$  and  $\hat{\mathcal{H}}$  and assuming no explicit dependence on the pinning angle  $\theta$ , their analysis lacks a mechanism to incorporate shape-mediated feedback from  $\theta$  variations. These omissions result in an incomplete characterization of the leading-order nonlinear physics at  $\mathcal{O}(\varepsilon^2)$ , as evidenced by the discrepancies between their predictions and ours in Fig. 2.2(a).

To emphasize further, our second-order (quadratic) perturbation model accurately reproduces the force response  $\hat{F}$  obtained from the numerical solution of the Young–Laplace equation across the full compression range (i.e., until the pinning angle reaches  $\theta = 180^\circ$ ) and up to  $\varepsilon \approx 0.55$  during dilation for the representative CCFA mean capillary radius  $\hat{R} = 0.45$ . In contrast, the second-order Taylor expansion of Sariola [3] performs only marginally better than the linear model of Kusumaatmaja and Lipowsky [2], capturing only the near-linear segment of the force–displacement curve. Although their curve begins to bend toward the numerical solution in the nonlinear regime, it substantially underestimates the leading-order nonlinear response owing to the partial omission of first-order shape feedback at  $\mathcal{O}(\varepsilon^2)$ .

Following the above discussion, to the best of our knowledge, our framework provides the first analytical expressions that are both simple and accurate in capturing the leading-order nonlinear, shape-mediated effects on the force response of a pinned droplet or capillary bridge under quasi-static deformation in the small-strain limit. As a useful byproduct, it also yields the leading nonlinear corrections to the mean curvature and pinning angle, thereby enabling closed-form approximations of the bridge profile without requiring numerical solutions of the nonlinear Young–Laplace equation. Moreover, the physically grounded methodology we adopt to derive the regular perturbation corrections to the force response, mean curvature, pinning angle, and bridge shape at each order follows a consistent structure, and hence, can, in principle, be extended systematically to higher orders.

Such higher-order expansions are expected to further improve the accuracy of the model, potentially capturing the nonlinear behaviour up to  $\bar{\varepsilon} \approx 1$  during dilation. However, since the present second-order expansion already performs well across the entire compression range [see Fig. 2.3(b)] and up to moderate dilation [see Fig. 2.3(a)], the added algebraic complexity of higher-order terms offers limited practical benefit. Furthermore, these higher-order corrections are not expected to reveal any fundamentally new nonlinear physics beyond what is already captured at the leading nonlinear (second) order. For these reasons, we restrict our analysis to second-order perturbation expansions. The accuracy of the model and the nonlinear physics it captures are discussed in detail in the following subsections.

### 2.4.1 Force response

We recall that the dimensionless force response  $\hat{F}$  is approximated as a regular perturbation expansion in the small displacement  $\varepsilon$ , with the first- and second-order corrections  $\hat{F}_1$  and  $\hat{F}_2$  given by Eqns. (2.12a) and (2.13a), respectively. The first-order correction  $\hat{F}_1$  captures the linear behaviour of the force response and recovers the dimensionless linear spring constant  $-k/(2\pi \sum_{\alpha\beta})$  reported by Kusumaatmaja and Lipowsky [2] (with interfacial tension  $\gamma$  denoted by  $\sum_{\alpha\beta}$ ) and  $-k_1/(2\pi\gamma)$  reported by Sariola [3] for an axisymmetric pinned bridge between plates with equal contact radii. Despite employing different modeling approaches, this universal agreement at first order arises because all models begin from the common undeformed spherical bridge and capture the linear correction to the force due to small deviations from this base state toward an unduloid.

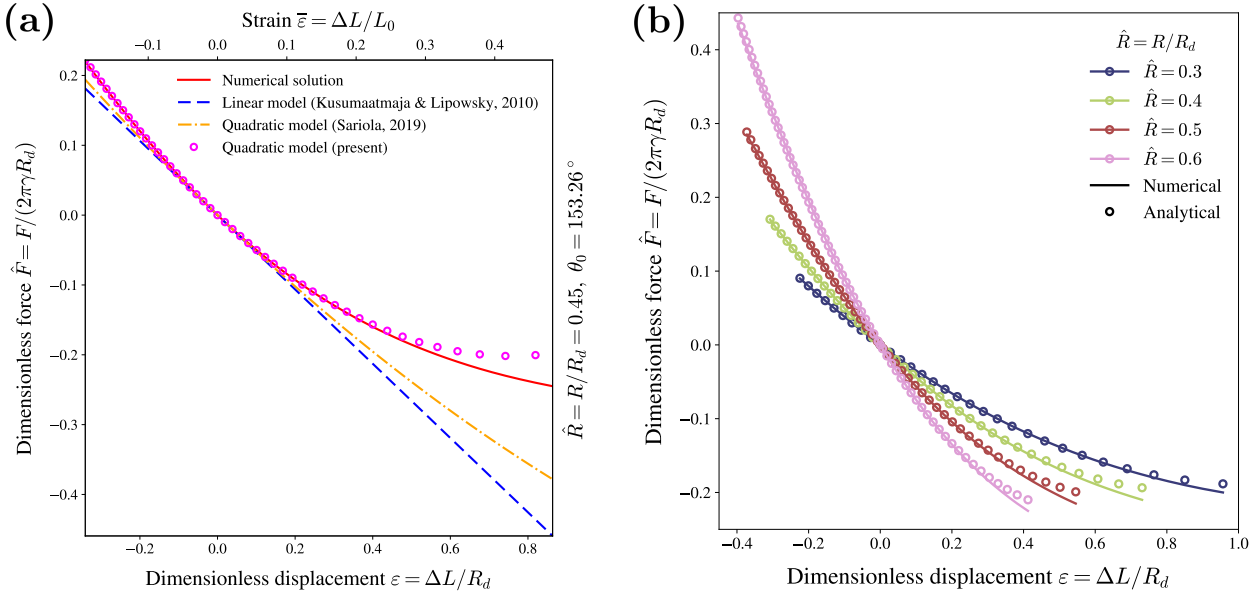


**Figure 2.2:** (a) Dimensionless force response  $\hat{F} = F/(2\pi\gamma R_d)$  versus displacement  $\varepsilon = \Delta L/R_d$  (bottom axis) and strain  $\bar{\varepsilon} = \Delta L/L_0$  (top axis) for capillary radius  $\hat{R} = R/R_d = 0.45$ . The numerical Young–Laplace solution (*solid red*) is compared with the linear model of Kusumaatmaja and Lipowsky [2] (*blue dashed*), the quadratic model of Sariola [3] (*orange dash-dot*), and the present second-order asymptotic approximation (*magenta open circles*). Curves are shown up to the compression limit ( $\theta = 180^\circ$ ) and to the onset of dilation where the present model departs from the numerical solution. (b) Numerical  $\hat{F}$  plotted against  $\varepsilon$  across the CCFA-relevant range:  $\hat{R} \in \{0.3, 0.4, 0.5, 0.6\}$  (*solid lines, distinct colours*), overlaid with *matching-colour open circles* from the present asymptotic model. Truncation limits as in panel (a).

Kusumaatmaja and Lipowsky [2] derived the linear force response by first parameterizing the bridge profile in terms of the tilt angle  $\phi$  and expressing the capillary rim boundary conditions and the volume constraint using this parameterized shape, analogous to Eqns. (2.5)–(2.9) in our formulation. However, rather than perturbing these governing relations in the small displacement  $\varepsilon$  or strain  $\bar{\varepsilon}$ , they expanded them in the small dimensionless force parameter  $\mathcal{F} = -F\mathcal{H}/(2\pi\gamma)$  [denoted  $\epsilon$  in their notation] to first-order, and subsequently employed a sequence of systematic elimination steps to remove the first-order variations in mean curvature and pinning angle (denoted  $\Delta M$  and  $\Delta\theta$  in their formulation) from the resulting expressions. This ultimately yielded a linear force-displacement relation of the form  $\hat{F} = \left(-k/2\pi \sum_{\alpha\beta}\right)\varepsilon$ .

On the other hand, Sariola [3] adopted the Kenmotsu parameterization of the bridge profile in terms of the meridional arc-length coordinate  $s$ , where the shape is fully specified by the Kenmotsu

bulge parameter  $B$  [120], mean curvature  $\mathcal{H}$ , and pinning angle  $\theta$ . This formulation enabled them to write the rim boundary conditions and volume constraint in terms of  $B$ ,  $\mathcal{H}$ , and  $\theta$ , and led to the expression for the force response:  $F(B, \mathcal{H}) = \pi\gamma(B^2 - 1)/(2\mathcal{H})$ . As discussed earlier, this representation does not include an explicit dependence on the pinning angle  $\theta$ , despite  $\theta$  being one of the key parameters controlling the bridge geometry. They then performed a Taylor expansion of this force equation in  $\varepsilon$  about the undeformed (spherical) state, obtaining the dimensionless linear spring constant  $-k_1/(2\pi\gamma)$ .

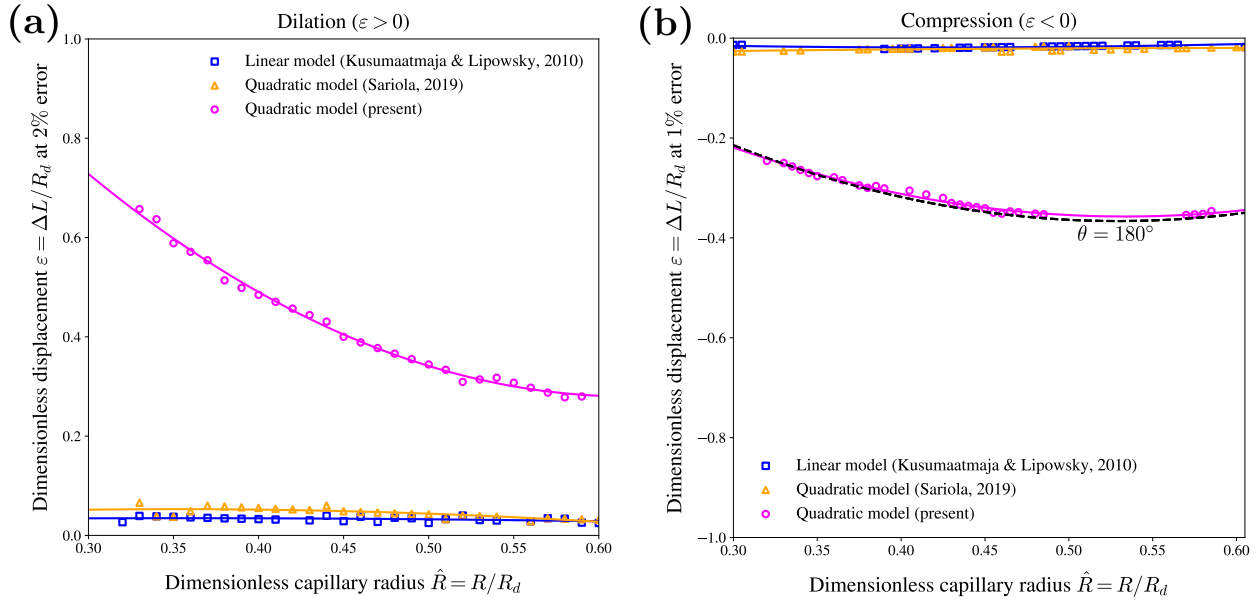


**Figure 2.3:** (a,b) Dimensionless displacement  $\varepsilon = \Delta L/R_d$  at which the % relative error between the analytical models and the numerical solution,  $100 \times |\hat{F}_{\text{analytical}}/\hat{F}_{\text{numerical}} - 1|$ , reaches a fixed threshold, plotted against capillary radius  $\hat{R} = R/R_d$ . (a) Dilation threshold 2%; (b) compression threshold 1%. Models: Kusumaatmaja and Lipowsky [2] (blue squares), Sariola [3] (orange triangles), present second-order asymptotic model (magenta open circles); solid lines (with colours matching the markers) are quadratic fits. The capillary radius is varied over the CCFA-relevant range  $\hat{R} \in [0.3, 0.6]$ . The chosen error thresholds correspond to the smallest values for which all models yield consistent, non-fluctuating trends across the entire radius range. The black dashed line in panel (b) indicates the point of maximum compression ( $\theta = 180^\circ$ ).

We now turn to the second-order correction to the force response  $\hat{F}_2$ . As evident from Eqn. (2.9) and as discussed previously, this coefficient captures contributions from both the undeformed shape—via  $\theta_0$  and  $\hat{\mathcal{H}}_0 = 1$ —and the first-order shape through the corrections  $\hat{F}_1$ ,  $\hat{\mathcal{H}}_1$ , and  $\theta_1$ . In addition,  $\hat{F}_2$  is coupled to the second-order corrections  $\hat{\mathcal{H}}_2$  and  $\theta_2$  through the  $\mathcal{O}(\varepsilon^2)$  boundary conditions and volume constraint given in Eqn. (2.11). Owing to this hierarchical coupling,  $\hat{F}_2$  naturally incorporates shape-mediated feedback from lower-order terms and therefore captures the correct leading-order nonlinear behaviour of the force response. This is validated in Fig. 2.2(a), which shows close agreement between our quadratic perturbation expansion and the numerical solution of the Young–Laplace equation across both the compression ( $\varepsilon < 0$ ,  $\hat{F} > 0$ ) and dilation ( $\varepsilon > 0$ ,  $\hat{F} < 0$ ) regimes for a capillary with the CCFA mean radius  $\hat{R} = 0.45$ .

As anticipated, all three models—our second-order perturbation expansion, the linear theory of Kusumaatmaja and Lipowsky [2], and the quadratic Taylor expansion of Sariola [3]—coincide with the numerical curve in the linear regime. However, as previously pointed out, the second-order correction in the formulation of Sariola [3], which corresponds to the dimensionless quadratic spring constant  $-k_2/(2\pi\gamma/R_d)$ , neglects the first-order shape corrections arising from variations in

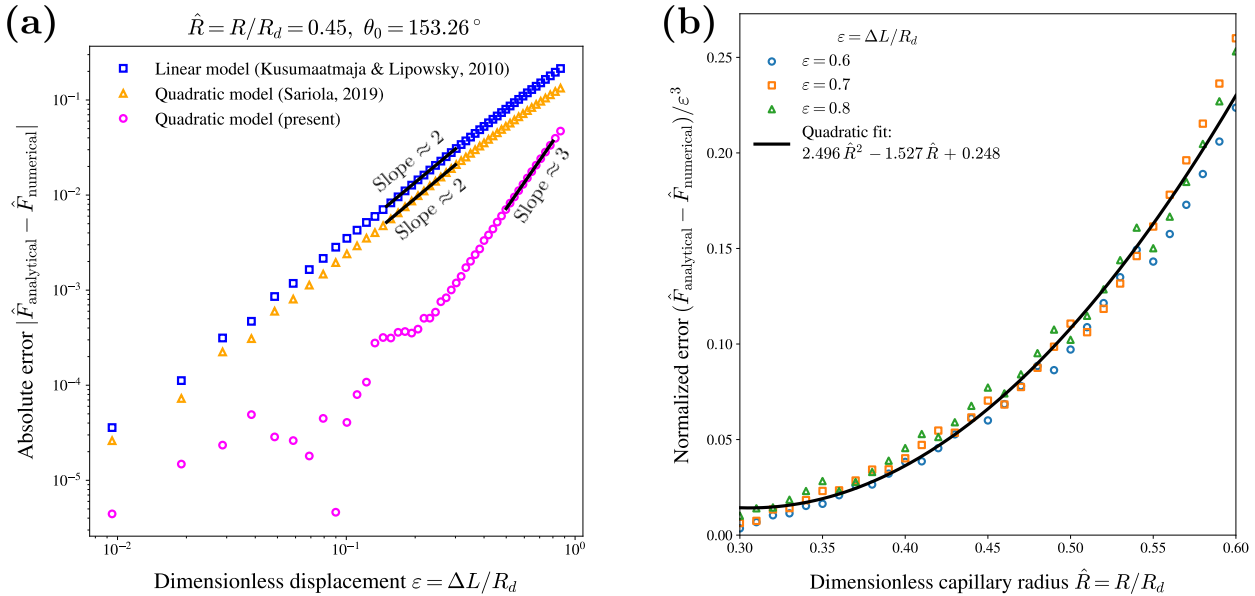


**Figure 2.4:** (a) Log–log plot of the absolute error between the analytical models and the numerical solution versus displacement  $\varepsilon$  during dilation for capillary radius  $\hat{R} = R/R_d = 0.45$ . Models: Kusumaatmaja and Lipowsky [2] (blue squares), Sariola [3] (orange triangles), and the present quadratic model (magenta circles). Linear fits (black solid line) to the error curves over the range  $\varepsilon \in [0.15, 0.3]$  for the first two models yield slopes of 2.00 and 2.01, respectively. For the present model, the linear fit over the range  $\varepsilon \in [0.5, 0.8]$  (where the errors stabilize) yields a slope of 3.47. (b) Error between the present model and the numerical model, normalized by  $\varepsilon^3$ , plotted versus  $\hat{R}$  for  $\varepsilon = 0.6$  (circles), 0.7 (squares), and 0.8 (triangles). Data points collapse onto a single quadratic fit (black solid line):  $2.496 \hat{R}^2 - 1.527 \hat{R} + 0.248$ .

mean curvature and pinning angle, retaining only the dependence on the bulge parameter  $B$ . As a result, it fails to capture the correct leading-order nonlinear physics at  $\mathcal{O}(\varepsilon^2)$  and substantially underestimates the force response in the nonlinear region, offering only a modest improvement over the linear model. To further assess the robustness of our approach, we compared our model with the numerical solution for capillary radii spanning the entire CCFA range:  $\hat{R} = 0.3, 0.4, 0.5$ , and 0.6. As shown in Fig. 2.2(b), our model exhibits excellent agreement with the numerical solution in the nonlinear regime for both compression and dilation across all considered capillary radii.

Before proceeding further with our discussion, we briefly outline the scheme used to obtain the numerical solution cited in the previous paragraph. The parameterized bridge profile  $\{\hat{\mathcal{R}}(\phi), \hat{z}(\phi)\}$  is reformulated in terms of the dimensionless curvilinear arc length  $s$  (measured from the left capillary rim at  $\hat{z} = -\hat{L}/2$ ), yielding the shape variables  $\{\hat{\mathcal{R}}(s), \hat{z}(s), \phi(s)\}$ . This transformation leads to the following system of three ODEs that govern the bridge shape at any specified force  $\hat{F}$ :

$$\frac{d\hat{\mathcal{R}}}{ds} = \sin \phi, \quad \frac{d\hat{z}}{ds} = \cos \phi, \quad \frac{d\phi}{ds} = -\frac{1}{\hat{\mathcal{R}}} \left( \cos \phi + \frac{2\hat{F}}{\hat{\mathcal{R}}} \right). \quad (2.16)$$

The first two equations in (2.16) are obtained from the definition of the dimensionless differential arc length  $ds = \sqrt{(d\hat{\mathcal{R}})^2 + (d\hat{z})^2}$  and the geometric slope relation  $d\hat{\mathcal{R}}/d\hat{z} = \tan \phi$ . The third equation is derived by expressing the Young–Laplace equation (2.1) in terms of the tilt angle  $\phi$  and its derivative  $d\phi/ds$ , yielding  $2\hat{\mathcal{H}} = \cos \phi/\hat{\mathcal{R}} - d\phi/ds$ . This expression is then combined with the first integral (2.2) and the force relation (2.4), resulting in the equivalent form  $2\hat{\mathcal{H}} = \cos \phi/\hat{\mathcal{R}} + \hat{F}/\hat{\mathcal{R}}^2$ .

The origin of the axisymmetric cylindrical coordinate system is placed at the left capillary rim

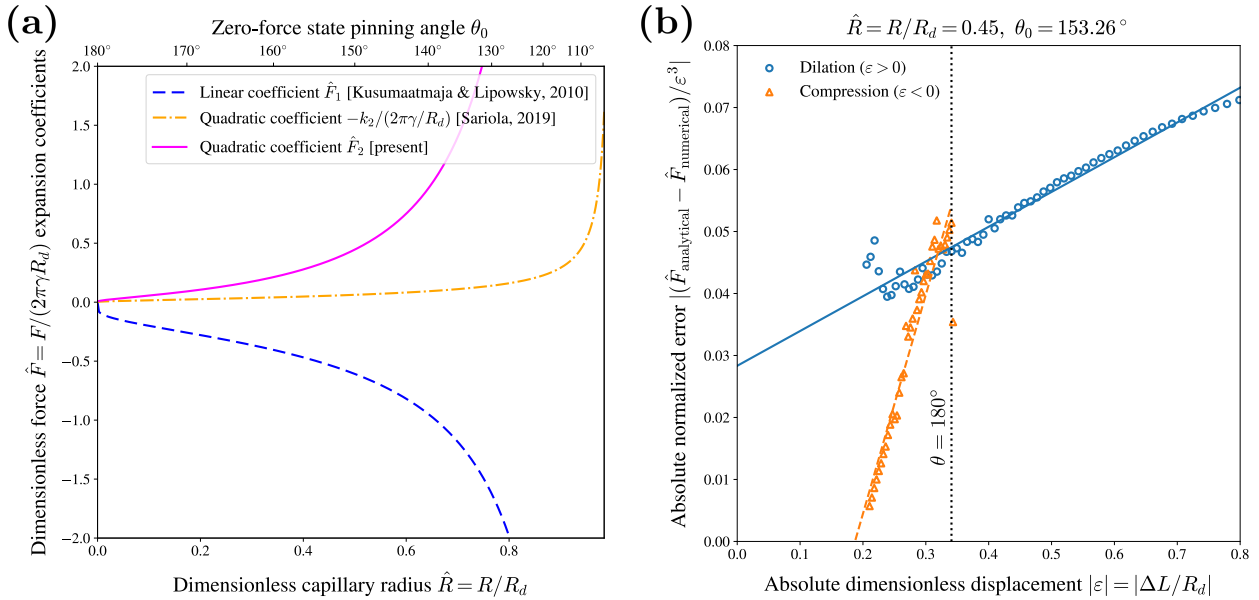


**Figure 2.5:** (a) First- (linear) and second-order (quadratic) coefficients of the regular perturbation expansion for the dimensionless force response  $\hat{F}$ , denoted  $\hat{F}_1$  (blue dashed) and  $\hat{F}_2$  (magenta solid), plotted versus capillary radius  $\hat{R} \in [0, 1]$  [bottom axis] and the corresponding zero-force pinning angle  $\theta_0$  (top axis). Also shown is the quadratic coefficient of Sariola [3] (orange dash-dot-dash), given by  $-k_2/(2\pi\gamma/R_d)$ . (b) Absolute normalized error between the present analytical model and the numerical solution,  $|(\hat{F}_{\text{analytical}} - \hat{F}_{\text{numerical}})/\varepsilon^3|$ , plotted versus the absolute displacement  $|\varepsilon| = |\Delta L/R_d|$  for dilation (circles) and compression (triangles) at the CCFA mean radius  $\hat{R} = 0.45$ . Solid lines (with colours matching the markers) are linear fits. The vertical black dotted line marks the absolute displacement at the maximum compression limit ( $\theta = 180^\circ$ ).

plane, and the ODE system is solved for a given force  $\hat{F}$  using the RK45 scheme, subject to the initial conditions  $\hat{\mathcal{R}}(s=0) = \hat{R}$ ,  $\hat{z}(s=0) = 0$ , and  $\phi(s=0) = \theta - \pi/2$ . The solver proceeds until the bridge profile intersects the right capillary rim, defined by the boundary condition  $\hat{\mathcal{R}}(\hat{z} = \hat{L}) = \hat{R}$ . The unknown pinning angle  $\theta$  is iteratively adjusted (initially sampled from the interval  $[\pi/2, \pi]$ ), and the system is solved repeatedly while calculating the bridge volume  $\hat{V}_b$  via the trapezoidal rule, until it matches the zero-force state bridge volume [Eqn. (2.9)] within a relative tolerance of  $10^{-6}$ . Finally, the stopping point value of  $\hat{z}$  is extracted, giving us the capillary separation  $\hat{L}$ . The deviation of this value from the undeformed separation  $\hat{L}_0$  provides the dimensionless displacement  $\varepsilon$ .

Returning to our discussion, it is of practical importance for experimentalists to have the knowledge of the range of dimensionless displacement  $\varepsilon$  (in both dilation and compression) over which our quadratic asymptotic expansion remains accurate enough to replace a full numerical solution. It is also useful to quantify the additional displacement range our model captures, compared with the linear model of Kusumaatmaja and Lipowsky [2] and the quadratic model of Sariola [3]. This question is addressed in Fig. 2.3, where we plot the dimensionless displacement  $\varepsilon$  as a function of the capillary radius  $\hat{R}$  at which the percentage relative error between the analytical and numerical force response,  $100 \times |\hat{F}_{\text{analytical}}/\hat{F}_{\text{numerical}} - 1|$ , reaches 2% for dilation [panel (a)] and 1% for compression [panel (b)]. These tolerances were chosen as the smallest values for which the relative errors across all capillary radii in the CCFA-relevant range,  $\hat{R} \in [0.3, 0.6]$ , yield a smooth and interpretable trend without significant fluctuations.

During dilation, all three models exhibit the trend that smaller capillary radii permit larger displacements before reaching the prescribed error threshold. This observation can be attributed to

the fact that larger capillary radii facilitate greater deviation from the undeformed spherical state, i.e., more pronounced shape changes, for a given displacement. This effect is compounded by the steeper gradients  $d\hat{F}/d\varepsilon$ ,  $d\hat{\mathcal{H}}/d\varepsilon$ , and  $d\theta/d\varepsilon$  with increasing radius  $\hat{R}$ , as shown in Figs. 2.2(b), 2.6(a), and 2.6(b), respectively. Consequently, our second-order asymptotic expansion becomes relatively insufficient for larger radii at smaller displacements, as it fails to capture the rapidly evolving shape beyond the shown threshold displacement, and higher-order corrections would be required to improve accuracy.

Nonetheless, it is important to highlight that both the linear model of Kusumaatmaja and Lipowsky [2] and the quadratic model of Sariola [3] exceed the 2% error threshold even at  $\varepsilon = 0.1$  (corresponding to a strain  $\bar{\varepsilon} = \Delta L/L_0 < 0.05$ ), limiting their utility for experiments. In contrast, our model remains within the 2% error margin up to  $\varepsilon = 0.7$  for  $\hat{R} = 0.3$ , and up to  $\varepsilon = 0.3$  for  $\hat{R} = 0.6$ , corresponding to strains of  $\bar{\varepsilon} \approx 0.4$  and 0.2, respectively—representing a substantial improvement over the earlier models. In compression, both Kusumaatmaja and Lipowsky [2] and Sariola [3] exhibit relative errors exceeding 1% for  $\varepsilon > 0.05$  across all capillary radii. In contrast, our model stays within the 1% threshold nearly up to the maximum compression limit, i.e., until the pinning angle approaches  $\theta = 180^\circ$ . This confirms that our asymptotic model accurately captures the entire compression range for all capillary radii commonly used in CCFA experiments.

Having established that our model significantly extends the range of dimensionless displacement  $\varepsilon$  over which it agrees with the numerical solution—compared to the linear model of Kusumaatmaja and Lipowsky [2] and the quadratic model of Sariola [3]—we now turn to the question of whether it also correctly captures the leading-order nonlinear physics. There are two ways to assess this. First, since our regular asymptotic expansions are truncated at second order, the absolute error between our analytical model and the numerical solution is expected to scale as  $\varepsilon^3$ . This implies that, at a fixed capillary radius  $\hat{R}$ , a log–log plot of the absolute error in the force response versus  $\varepsilon$  should exhibit a linear trend with slope approximately equal to 3.

This prediction is confirmed in Fig. 2.4(a), which shows the absolute error in force response between our model and the numerical solution as a function of  $\varepsilon$  on a log–log scale for the CCFA mean radius  $\hat{R} = 0.45$ . After an initial transient, the error falls along a straight line with slope  $3.47 \approx 3$ , consistent with the expected  $\mathcal{O}(\varepsilon^3)$  error scaling. Repeating the same analysis for the linear model of Kusumaatmaja and Lipowsky [2] yields a slope of 2.00, confirming that its error scales as  $\varepsilon^2$ , as anticipated. However, applying this analysis to the quadratic model of Sariola [3] produces a slope of  $2.01 \approx 2$ , indicating that this model fails to capture the correct leading-order nonlinear behaviour, offering only a marginal improvement over the linear model.

The second way to establish that our model admits an error scaling as  $\varepsilon^3$  is by noting that the error between the analytical and numerical solution at a fixed displacement  $\varepsilon$ , when normalized by  $\varepsilon^3$ , becomes  $\mathcal{O}(1)$ . In other words, this normalized error should depend solely on the capillary radius  $\hat{R}$ , or equivalently, the zero-force state pinning angle  $\theta_0$ . Consequently, the curve of this normalized error versus capillary radius  $\hat{R}$  should be independent of the chosen value of  $\varepsilon$ .

This prediction is confirmed in Fig. 2.4(b), which plots the normalized error in the force response as a function of  $\hat{R}$  over the CCFA-relevant range  $\hat{R} \in [0.3, 0.6]$  for three different dilations:  $\varepsilon = 0.6$ , 0.7, and 0.8. All three curves closely collapse onto a single quadratic trend, represented by the solid black fit line. The monotonic increase of this fit further reestablishes that, at any given displacement, the error grows with capillary radius. Moreover, since the normalized error remains strictly positive, we conclude that the perturbation expansion of the force response consistently overestimates the numerical solution as and when it diverges.

We now analyze the behaviour of the first-order coefficient  $\hat{F}_1$  of the force response, corresponding to the dimensionless linear spring constant  $-k/(2\pi\gamma)$  reported by Kusumaatmaja and Lipowsky [2], along with the second-order coefficient  $\hat{F}_2$ , and the quadratic coefficient (dimensionless quadratic

spring constant)  $-k_2/(2\pi\gamma/R_d)$  derived by Sariola [3], as functions of the capillary radius  $\hat{R}$ . As shown in Fig. 2.5(a), each of these coefficients tends to zero as  $\hat{R} \rightarrow 0$  (equivalently, as  $\theta_0 \rightarrow 180^\circ$ ), consistent with the zero force response in this limit. The first-order coefficient  $\hat{F}_1$  decreases monotonically with increasing  $\hat{R}$  and diverges to  $-\infty$  as  $\hat{R} \rightarrow 1$ . This trend captures that the force–displacement slope,  $d\hat{F}/d\varepsilon \approx \hat{F}_1$ , becomes steeper with increasing capillary radius, suggesting that the incremental force required to move between two equilibrium states also increases.

In other words, it requires less mechanical effort to deform a droplet between two equilibrium states using a smaller capillary than a larger one. Equivalently, a smaller displacement is sufficient to induce a given change in the force response with a larger capillary than with a smaller one, as can be observed in Fig. 2.2(b). In the limiting case  $\hat{R} \rightarrow 1$ , where the capillary radius approaches that of the undeformed droplet, the divergence of  $\hat{F}_1 \rightarrow -\infty$  implies that an extremely large force is required to move between equilibrium states—reflecting the increasing stiffness of the droplet in this regime.

A key limitation of the linear coefficient  $\hat{F}_1$  is that it predicts a symmetric force response, yielding equal and opposite forces for compression ( $-\varepsilon$ ) and dilation ( $\varepsilon$ ). Owing to its constant slope, it also implies that the incremental force required to transition between consecutive equilibrium states remains uniform. This symmetry does not hold in practice and is broken by the second-order (quadratic) coefficient  $\hat{F}_2$ . Similar in behaviour to  $\hat{F}_1$  up to a sign change,  $\hat{F}_2$  increases monotonically with capillary radius and diverges to  $+\infty$  as  $\hat{R} \rightarrow 1$ .

First, this implies that the force–displacement slope, given by  $d\hat{F}/d\varepsilon \approx \hat{F}_1 + 2\varepsilon\hat{F}_2$ , increases in magnitude with decreasing  $\varepsilon$  at fixed capillary radius. Physically, this means that the incremental force required to move between neighbouring equilibrium states grows as the droplet is compressed away from the zero-force state, and diminishes as it is dilated (see Fig. 2.8). As a result, the dilation–compression symmetry is broken, and it is energetically easier to dilate the droplet between two equilibrium positions than to compress it by the same amount.

Second, the rate of change of the force–displacement slope at fixed  $\varepsilon$ , given by  $d^2\hat{F}/d\varepsilon^2 \approx 2\hat{F}_2$ , increases with capillary radius. Thus, the incremental force required between successive displacements varies more rapidly for larger capillaries than for smaller ones. These trends are clearly reflected in Figs. 2.2(a) and (b). In the limiting case  $\hat{R} \rightarrow 1$ , the divergence of  $\hat{F}_2 \rightarrow +\infty$  remains consistent with the increasing stiffness of the droplet under deformation, while also capturing the stronger resistance to compression relative to dilation—an asymmetry not accounted for by the linear approximation alone.

From the preceding discussion, we conclude that the incremental force required to displace a droplet between adjacent equilibrium states increases under compression and decreases under dilation, with this incremental force at each displacement step growing with capillary radius (see Fig. 2.10). Equivalently, the displacement required to achieve a given change in force response decreases with increasing compression and capillary radius, and increases under dilation and for smaller capillaries (see Fig. 2.9). It is therefore energetically most expensive to compress a droplet from its undeformed state using a large capillary, with the incremental energy cost rising at each successive compression step. Conversely, it is energetically least expensive to dilate a droplet using a small capillary, with the incremental energy cost decreasing as dilation progresses.

Furthermore, the first-order coefficient  $\hat{F}_1$  predominantly sets the magnitude of the force response and may thus be interpreted as a “magnitude mode”, while the second-order coefficient  $\hat{F}_2$  governs the breaking of symmetry between compression and dilation, thereby introducing nonlinear effects and serving as a “deformation-type mode”. As a brief remark, we note that the quadratic coefficient proposed by Sariola [3] exhibits the same qualitative trend as  $\hat{F}_2$ , but remains close to zero across much of the capillary radius range. As such, it provides only a marginal correction to the linear approximation—capturing the correct qualitative physical trends but failing to account

quantitatively for the underlying nonlinear behaviour.

We have already established in Fig. 2.3(b) that our second-order asymptotic model captures the nonlinear behaviour of the droplet accurately under compression, up to the maximum compression limit, i.e., when  $\theta = 180^\circ$ , across all CCFA relevant capillary radii  $\hat{R} \in [0.3, 0.6]$ . In addition to this quantitative validation, Figs. 2.2(a) and (b) suggest a qualitative trend: at a given displacement  $\varepsilon$  within the admissible compression regime, the asymptotic expansion for the force response appears to agree more closely with the numerical solution during compression than during dilation at  $-\varepsilon$ . This observation is quantitatively confirmed in Fig. 2.5(b), where we plot the absolute normalized error between the analytical and numerical force responses, defined as  $|(\hat{F}_{\text{analytical}} - \hat{F}_{\text{numerical}})/\varepsilon^3|$ , for the CCFA mean capillary radius  $\hat{R} = 0.45$ .

We find that the error is slightly lower in compression than in dilation at the same absolute displacement  $|\varepsilon|$ . This asymmetry in accuracy can be attributed to the higher-order corrections, particularly the third- and fourth-order coefficients,  $\hat{F}_3$  and  $\hat{F}_4$ , since the normalized error scales as  $|\hat{F}_3 + \varepsilon \hat{F}_4|$ . In fact, as we established through Fig. 2.4(b) that the asymptotic expansion consistently overestimates the numerical solution once the deviation begins, implies that both  $\hat{F}_3$  and  $\hat{F}_4$  are positive at  $\hat{R} = 0.45$ . Since this trend is found to hold across the entire CCFA-relevant range of capillary radii, we conclude that the same asymptotic structure—namely, positive  $\hat{F}_3$  and  $\hat{F}_4$ —persists throughout.

#### 2.4.2 Mean curvature and pinning angle

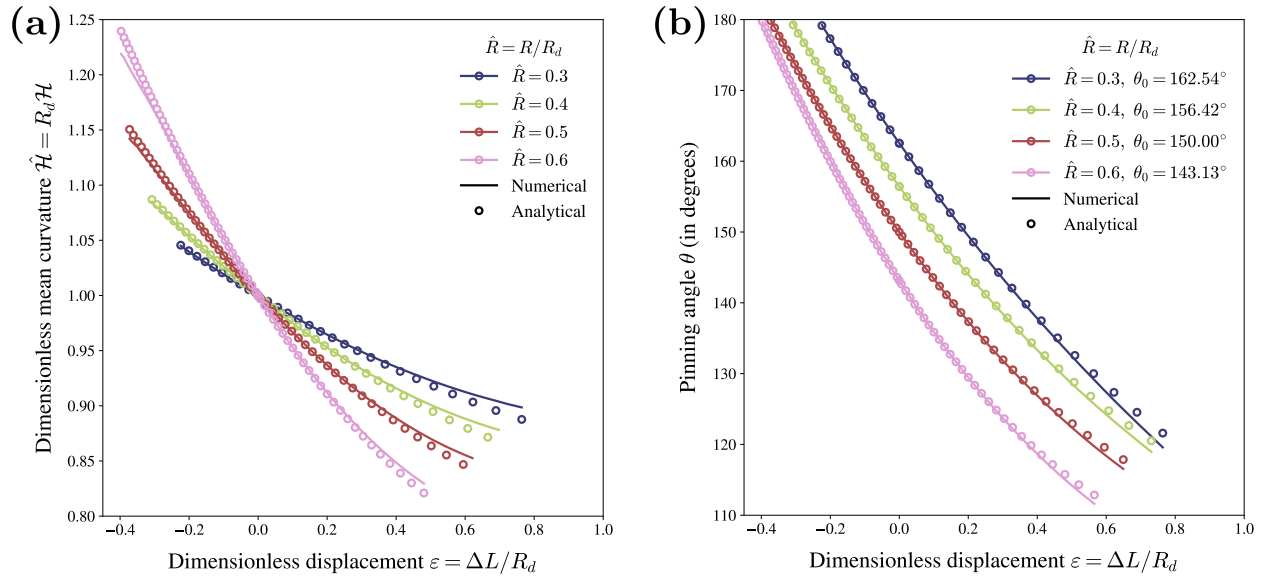


**Figure 2.6:** (a) Numerical profiles of the dimensionless mean curvature  $\hat{\mathcal{H}} = R_d \mathcal{H}$  versus displacement  $\varepsilon = \Delta L / R_d$  for capillary radii  $\hat{R} \in \{0.3, 0.4, 0.5, 0.6\}$  (solid lines, distinct colours), spanning the CCFA-relevant range. Corresponding present asymptotic model curves are overlaid as *matching-colour open circles*. Curves are shown up to the compression limit ( $\theta = 180^\circ$ ) and to the dilation range beyond which the asymptotic model deviates from the numerical solution. (b) The same comparison is presented for the pinning angle  $\theta$  (in degrees) plotted versus  $\varepsilon$ , using the same line/marker conventions.

We recall that the dimensionless mean curvature  $\hat{\mathcal{H}}$  and pinning angle  $\theta$  are expressed as regular perturbation expansions in the small displacement  $\varepsilon$ , with the first-order corrections,  $\hat{\mathcal{H}}_1$  and  $\theta_1$ , given by Eqns. (2.12b) and (2.12c), and the second-order corrections,  $\hat{\mathcal{H}}_2$  and  $\theta_2$ , by Eqns. (2.13b)

and (2.13c). To assess the accuracy of these asymptotic expansions, we compare them against numerical results obtained using the RK45 scheme for capillary radii  $\hat{R} = 0.3, 0.4, 0.5$ , and  $0.6$ . The corresponding comparisons for  $\hat{\mathcal{H}}$  and  $\theta$  are shown in Figs. 2.6(a) and (b), respectively. We find that the regular expansions for both  $\hat{\mathcal{H}}$  and  $\theta$  accurately capture the expected physical trends: as the droplet is compressed away from the undeformed (zero-force) state, the incremental changes in mean curvature and pinning angle associated with transitions between equilibrium states increase; conversely, these incremental changes decrease as the droplet is dilated.

Moreover, these incremental variations grow with increasing capillary radius. This behaviour is physically consistent and provides mechanistic support for our earlier discussion on the force response: it explains why compression requires more force than dilation, and why transitions between equilibrium states become increasingly energetically unfavourable with larger capillary radii. In analogy with the force response coefficients, the first-order corrections  $\hat{\mathcal{H}}_1$  and  $\theta_1$  primarily determine the magnitude of the mean curvature and pinning angle, respectively, while the second-order coefficients  $\hat{\mathcal{H}}_2$  and  $\theta_2$  govern the asymmetry between compression and dilation, thereby introducing nonlinear effects.

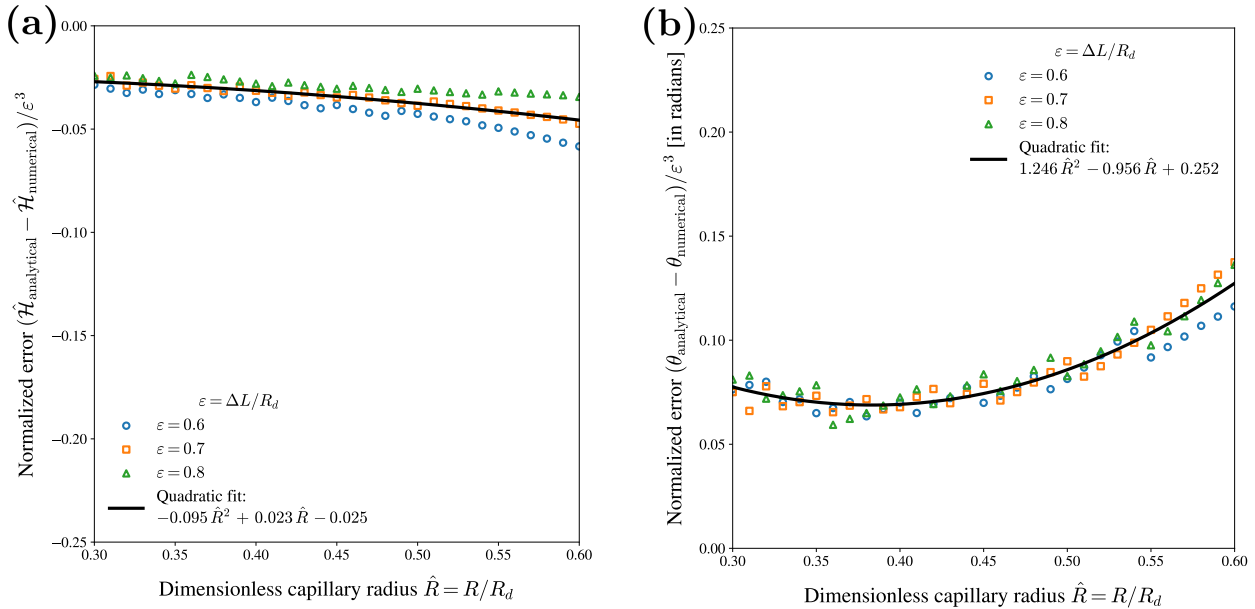


**Figure 2.7:** Normalized error between second-order asymptotic predictions and numerical results for (a) the mean curvature and (b) pinning angle, plotted versus capillary radius  $\hat{R} = R/R_d$  for displacements  $\varepsilon = 0.6$  (circles),  $0.7$  (squares), and  $0.8$  (triangles). Errors are normalized by  $\varepsilon^3$ . In both panels, the data collapse onto a single quadratic fit (black solid line), consistent with cubic error scaling in displacement. Fitted curves: mean curvature  $-0.095\hat{R}^2 + 0.023\hat{R} - 0.025$ ; pinning angle  $1.246\hat{R}^2 - 0.956\hat{R} + 0.252$ .

As with the order-of-accuracy validation for the perturbation expansion of the force response shown in Fig. 2.2(b), we now confirm, for completeness, that the second-order asymptotic expansions of the mean curvature and pinning angle also exhibit an error that scales as  $\varepsilon^3$ . This is demonstrated in Figs. 2.7(a) and (b), where the absolute error between the asymptotically and numerically computed values of the mean curvature and pinning angle at fixed displacements  $\varepsilon = 0.6, 0.7$ , and  $0.8$  is normalized by  $\varepsilon^3$  and plotted as a function of the capillary radius  $\hat{R} \in [0.3, 0.6]$ . In both cases, the normalized error curves collapse onto a single master curve, indicating that the error depends solely on  $\hat{R}$  and confirming the expected cubic error scaling.

For the mean curvature, the normalized error is consistently negative, indicating that the asymptotic prediction underestimates the numerical result.

totic expansion underestimates the true mean curvature in the regime where deviations from the numerical solution occur. Furthermore, the monotonic decrease of the quadratic fit (shown as a solid black line) implies that the absolute error increases with increasing capillary radius—consistent with the trend observed in the force response. On the other hand, the normalized error for the pinning angle remains strictly positive, indicating that the asymptotic expansion overestimates the true pinning angle when deviations arise. However, the corresponding quadratic fit is non-monotonic: the error initially decreases with increasing  $\hat{R}$  up to  $\hat{R} \approx 0.38$ , beyond which it exhibits the expected trend of increasing with capillary radius.

### 2.4.3 Bridge shape

We dedicate this section to validating that the second-order asymptotic expansion for the parameterized bridge shape,  $\{\hat{\mathcal{R}}(\phi), \hat{z}(\phi)\}$ , obtained from the first- and second-order corrections in Eqns. (2.14) and (2.15), approximate the true bridge shape well beyond the linear regime and consistently capture the physical trends discussed in the preceding sections. Figs. 2.8(a)–(e) show a comparison between the analytically and numerically computed profiles as the droplet evolves from the undeformed state [panel (c)] to its maximum compression limit, corresponding to  $\theta = 180^\circ$  [panel (a)], and to an equally dilated state [panel (e)]. The capillary radius chosen here is  $\hat{R} = 0.45$ , representative of the CCFA-relevant range  $\hat{R} \in [0.3, 0.6]$ .

We observe that the analytical profile matches the numerical shape with high accuracy, and as expected, the error between the two increases with the magnitude of displacement from the undeformed state. Consistent with the trends seen in the force response, the error during dilation at  $\varepsilon$  is greater than that during compression at  $-\varepsilon$ . Moreover, since the displacement increment between adjacent equilibrium profiles is fixed at  $|\Delta\varepsilon| = 0.17$ , the corresponding variation in force required to transition between these states supports our earlier conclusion: the incremental force required to move between neighbouring equilibrium states grows as the droplet is compressed away from the zero-force state, and diminishes as it is dilated.

Following our discussion above, we conclude this section by analyzing the performance of the asymptotic expansion for the bridge profile across different capillary radii under two distinct conditions: at fixed force and at fixed displacement, for both compression and dilation by the same amount from the undeformed state. Fig. 2.9 shows that at fixed force (with a representative value  $\hat{F} = \pm 0.10$ ), the asymptotic profile closely matches the numerically computed shape, with accuracy improving as the capillary radius increases. This behaviour is consistent with our earlier established trend that the displacement required to generate a given force response decreases with increasing capillary radius; smaller displacements from the undeformed state lead to smaller deviations from the true profile.

Finally, Fig. 2.10 shows that at fixed displacement (here, a representative value  $\varepsilon = \pm 0.20$  is chosen), the discrepancy between the analytical and numerical profiles follows a non-monotonic trend similar to that observed in the pinning angle error shown in Fig. 2.7(b). This connection is expected, as the asymptotic expansion for the pinning angle  $\theta$  determines the bounds of the tilt angle domain,  $\phi \in [\pi/2 - \theta, \theta - \pi/2]$ , used to compute the analytical bridge shape. Additionally, the force response associated with each of the profiles in this fixed-displacement setting recovers the previously established trend: the force required to displace the droplet by a fixed amount  $|\varepsilon|$  increases with capillary radius and is consistently larger in magnitude during compression than during dilation.

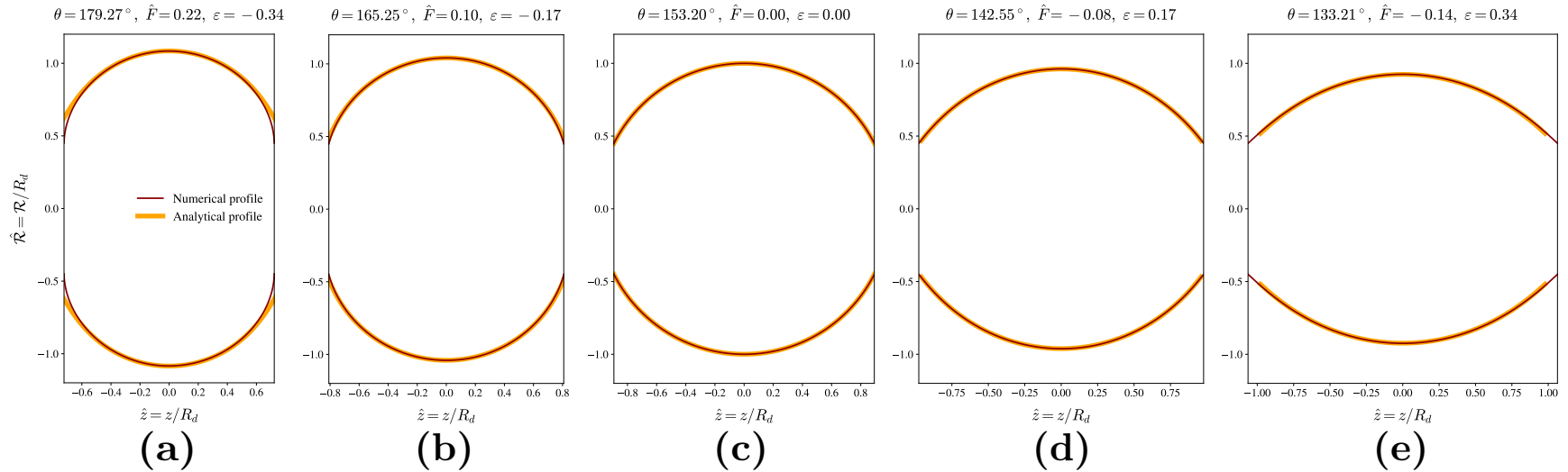


**Figure 2.8:** Comparison of bridge profiles  $\hat{\mathcal{R}}(\hat{z})$  from the numerical solution (*red solid*) and the second-order asymptotic expansion (*thick orange solid*) as the droplet evolves from the undeformed state [panel (c)] to maximum compression ( $\theta = 180^\circ$ ) [panel (a)] and to an equally dilated state [panel (e)]. The capillary radius selected is  $\hat{R} = 0.45$ , representative of the CCFA-relevant range  $\hat{R} \in [0.3, 0.6]$ . The absolute displacement between adjacent equilibrium states is fixed at  $|\Delta\varepsilon| = 0.17$ . For each panel, the corresponding pinning angle  $\theta$ , force response  $\hat{F}$ , and displacement  $\varepsilon$  are listed at the top of each panel for reference.

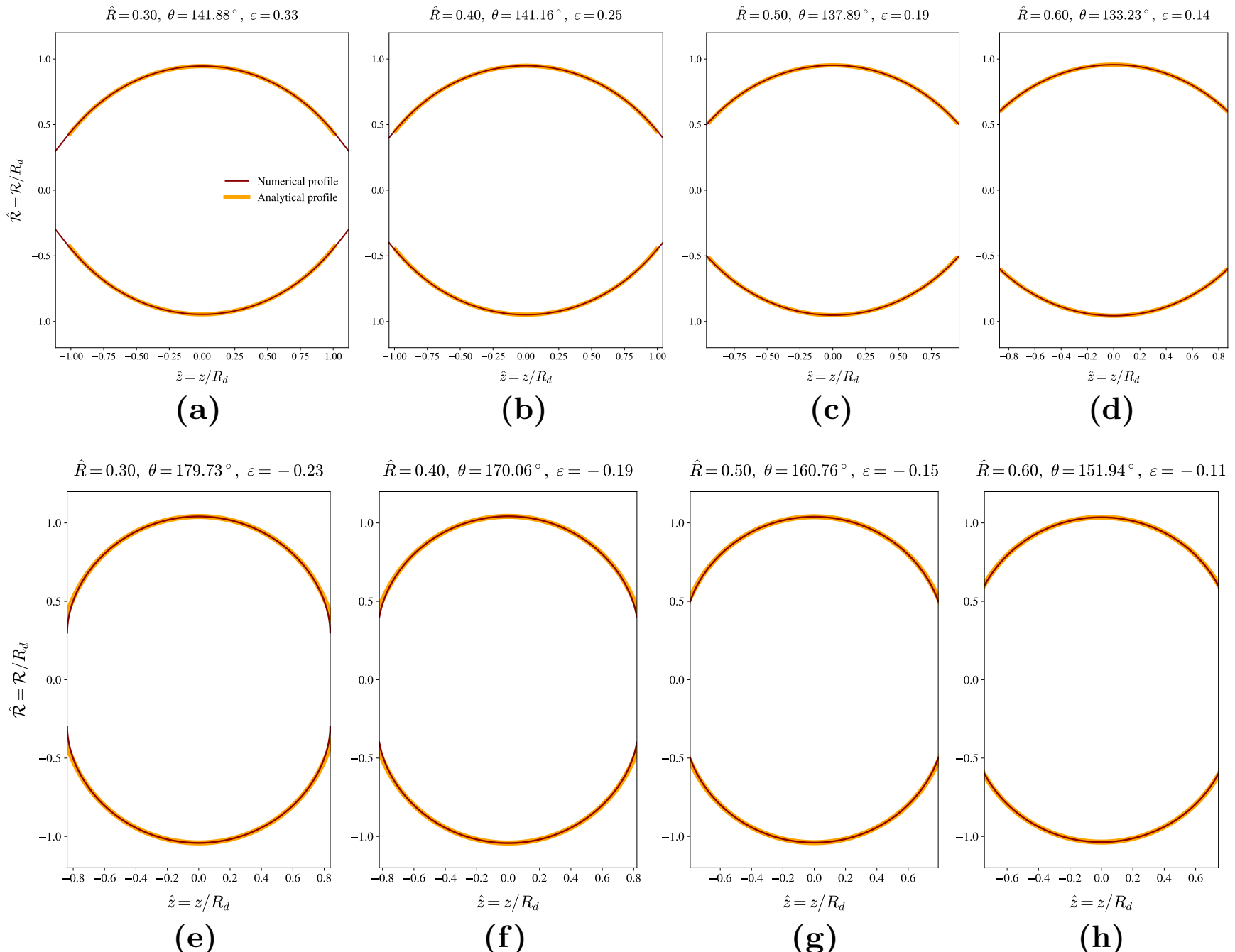


**Figure 2.9:** Comparison of numerical (red solid) and analytical (thick orange solid) bridge profiles for capillary radii  $\hat{R} \in \{0.3, 0.4, 0.5, 0.6\}$  at fixed force magnitude:  $\hat{F} = -0.10$  during dilation [panels (a) to (d)] and  $\hat{F} = 0.10$  during compression [panels (e) to (h)]. The capillary radius  $\hat{R}$ , pinning angle  $\theta$ , and displacement  $\varepsilon$  are indicated at the top of each panel for reference.

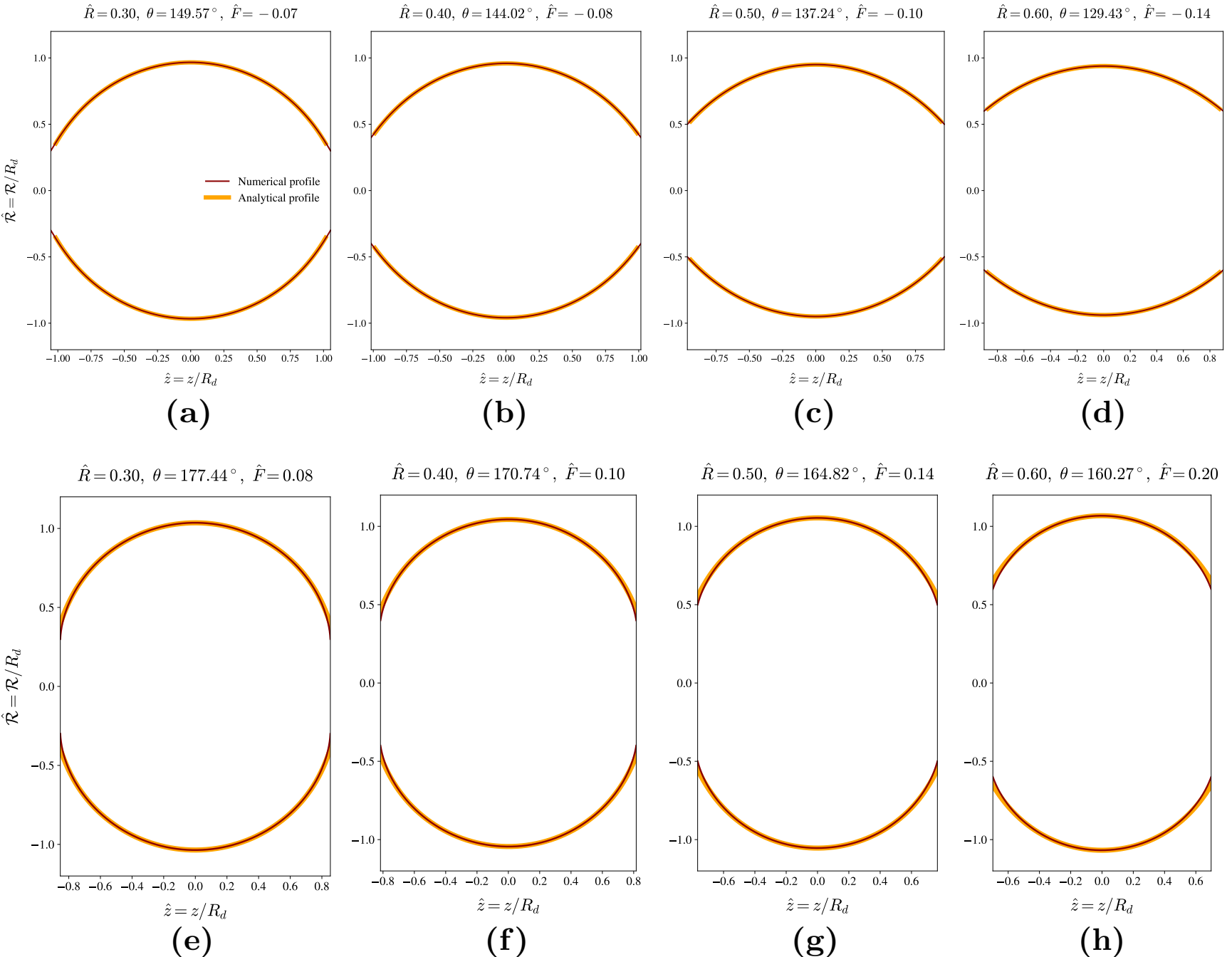


**Figure 2.10:** Comparison of numerical (red solid) and analytical (thick orange solid) bridge profiles for capillary radii  $\hat{R} \in \{0.3, 0.4, 0.5, 0.6\}$  at fixed absolute displacement from the undeformed state:  $\varepsilon = 0.20$  during dilation [panels (a) to (d)] and  $\varepsilon = -0.20$  during compression [panels (e) to (h)]. The capillary radius  $\hat{R}$ , pinning angle  $\theta$ , and force response  $\hat{F}$  are indicated at the top of each panel for reference.

### 2.4.4 Limitations

The asymptotic expressions developed here are restricted to small-strain displacements ( $|\Delta L/L_0| \ll 1$  or  $|\Delta L/R_d| \ll 1$ ) of the capillaries and assume that the droplet remains axisymmetric throughout its quasi-static deformation. As such, the model inevitably loses accuracy under relatively large displacements or once axisymmetry breaks beyond a critical deformation, as analyzed by Elfring and Lauga [127]. Furthermore, to isolate the essential physics, the present formulation considers only capillaries of equal radius. Geometric asymmetry due to unequal capillary radii has been examined at linear order by Kusumaatmaja and Lipowsky [2], and an attempt to extend this to quadratic order was made by Sariola [3]. However, as they observed, such asymmetries do not qualitatively alter the underlying dominant physical trends.

A further key fact that the present analytical framework relies on is that the relative change in droplet bridge volume remains below 5%—both for pinned droplets and for those held at the capillary rims by constant suction pressure—across the range of capillary radii and suction pressures typically used in the CCFA (see Appendix B). Accordingly, the bridge volume is approximated as constant. When larger capillary radii or higher suction pressures are employed, however, this approximation progressively breaks down due to enhanced volume exchange between the bridge and the spherical caps confined within the capillaries. In such cases, the correct constraint to enforce—provided no mass is exchanged with the ambient fluid—is conservation of the total droplet volume, comprising both the bridge and cap volumes. Consequently, the first- and second-order coefficients of the force response, mean curvature, pinning angle, and bridge shape will differ from those reported in this chapter, although the underlying methodology for their derivation remains unchanged (as briefly discussed at the end of Section 2.1).

## 2.5 Conclusions

### 2.5.1 Key findings

In this chapter, we derived analytical expressions to approximate the force response and shape of an axisymmetric Newtonian droplet (or bubble) pinned at the rims of two coaxial capillaries of equal radii, forming a capillary bridge that is quasi-statically compressed or dilated from its undeformed spherical shape under small imposed strains. At each deformation, the system is allowed to attain mechanical equilibrium, so that the flow field and the associated bulk viscous stresses in both the droplet and the surrounding Newtonian fluid dissipate, leaving the force response governed solely by the static Laplace pressure and contact line tension. This framework provides a direct analytical description of quasi-static deformation experiments performed with the CCFA.

This work constitutes the first analytical model to extend significantly beyond the linear force-displacement regime studied by Kusumaatmaja and Lipowsky [2]—developed primarily to extract the interfacial tension  $\gamma$ —and the weak Taylor-expansion-based quadratic correction proposed by Sariola [3]. The present model captures the correct leading-order nonlinear behaviour of the force response, mean curvature, pinning angle, and, consequently, the droplet shape. For capillary radii  $R$  typically used in the CCFA—falling in the range  $0.3 \leq R/R_d \leq 0.6$ , where  $R_d$  is the undeformed droplet radius—the displacement  $\Delta L$  at which our analytical model incurs a 2% relative error in the force response (compared against numerical shooting solutions of the full Young–Laplace boundary value problem) during dilation ranges from approximately  $0.7R_d$  at  $R/R_d = 0.3$  to  $0.3R_d$  at  $R/R_d = 0.6$ . Under maximum compression, the relative error remains within  $\approx 1\%$  across this entire range of capillary radii. By contrast, the models of Kusumaatmaja and Lipowsky [2] and Sariola [3] attain comparable accuracy only within displacements  $|\Delta L| \lesssim 0.05R_d$ .

The present model is constructed using regular perturbation expansions up to second order in the small dimensionless displacement  $\Delta L/R_d$  about the undeformed state, for the force response, mean curvature, and pinning angle of the droplet. Each correction is obtained through shape-mediated capillary rim boundary conditions and a bridge volume conservation constraint. Corrections at each order depend on those at lower orders and are thus ultimately a function of the undeformed pinning angle  $\theta_0$ .

Thus, by specifying  $\theta_0$  (or equivalently, the capillary-to-droplet radius ratio  $R/R_d = \sin \theta_0$ ), one can compute the evolving force response, mean curvature, pinning angle, and droplet shape at any displacement well into the leading-order nonlinear regime—without solving the full Young–Laplace equation numerically at each prescribed displacement. While such numerical approaches are tractable, they remain cumbersome for routine validation and analysis of CCFA experiments. This analytical framework thus provides a practical and efficient tool for experimentalists seeking to interpret quasi-static droplet (or bubble) deformation data in the CCFA, and more generally, for analyzing any pinned axisymmetric Newtonian capillary bridge undergoing quasi-static deformation in natural or industrial contexts.

In these asymptotic expansions, the first-order corrections predominantly set the magnitude of each quantity and may therefore be interpreted as a “magnitude mode.” The second-order coefficients govern the asymmetry between compression and dilation, introducing nonlinear effects, and may thus be viewed as a “deformation-type mode.” Together, these corrections capture the key physical trend that the incremental force required to displace a droplet between successive equilibrium states increases under compression and decreases under dilation, with this incremental force at each displacement step growing with capillary radius. Put differently, compressing a droplet from its undeformed state is energetically most costly when using a large capillary, with the incremental energy cost rising at each successive compression step; conversely, dilation is energetically least costly with a small capillary, with the incremental cost diminishing as dilation progresses. Finally, the accuracy of the asymptotic expansions varies with capillary radius: while the errors in the force response and mean curvature increase monotonically with  $R$ , the error in the pinning angle exhibits a non-monotonic trend, initially decreasing with  $R$  up to  $R \approx 0.38R_d$ , and increasing thereafter.

### 2.5.2 Future directions

A natural extension of the present model, which we aim to explore in future work, is to investigate how the evolution of the force response and droplet (or bubble) shape is modified when the droplet–ambient fluid interface is laden with surfactants and subjected to quasi-static deformation. In such systems, the equilibrium interfacial tension  $\gamma$  depends on the equilibrium surfactant surface concentration  $\Gamma$ , and thus varies as the droplet is displaced from its zero-force state. Accordingly, both  $\gamma$  and  $\Gamma$  must be expressed as regular perturbation expansions in  $\Delta L/R_d$  about their zero-force values, thereby perturbing the isotherm that relates them [15]. This perturbed isotherm must then be incorporated into the Young–Laplace equation, as well as into the boundary conditions and volume constraint that close the system. This direction is of significant practical interest, since fluid–fluid interfaces in most natural and industrial settings are often surfactant-laden [15, 72], and surfactants can substantially alter both the droplet shape and the resulting force response at a given capillary separation.

# Chapter 3

## A theory for characterizing the bulk rheology and interfacial tension of viscoelastic microdroplets under oscillatory deformation

### 3.1 Introduction

Viscoelastic microdroplets are micron-sized fluid volumes of characteristic size 10–1000  $\mu\text{m}$  that, under an external mechanical load, exhibit both viscous (fluid-like) and elastic (solid-like) bulk responses [31, 32, 34], together with an interfacial elastic recoil that resists changes in surface area [15–17]. Their bulk rheology is characterized by a constant zero-shear viscosity  $\mu_0$ , which quantifies the resistance of the droplet to flow under slow, steady shears (long timescales), and a constant infinite-frequency elastic modulus  $G_0$ , which captures the limiting stiffness of the droplet when deformed on short timescales (high frequencies). The crossover from predominantly elastic to predominantly viscous behaviour is governed by the relaxation time  $\lambda$ , a material property that sets the balance between elastic energy storage and viscous dissipation. At the interface, when clean (surfactant-free), the restoring force is provided by a constant interfacial tension  $\gamma$ . This duality—bulk viscoelasticity coupled with interfacial capillarity—renders the deformation dynamics of viscoelastic microdroplets under diverse loading protocols particularly rich, motivating a growing body of work in recent years [87, 128, 129].

Beyond their rich single-droplet dynamics, viscoelastic microdroplets are compelling because they are pervasive across biological and industrial settings. In biology, cell-sized droplets of phase-separated biopolymers, protein condensates, and lipid-rich organelles exhibit viscoelasticity that regulates intracellular organization and transport [7, 130, 131]. In the food and cosmetics industries, emulsions containing polymeric or gel-like dispersed phases rely on constituent microdroplet viscoelasticity to tune macroscopic texture, stability, and mouthfeel [9, 10, 132].

In medicine, microdroplets serve as model building blocks for microgel- and capsule-based drug carriers, whose ability to deform through constrictions while resisting coalescence or rupture is critical for targeted delivery [94, 133, 134]. More broadly, they represent one of the simplest classes within the huge spectrum of soft microparticles, where the bulk rheology, stability, and failure of the composite soft material are dictated by mechanics at the single-microdroplet scale. This microscopic-to-macroscopic connection underscores the importance of characterizing their material properties under controlled loading.

Despite the ubiquity of viscoelastic microdroplets and the pressing need to characterize their material properties, the available literature remains scarce, primarily due to the absence of experimental apparatus capable of probing such droplets at the microscale. Historically, one of the most widely used devices for characterizing the bulk rheology of macroscopic viscoelastic droplets (or thin films) of size  $\sim 1\text{--}10\text{ mm}$  has been the oscillatory squeeze flow rheometer (OSFR). This device was first proposed theoretically by Phan-Thien [55] in 1980 and later fully realized experimentally by Bell et al. [37]. The OSFR builds on the classical squeeze-flow technique, introduced by Stefan [135] in the late nineteenth century to determine the viscosity of Newtonian thin films from force–displacement measurements. As such, its design underpins the squeeze flow rheometer (SFR), which remains widely used for probing the bulk rheology of both Newtonian and non-Newtonian fluids [31, 51, 52, 59, 60, 136–144].

In both the SFR and OSFR, a small volume of fluid (typically 10–100 mL) is confined between two coaxial, millimeter-sized circular substrates (or plates) of radius  $R$ . The fluid is pinned at the rims of the substrates, and the upper substrate is adjusted such that the fluid maintains a pinning angle of  $\pi/2$  at both rims, with a thin gap  $H_0$  established between them, corresponding to a small aspect ratio  $\delta = H_0/R \ll 1$ . In this initial configuration, the fluid sample forms a cylindrical thin film. In the SFR, the upper substrate is then driven either at constant velocity or under a constant applied force, such that nonlinearities in the resulting flow field remain negligible at leading order, yielding a lubrication flow [29].

The resulting force exerted by the film on the lower substrate, referred to as the *force response*, is then measured as a function of time. This response is dominated by bulk rheological contributions, while interfacial effects are negligible. The latter arises because, in general, the capillary stresses are small compared with bulk viscous and elastic stresses at the macroscopic scale, leading to large elasto-capillary and capillary numbers,  $Ec_0 = G_0 R / \gamma \gg 1$  and  $Ca_0 = \mu_0 R \omega / \gamma \gg 1$ , respectively.

For Newtonian fluids, the force response in the SFR is directly proportional to the dynamic viscosity, thereby providing a straightforward measurement of this property [13, 135]. For viscoelastic fluids, under negligible inertia, the leading-order deviatoric stress is commonly described by the Maxwell linear viscoelastic model [31, 32, 34, 36]. In this case, the SFR force response can be expressed as a Volterra integral of the relaxation modulus  $G(\tau)$ , which encodes the memory of the fluid to past deformations. In general, this integral does not reduce to a simple algebraic relation in terms of the bulk rheological parameters,  $\mu_0$  and  $G_0$ , or equivalently  $\lambda = \mu_0/G_0$  [136, 138, 139, 143–145]. Consequently, extracting these rheological properties is far less straightforward than for Newtonian fluids.

In practice, this is why the OSFR is preferred for bulk rheological characterization of viscoelastic fluids. Instead of driving the upper substrate at constant velocity or under constant force, it is oscillated with a small strain amplitude about its mean (initial) position, ensuring that nonlinearities in the flow field are negligible at leading order. Once initial transients have decayed, the flow field is assumed to oscillate harmonically at the driving frequency  $\omega$ .

This assumption allows the Volterra integral of  $G(\tau)$  to be recast directly in terms of the linear, frequency-dependent rheological properties of the fluid, or equivalently the complex viscosity  $\eta^*(\omega)$ , following the correspondence principle of Pipkin [146]. These properties are expressed as the storage modulus  $G'(\omega)$ , representing the in-phase (to the imposed strain) elastic component of the response that quantifies energy stored per oscillation cycle, and the loss modulus  $G''(\omega)$ , representing the out-of-phase viscous component associated with energy dissipation [34, 58]. Both moduli are directly related to the intrinsic rheological parameters  $\mu_0$ ,  $G_0$ , and  $\lambda$ , and thus enable their characterization by measuring these moduli at a given frequency or, more commonly, across an entire frequency sweep.

However, the OSFR is designed for macroscopic droplets and cannot resolve the sensitive force

responses of microdroplets, which typically fall in the range  $1\text{ nN}\text{--}1\text{ mN}$ . As a result, the OSFR has been primarily employed to characterize the bulk rheology of macroscopic droplets or thin films [37, 55–60]. As noted earlier, these measurements are generally performed in the high elasto-capillary number ( $\text{Ec}_0 \gg 1$  or  $\text{Ec} = G'R/\gamma \gg 1$ ) and high capillary number ( $\text{Ca}_0 \gg 1$  or  $\text{Ca} = G''R/\gamma \gg 1$ ) regimes, where interfacial stresses are negligible compared with bulk rheological stresses.

Other instruments, such as the compressional rheometer [39, 40], the micro-Fourier rheometer (MFR) [45, 147], and the filament stretching rheometer (FiSER) [13, 46, 148], which can all be operated on principles similar to the OSFR, have also traditionally been applied in this regime. The first study to investigate the operation of the OSFR in the low-to- $\mathcal{O}(1)$  capillary number regime ( $\bar{\text{Ca}} = \mu R\omega/\gamma \lesssim 1$ ) was conducted by Barakat et al. [13]. Although their work considered macroscopic Newtonian droplets, significant effects from capillary stresses emerged because they assumed either sufficiently small droplet viscosity or sufficiently low oscillation frequency to render  $\bar{\text{Ca}} \lesssim 1$ . This enabled them to directly extract both the dynamic viscosity  $\mu$  and the interfacial tension  $\gamma$  from the measured force response.

The dynamics captured by Barakat et al. [13] for macroscopic Newtonian droplets with low viscosity or driven at low frequency are equally representative of Newtonian microdroplets, since both cases lie in the  $\bar{\text{Ca}} \lesssim 1$  regime. In this chapter, we extend this analytical framework to viscoelastic microdroplets whose linear viscoelastic behaviour at low strain amplitudes is described by the (single-mode) Maxwell model, thereby addressing the current scarcity of analytical approaches that simultaneously probe their bulk rheology—i.e.,  $G'(\omega)$  and  $G''(\omega)$ , and hence  $\mu_0$ ,  $G_0$ , and  $\lambda$ —together with their interfacial tension  $\gamma$ . More broadly, the framework applies to any viscoelastic droplet (or thin film) subjected to oscillatory deformation in the OSFR configuration where interfacial stresses remain significant, i.e., in the  $\text{Ec} \lesssim 1$  and  $\text{Ca} \lesssim 1$  regime. However, since the OSFR cannot directly perturb microdroplets, experimental validation of this theory requires an apparatus that not only operates on OSFR principles but is also capable of probing microdroplets, ensuring that the framework models a realistic physical setting.

Inspired by the micro-cantilever tensiometer [20] and the atomic force microscope (AFM) [21, 85, 86], the cantilevered capillary force apparatus (CCFA) developed by Frostad et al. [1] provides such a solution. At present, it is the only practical instrument capable of attaching a wide range of soft microparticles to its capillaries via capillary-rim pinning or suction and of perturbing them while measuring their small force responses with high accuracy. Alternative techniques, such as the biomembrane force probe [19, 75], AFM, the surface force apparatus (SFA) [76, 77], and optical or magnetic tweezers [78, 79], could in principle be employed; however, these methods are generally limited to particle sizes  $\lesssim 10\text{ }\mu\text{m}$ , and are therefore unsuitable for most microdroplet sizes of interest here, or they face difficulties in attaching highly deformable microparticles in order to perturb them. We note that while the CCFA has previously been used to impose oscillatory deformations on microdroplets and to measure the resulting force response exerted on the cantilevered capillary [1], it has not yet been implemented in the thin-gap, initially cylindrical configuration characteristic of the OSFR. Nevertheless, such an adaptation is, in principle, feasible.

In this analytical framework, we model the flow field within the droplet using a regular perturbation expansion in the small strain amplitude ( $\varepsilon \ll 1$ ) and small aspect ratio ( $\delta^2 \ll 1$ ), with the droplet bulk behaviour described by the Maxwell model for the leading-order deviatoric stress. The thin-gap geometry, small-amplitude oscillations, and an initially cylindrical shape ensure that interface slopes remain small, so that the leading-order post-transient velocity field within the droplet is governed entirely by the oscillatory motion of the upper substrate. The resulting force response consists of a static component—arising from Laplace pressure and contact-line tension—together with a dynamic component composed of linear in-phase contributions from interfacial curvature and bulk elasticity, and an out-of-phase contribution from bulk viscosity.

Here, the dynamic component arises through the lubrication pressure. From this response, we show that the interfacial tension  $\gamma$  can be extracted from the static contribution, which can then be used to determine the frequency-dependent storage and loss moduli,  $G'(\omega)$  and  $G''(\omega)$ , from the dynamic component. In turn, the intrinsic bulk material parameters—the zero-shear viscosity  $\mu_0$ , infinite-frequency modulus  $G_0$ , and relaxation time  $\lambda = \mu_0/G_0$ —can be inferred. This framework thus provides the first simple yet robust analytical method for simultaneously determining both the bulk rheology and interfacial tension of a viscoelastic microdroplet solely from its oscillatory force response in the OSFR configuration.

Following this section, the chapter is organized as follows. In Section 3.2, we describe the setup of the viscoelastic microdroplet in the OSFR or CCFA in the low Bond number ( $Bo \ll 1$ ) limit, where the orientation of the substrates or capillaries is immaterial. We then state the mass and momentum conservation equations for the droplet and the surrounding Newtonian fluid, along with the Maxwell constitutive model employed to describe the droplet’s bulk behaviour under small-amplitude oscillatory deformation. The required initial and boundary conditions are specified, including the interfacial stress balance and the kinematic boundary condition.

In Section 3.3, we nondimensionalize the system using appropriate characteristic scales and posit regular perturbation expansions: in  $\delta^2 \ll 1$  and  $\varepsilon \ll 1$  for the droplet flow field, and in  $\varepsilon$  for the ambient flow field and droplet shape. These expansions yield, at leading (dynamic) order, the governing lubrication equations for the droplet and Stokes equations for the ambient fluid, with inertia neglected owing to the low Reynolds number at the microscale. The same expansions are also applied to obtain the leading-order corrections to the interfacial stress balance, kinematic boundary condition, and droplet shape. The implications of different limits of the capillary number  $Ca_0 = \mu_0 R \omega / \gamma$  on the interfacial stress balance are also discussed in detail.

In the post-transient regime, when the flow field oscillates harmonically at the driving frequency  $\omega$ , the velocity and dynamic pressure fields are expressed as complex-valued functions with frequency  $\omega$ , following the correspondence principle [146], and the oscillatory force response is obtained. In Section 3.4, we validate our framework against previous analytical models by considering appropriate limits of the elasto-capillary number  $Ec = G' R / \gamma$  and capillary number  $Ca = G'' R / \gamma$ , and then establish a procedure to decouple the interfacial tension, storage modulus, and loss modulus from the force response measured as a function of time in the OSFR or CCFA. We close this section by outlining the limitations of the present analytical framework—arising from its modeling assumptions—together with their implications and, where appropriate, potential remedies; we also emphasize the need for validation via numerical simulations and/or experiments. Finally, in Section 3.5, we summarize the key findings and briefly discuss potential extensions to viscoelastic solid microparticles, microparticles with more complex bulk rheology (e.g. microgels), and surfactant-laden viscoelastic microdroplets.

## 3.2 Problem setup

We consider a static viscoelastic microdroplet pinned at the rims of two coaxial circular substrates of radius  $R = 10\text{--}100\,\mu\text{m}$  separated by a thin gap  $H_0$  such that the aspect ratio  $\delta = H_0/R \sim 10^{-1} \ll 1$ . The substrate radii are typical of the CCFA [1], while the aspect ratio is characteristic of the OSFR [13, 58] and related rheometers capable of oscillatory perturbations, such as the compressional rheometer [39, 40], MFR [45], and FiSER [46]. The droplet is characterized by a constant density  $\rho$ , zero-shear viscosity  $\mu_0$ , infinite-frequency elastic modulus  $G_0$ , and relaxation time  $\lambda$ .

This setup is surrounded by a Newtonian fluid of constant density  $\rho_a$  and dynamic viscosity  $\mu_a$ , and the constant interfacial tension at the droplet–ambient interface is  $\gamma$ . The shape of the interface

is assumed axisymmetric about the vertical axis joining the centers of the substrates. The pinning angle at the lower substrate is  $\theta_0 = \pi/2$ . The ratio of gravitational to interfacial curvature stresses is given by the Bond number  $Bo = \Delta\rho g H_0^2 / \gamma = \delta^2 \Delta\rho g R^2 / \gamma \sim 10^{-7} - 10^{-5} \ll 1$ , where  $\Delta\rho = \rho - \rho_a$  is the density difference and  $g$  is the gravitational acceleration, indicating that gravitational effects are negligible. Consequently, the upper pinning angle is also  $\theta_0 = \pi/2$ , and the droplet adopts a static cylindrical shape.

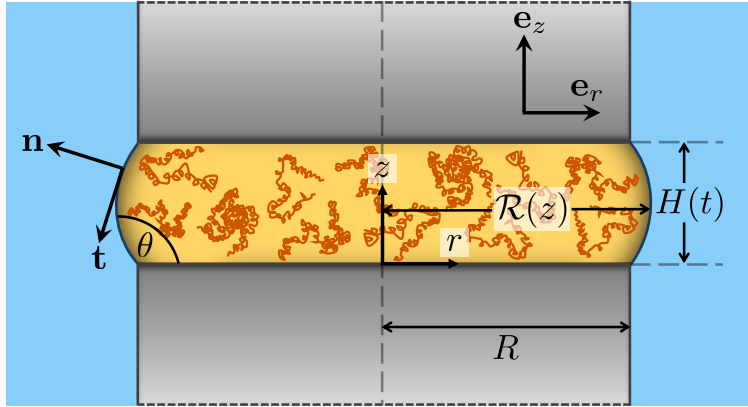


**Figure 3.1:** Schematic of an axisymmetric viscoelastic microdroplet pinned between two coaxial circular substrates of radius  $R = 10 - 100 \mu\text{m}$  and subjected to oscillatory deformation. The upper substrate oscillates while the lower remains fixed. The instantaneous gap at time  $t \geq 0$  is  $H(t)$ , with  $H(0) = H_0$  and aspect ratio  $\delta = H_0/R \ll 1$ . An axisymmetric cylindrical coordinate system  $(r, z)$  is adopted, with corresponding unit vectors denoted by  $\mathbf{e}_r$  and  $\mathbf{e}_z$ . The interface shape is described by  $r = \mathcal{R}(z, t)$ , with  $\mathcal{R}(z, 0) = R$ . The pinning angle is denoted by  $\theta(t)$ , with  $\theta(0) = \pi/2$ . The unit normal and tangent to the interface are represented by  $\mathbf{n}$  and  $\mathbf{t}$ , respectively.

From this initial configuration, we impose a sinusoidal oscillation of the upper substrate with angular frequency  $\omega$  and small strain amplitude  $\varepsilon \ll 1$ , while keeping the lower substrate fixed. We assume that the droplet–ambient fluid interface remains axisymmetric throughout the oscillation and hence adopt the axisymmetric cylindrical coordinate system  $(r, z)$ , with the origin located at the center of the lower substrate. Here,  $r$  and  $z$  denote the radial (tangential to the substrates) and axial (normal to the substrates) directions, respectively, and the corresponding unit vectors are denoted by  $\mathbf{e}_r$  and  $\mathbf{e}_z$  (see Fig. 3.1). The instantaneous gap between the substrates at time  $t \geq 0$  is then given by

$$H(t) \mathbf{e}_z = H_0 [1 + \varepsilon \sin(\omega t)] \mathbf{e}_z, \quad (3.1)$$

and the shape of the interface is described by the function  $r = \mathcal{R}(z, t)$ , with  $\mathcal{R}(z, 0) = \mathcal{R}_0(z) = R$ .

Owing to the small Bond number  $Bo \ll 1$ , gravitational effects remain negligible during the oscillation, and the interface shape retains symmetry about the mid-plane  $z = H(t)/2$ . As such, it can be characterized by a single time-dependent pinning angle  $\theta(t)$ , with  $\theta(0) = \theta_0 = \pi/2$ . The unit normal and tangent vectors to the interface are denoted by  $\mathbf{n}$  and  $\mathbf{t}$ , respectively.

The dynamics of the viscoelastic microdroplet are governed by the conservation of mass and momentum, expressed as

$$\nabla \cdot \mathbf{u} = 0, \quad (3.2a)$$

$$\rho \left( \frac{\partial \mathbf{u}}{\partial t} + \mathbf{u} \cdot \nabla \mathbf{u} \right) = -\nabla p + \rho \mathbf{g} + \nabla \cdot \boldsymbol{\tau}, \quad (3.2b)$$

where  $\mathbf{u}(\mathbf{x}, t)$  and  $p(\mathbf{x}, t)$  denote the velocity and pressure fields of the droplet, and  $\boldsymbol{\tau}(\mathbf{x}, t)$  is the corresponding deviatoric stress tensor. The ambient Newtonian fluid satisfies the same set of equations with the subscript ‘ $a$ ’ appended to each variable. The deviatoric stress in the ambient fluid is given by Newton’s law of viscosity,  $\boldsymbol{\tau}_a = 2\mu_a \mathbf{E}_a$ , where  $\mathbf{E}_a = \frac{1}{2} [\nabla \mathbf{u}_a + (\nabla \mathbf{u}_a)^\top]$  is the rate-of-strain tensor.

At leading order in the small strain amplitude  $\varepsilon$ , the deviatoric stress in the droplet is assumed to follow the classical Maxwell linear viscoelastic model [31, 34], which corresponds to a spring and dashpot connected in series, and is given by

$$\boldsymbol{\tau} + \lambda \frac{\partial \boldsymbol{\tau}}{\partial t} = 2\mu_0 \mathbf{E},$$

where  $\lambda = \mu_0/G_0$  is the relaxation time and  $\mathbf{E} = \frac{1}{2} [\nabla \mathbf{u} + (\nabla \mathbf{u})^\top]$  is the rate-of-strain tensor of the droplet. In the limit where the characteristic timescale of deformation  $t_c$  is much longer than the relaxation time  $\lambda$ , i.e., the Deborah number  $\text{De} = \lambda/t_c \ll 1$ , the model reduces to Newton’s law of viscosity,  $\boldsymbol{\tau} = 2\mu_0 \mathbf{E}$ , and the droplet behaves as a Newtonian fluid. Conversely, when  $t_c \ll \lambda$  or  $\text{De} \gg 1$ , it reduces to Hooke’s law of elasticity,  $\partial \boldsymbol{\tau} / \partial t = 2G_0 \mathbf{E}$ , corresponding to a Hookean solid.

The regime of primary interest in this work is the intermediate case where  $t_c \sim \lambda$ , i.e.,  $\text{De} \sim 1$ , which exhibits true viscoelastic behaviour with comparable fluid-like and solid-like responses. Integrating the above differential form of the Maxwell model in time from  $t = -\infty$  to  $t$ , and assuming that the deviatoric stress  $\boldsymbol{\tau}$  remains bounded as  $t \rightarrow -\infty$ , yields the equivalent integral form:

$$\boldsymbol{\tau}(\mathbf{x}, t) = 2 \int_0^\infty [G(\tau) \mathbf{E}(\mathbf{x}, t - \tau)] d\tau, \quad (3.3)$$

where  $G(\tau) = G_0 \exp(-\tau/\lambda)$  for  $\tau \geq 0$  is the relaxation modulus, representing the memory of past deformations.

The governing equations for the droplet in Eqn. (3.2) are subject to no-slip boundary conditions at both the upper and lower substrates. At the droplet–ambient fluid interface, the stress jump is balanced by curvature-induced capillary stresses, expressed by the interfacial stress balance [16, 17, 149]:

$$\mathbf{n} \cdot (\boldsymbol{\sigma}_a - \boldsymbol{\sigma}) = \gamma \mathbf{n} (\nabla \cdot \mathbf{n}). \quad (3.4)$$

Here,  $\mathbf{n}$  is the local unit normal pointing from the droplet into the ambient fluid (see Fig. 3.1), and  $\boldsymbol{\sigma}_a = -p_a \mathbf{I} + \boldsymbol{\tau}_a$  and  $\boldsymbol{\sigma} = -p \mathbf{I} + \boldsymbol{\tau}$  are the stress tensors of the ambient fluid and droplet, respectively, with  $\mathbf{I}$  being the identity tensor.

The term  $\nabla \cdot \mathbf{n}$  represents twice the local mean curvature of the interface  $\mathcal{H}$ , which in the axisymmetric setting is given by

$$2\mathcal{H} = \nabla \cdot \mathbf{n} = \frac{1}{\mathcal{R} (1 + \mathcal{R}'^2)^{1/2}} - \frac{\mathcal{R}''}{(1 + \mathcal{R}'^2)^{3/2}}, \quad (3.5)$$

where  $\mathcal{R}' = \partial \mathcal{R} / \partial z$  and  $\mathcal{R}'' = \partial^2 \mathcal{R} / \partial z^2$  [16, 17, 103]. The first term on the right-hand side corresponds to the azimuthal (circumferential or hoop) curvature, which quantifies the change in the interface normal  $\mathbf{n}$  as one traverses a ring of constant axial coordinate  $z$ , while the second term represents the meridional (axial) curvature, associated with variations of the interface normal along the meridional arc.

In addition to the interfacial stress balance (3.5), the velocity fields of the droplet and the ambient fluid must match at the interface, and the kinematic boundary condition must be satisfied [29]:

$$\mathbf{u} \cdot \mathbf{n} = \frac{1}{(1 + \mathcal{R}'^2)^{1/2}} \frac{\partial \mathcal{R}}{\partial t} = \mathbf{u}_a \cdot \mathbf{n}. \quad (3.6)$$

Finally, we assume that the ambient velocity field decays sufficiently far from the interface, i.e.,  $\mathbf{u}_a \rightarrow \mathbf{0}$  as  $r \rightarrow \infty$ .

### 3.3 Analytical framework

#### 3.3.1 Non-dimensionalization

For the microdroplet, we adopt  $H_0$  as the characteristic length scale in the axial direction  $\mathbf{e}_z$  and  $R$  as that in the radial direction  $\mathbf{e}_r$  as  $R$ , while for the ambient fluid,  $R$  serves as the characteristic length scale in both directions. Consequently, for the microdroplet, the gradient operator  $\nabla$  admits two possible scales,  $1/H_0$  and  $1/R$ , of which  $1/H_0$  dominates owing to  $H_0 = \delta R$  ( $\delta \ll 1$ ) and is thus chosen as the appropriate scale.

For the ambient fluid,  $1/R$  is the only relevant scale for the gradient operator. From Eqn. (3.1), the axial velocity component of the droplet scales as,  $u_z = \mathbf{e}_z \cdot \mathbf{u} \sim \varepsilon H_0 \omega$ , and the mass conservation (3.2a) then requires the radial component to scale as  $u_r = \mathbf{e}_r \cdot \mathbf{u} \sim \varepsilon R \omega$ , yielding the overall velocity scale  $\mathbf{u} \sim \varepsilon R \omega$ . Since the ambient fluid spans a characteristic length  $R$ , the velocity scale  $\mathbf{u}_a \sim \varepsilon R \omega$ . The timescale of the problem is set by the inverse angular frequency  $\omega^{-1}$ .

The above choice of characteristic scales implies that the deviatoric stresses scale as  $\boldsymbol{\tau} \sim \varepsilon \mu_0 R \omega / H_0 = \varepsilon \mu_0 \omega / \delta$  for the droplet and  $\boldsymbol{\tau}_a \sim \varepsilon \mu_a \omega$  for the ambient fluid. Consequently, their divergences scale as  $\nabla \cdot \boldsymbol{\tau} \sim \varepsilon \mu_0 \omega / (\delta^2 R)$  and  $\nabla \cdot \boldsymbol{\tau}_a \sim \varepsilon \mu_a \omega / R$ , respectively. The unsteady inertial terms scale as  $\partial \mathbf{u} / \partial t \sim \varepsilon R \omega^2$  and  $\partial \mathbf{u}_a / \partial t \sim \varepsilon R \omega^2$ , while the convective accelerations scale as  $\mathbf{u} \cdot \nabla \mathbf{u} \sim \varepsilon^2 R \omega^2$  and  $\mathbf{u}_a \cdot \nabla \mathbf{u}_a \sim \varepsilon^2 R \omega^2$ .

The pressure gradients scale as  $\nabla p \sim p_c / R$  and  $\nabla p_a \sim p_{c,a} / R$ , where  $p_c$  and  $p_{c,a}$  denote the characteristic pressure scales for the droplet and ambient fluid, respectively. The pressure gradient scale of the droplet reflects the fact that the radial pressure gradient dominates over the axial one owing to the thin-gap geometry ( $\delta \ll 1$ ). Finally, the gravitational stresses scale as  $\rho g H_0$  and  $\rho_a g R$  for the droplet and the ambient fluid, respectively.

Using the above scaling arguments, we non-dimensionalize the governing equations in Eqn. (3.2) to obtain the following dimensionless mass and momentum conservation equations for the micro-droplet [Eqns. (3.7a) and (3.7b)] and the ambient fluid [Eqns. (3.7c) and (3.7d)]:

$$\hat{\nabla} \cdot \hat{\mathbf{u}} = \mathbf{0}, \quad (3.7a)$$

$$\text{Re} \left( \frac{\partial \hat{\mathbf{u}}}{\partial \hat{t}} + \varepsilon \hat{\mathbf{u}} \cdot \hat{\nabla}_{\parallel} \hat{\mathbf{u}} \right) = -\frac{p_c}{\varepsilon \mu_0 \omega / \delta^2} \hat{\nabla}_{\parallel} \hat{p} - \text{Gr} \mathbf{e}_z + \hat{\nabla} \cdot \hat{\boldsymbol{\tau}}, \quad (3.7b)$$

$$\hat{\nabla}_{\parallel} \cdot \hat{\mathbf{u}}_a = \mathbf{0}, \quad (3.7c)$$

$$\text{Re}_a \left( \frac{\partial \hat{\mathbf{u}}_a}{\partial \hat{t}} + \varepsilon \hat{\mathbf{u}}_a \cdot \hat{\nabla}_{\parallel} \hat{\mathbf{u}}_a \right) = -\frac{p_{c,a}}{\varepsilon \mu_a \omega} \hat{\nabla}_{\parallel} \hat{p}_a - \text{Gr}_a \mathbf{e}_z + \hat{\nabla}_{\parallel} \cdot \hat{\boldsymbol{\tau}}_a. \quad (3.7d)$$

Here, all variables with hats ( $\hat{\cdot}$ ) are rendered dimensionless using the characteristic scales defined earlier.

The Reynolds number of the droplet is defined as  $\text{Re} = \rho \omega H_0^2 / \mu_0 = \delta^2 \rho \omega R^2 / \mu_0$ , based on the unsteady inertial stress scale  $\varepsilon \delta \rho \omega^2 R^2$ ; similarly, that of the ambient fluid is  $\text{Re}_a = \rho_a \omega R^2 / \mu_a$ . The

gradient operators are non-dimensionalized as  $\hat{\nabla} = H_0 \nabla$  and  $\hat{\nabla}_{\parallel} = R_0 \nabla$ , corresponding to the axial and radial scalings, respectively. The ratios of gravitational to viscous stresses are captured through the gravity numbers  $\text{Gr} = \delta^2 \rho g R / (\varepsilon \mu_0 \omega)$  and  $\text{Gr}_a = \rho_a g R / (\varepsilon \mu_a \omega)$  for the droplet and the ambient fluid, respectively. The dimensionless deviatoric stress tensor of the ambient fluid is given by  $\hat{\boldsymbol{\tau}}_a = 2\hat{\mathbf{E}}_a$  and that for the droplet follows from Eqn. (3.3):

$$\hat{\boldsymbol{\tau}}(\hat{t}) = 2 \int_0^\infty \left[ \hat{G}(\hat{\tau}) \hat{\mathbf{E}}(\hat{t} - \hat{\tau}) \right] d\hat{\tau}. \quad (3.8)$$

Here,  $\hat{G}(\hat{\tau}) = G(\tau) / (\mu_0 \omega) = \exp(-\hat{\tau}/\text{De}) / \text{De}$  is the dimensionless relaxation modulus, with  $\hat{\tau} = \omega \tau$  and  $\text{De} = \lambda \omega$  denoting the Deborah number of the droplet.

Owing to the micron-scale radius  $R$  of the substrates used to pin a microdroplet, the Reynolds and gravity numbers for both the droplet and ambient fluid satisfy  $(\text{Re}, \text{Re}_a, \text{Gr}, \text{Gr}_a) \ll 1$ . In this negligible-inertia, low-gravity regime, Eqns. (3.7b) and (3.7d) imply that pressure balances the bulk viscous stresses at leading order in both phases. Accordingly, the pressure scale in the droplet is the lubrication pressure scale  $p_c = \varepsilon \mu_0 \omega / \delta^2$ , while that in the ambient fluid is the viscous pressure scale  $p_{c,a} = \varepsilon \mu_a \omega$ .

Furthermore, due to the negligible effects of gravity, the hydrostatic pressure fields in the droplet and ambient fluid, denoted  $P$  and  $P_a$ , are spatially uniform at leading order. Their difference, the Laplace pressure  $\Delta P = P - P_a$ , is balanced by the static curvature-induced capillary stresses  $2\gamma \mathcal{H}_0 = \gamma/R$ , where  $\mathcal{H}_0 = 1/(2R)$  is the constant static mean curvature. This balance, known as the Young–Laplace equation, corresponds to the static limit of the interfacial stress balance (3.5) in the regime  $\text{Bo} \ll 1$ . As a result, the static pressures  $P$  and  $P_a$  scale as  $\gamma/R$ .

The characteristic stress scales for the droplet include the lubrication pressure scale  $p_c = \varepsilon \mu_0 \omega / \delta^2$ , which characterizes the dominant bulk stresses arising from strong radial pressure gradients in the thin-gap geometry, and the  $\mathcal{O}(\delta)$  smaller viscous stress scale  $\varepsilon \mu_0 \omega / \delta$ . We adopt  $p_c$  as the reference scale for the droplet stress  $\boldsymbol{\sigma}$ . For the ambient fluid, the natural stress scale is the viscous stress scale  $p_{c,a} = \varepsilon \mu_a \omega$ . Between these, the droplet stress scale  $p_c$  is typically dominant, as the viscosity ratio  $\hat{\mu} = \mu_a / \mu_0 \lesssim 1$  in most practical settings.

Accordingly, we non-dimensionalize the interfacial stress balance (3.5) by dividing through by  $p_c$ , yielding:

$$\mathbf{n} \cdot (\hat{\mu} \delta^2 \hat{\boldsymbol{\sigma}}_a - \hat{\boldsymbol{\sigma}}) = (\delta^2 / \varepsilon) \text{Ca}_0^{-1} \mathbf{n} \left( \hat{\nabla}_{\parallel} \cdot \mathbf{n} \right), \quad (3.9)$$

where the dimensionless stress tensors are defined as  $\hat{\boldsymbol{\sigma}}_a = \boldsymbol{\sigma}_a / (\varepsilon \mu_a \omega)$  and  $\hat{\boldsymbol{\sigma}} = \delta^2 \boldsymbol{\sigma} / (\varepsilon \mu_0 \omega)$ . In experiments, the strain amplitude  $\varepsilon$  and aspect ratio  $\delta$  are typically chosen such that  $\varepsilon \sim \delta^2$  [13, 37, 58, 150]. Under this scaling, the capillary number of the droplet  $\tilde{\text{Ca}}_0 = \varepsilon \mu_0 R \omega / (\delta^2 \gamma)$ , based on the zero-shear viscosity  $\mu_0$ , reduces to  $\text{Ca}_0 = \mu_0 R \omega / \gamma$ . This nondimensional group represents the ratio of viscous stresses arising from lubrication pressure to curvature-induced capillary stresses, and is consistent with the capillary number defined by Barakat et al. [13].

In axisymmetric cylindrical coordinates, the unit normal to the droplet interface is given by

$$\mathbf{n}(z, t) = \frac{\mathbf{e}_r - \mathcal{R}' \mathbf{e}_z}{(1 + \mathcal{R}'^2)^{1/2}}.$$

Substituting this into the kinematic boundary condition (3.6) gives us, in dimensionless form,

$$\frac{\partial \hat{\mathcal{R}}}{\partial \hat{t}}(\hat{z}, \hat{t}) = \varepsilon \left[ \hat{u}_r(\hat{\mathcal{R}}, \hat{z}, \hat{t}) - \hat{\mathcal{R}}'(\hat{z}, \hat{t}) \hat{u}_z(\hat{\mathcal{R}}, \hat{z}, \hat{t}) \right], \quad (3.10)$$

where the dimensionless variables  $\hat{\mathcal{R}} = \mathcal{R}/R$ ,  $\hat{t} = \omega t$ ,  $\hat{z} = z/H_0$ ,  $\hat{\mathcal{R}}' = \partial \hat{\mathcal{R}} / \partial \hat{z} = \delta \hat{\mathcal{R}}'$ ,  $\hat{u}_r = u_r / (\varepsilon R \omega)$ , and  $\hat{u}_z = u_z / (\varepsilon H_0 \omega)$ .

### 3.3.2 Asymptotic analysis and anatomy of the interfacial stress balance

Having expressed the governing equations and boundary conditions for the droplet and the ambient fluid in dimensionless form, we now proceed with an asymptotic analysis to reveal the leading-order dynamics of the coupled droplet–ambient fluid–substrates system, as the upper substrate undergoes small-amplitude oscillations ( $\varepsilon \ll 1$ ), while maintaining a thin gap between the substrates ( $\delta^2 \ll 1$ ). As discussed previously, the micron-scale substrate radius ensures that inertial and gravitational effects are negligible at leading order. In particular, the Reynolds and gravity numbers for both the droplet and the ambient fluid are of  $\mathcal{O}(\varepsilon^2)$  or smaller.

Under these assumptions, we expand the velocity, dynamic pressure, and all other relevant fields of the droplet as regular perturbation series in  $\delta^2$  and  $\varepsilon$ , and those of the ambient fluid as regular perturbation series in  $\varepsilon$ :

$$\hat{\mathbf{u}} = \hat{\mathbf{u}}_0 + \delta^2 \hat{\mathbf{u}}_1^{(1)} + \varepsilon \hat{\mathbf{u}}_1^{(2)} + \mathcal{O}(\delta^4, \varepsilon \delta^2, \varepsilon^2), \quad (3.11a)$$

$$\hat{p}_d = \hat{p} - (\delta^2/\varepsilon) \text{Ca}_0^{-1} \hat{P} = \hat{p}_{d,0} + \delta^2 \hat{p}_{d,1}^{(1)} + \varepsilon \hat{p}_{d,1}^{(2)} + \mathcal{O}(\delta^4, \varepsilon \delta^2, \varepsilon^2), \quad (3.11b)$$

$$\hat{\mathbf{u}}_a = \hat{\mathbf{u}}_{a,0} + \varepsilon \hat{\mathbf{u}}_{a,1} + \mathcal{O}(\varepsilon^2), \quad (3.11c)$$

$$\hat{p}_{a,d} = \hat{p}_a - (\varepsilon \hat{\mu} \text{Ca}_0)^{-1} \hat{P}_a = \hat{p}_{a,d,0} + \varepsilon \hat{p}_{a,d,1} + \mathcal{O}(\varepsilon^2). \quad (3.11d)$$

Here,  $\hat{p}_d = \delta^2 p_d / (\varepsilon \mu_0 \omega)$  and  $\hat{p}_{a,d} = p_{a,d} / (\varepsilon \mu_a \omega)$  denote the dimensionless dynamic pressures, while  $\hat{P} = RP/\gamma$  and  $\hat{P}_a = RP_a/\gamma$  represent the dimensionless static pressures.

We briefly remark on an apparent inconsistency that arises in the limit  $\varepsilon \rightarrow 0$  (i.e., when the upper substrate is stationary), wherein the perturbation expansions for the droplet fields reduce to the form

$$f = f_0 + \delta^2 f_1^{(1)} + \mathcal{O}(\delta^4),$$

rather than vanishing identically as is expected in the static configuration. A related concern may arise regarding the origin of flow and dynamic pressure fields at  $\mathcal{O}(1)$ , despite the applied motion entering at  $\mathcal{O}(\varepsilon)$ . These inconsistencies are resolved by recognizing that the characteristic scalings of the velocity and dynamic pressure fields themselves involve  $\varepsilon$ , such that the expansions are effectively rescaled by  $1/\varepsilon$ . As a result, a correction at  $\mathcal{O}(\varepsilon^n)$  in the scaled expansions corresponds to an  $\mathcal{O}(\varepsilon^{n-1})$  term in the unscaled physical fields.

Consequently, in the above expansions, the static fields reside at  $\mathcal{O}(1/\varepsilon)$ , while the leading-order dynamic response appears at  $\mathcal{O}(1)$ . Specifically, since  $\hat{\mathbf{u}} = \mathbf{u}/(\varepsilon R\omega)$ ,  $\hat{\mathbf{u}}_a = \mathbf{u}/(\varepsilon R\omega)$ ,  $\hat{p} = \delta^2 p / (\varepsilon \mu_0 \omega)$ , and  $\hat{p}_a = p_a / (\varepsilon \mu_a \omega)$ , it follows that  $(\mathbf{u}, \mathbf{u}_a, p_d, p_{a,d}) \rightarrow 0$ , and  $p \rightarrow P$ ,  $p_a \rightarrow P_a$  in the limit  $\varepsilon \rightarrow 0$ , consistent with the quiescent static state. A similar interpretation applies to the perturbation expansions for the ambient fluid. Thus, the perceived discrepancy is not a physical inconsistency, but rather a consequence of the chosen characteristic scales involving a perturbation parameter.

Substituting the perturbation expansions in Eqn. (3.11) into the dimensionless governing equations in Eqn. (3.7), we obtain, at leading order in  $\varepsilon$  and  $\delta^2$ , the lubrication equations for the droplet [Eqns. (3.12a) and (3.12b)], and at leading order in  $\varepsilon$ , the Stokes equations for the ambient fluid [Eqns. (3.12c) and (3.12d)], valid in the limit of negligible inertia ( $\text{Re}, \text{Re}_a \ll 1$ ) and low gravity ( $\text{Gr}, \text{Gr}_a \ll 1$ ):

$$\hat{\nabla} \cdot \hat{\mathbf{u}}_0 = \mathbf{0}, \quad (3.12a)$$

$$0 = -\frac{\partial \hat{p}_{d,0}}{\partial \hat{r}} + \int_0^\infty \left[ \hat{G}(\hat{\tau}) \frac{\partial^2}{\partial \hat{z}^2} \hat{u}_{0,r}(\hat{t} - \hat{\tau}) \right] d\hat{\tau}, \quad (3.12b)$$

$$\hat{\nabla}_\parallel \cdot \hat{\mathbf{u}}_{a,0} = \mathbf{0}, \quad (3.12c)$$

$$\mathbf{0} = -\hat{\nabla}_\parallel \hat{p}_{a,d,0} + \hat{\nabla}_\parallel^2 \mathbf{u}_{a,0}. \quad (3.12d)$$

Here,  $\hat{\nabla}_{\parallel}^2 = \hat{\nabla}_{\parallel} \cdot \hat{\nabla}_{\parallel}$  is the dimensionless radial Laplacian.

Utilizing the regular expansions in Eqn. (3.11), the dimensionless stress tensors of the ambient fluid and the droplet can be expanded as:

$$\hat{\sigma}_a = -(\varepsilon \hat{\mu} \text{Ca}_0)^{-1} \hat{P}_a \mathbf{I} - \hat{p}_{a,d,0} \mathbf{I} + 2\hat{\mathbf{E}}_{a,0} + \mathcal{O}(\varepsilon), \quad (3.13a)$$

$$\hat{\sigma} = -(\delta^2/\varepsilon) \text{Ca}_0^{-1} \hat{P} \mathbf{I} - \hat{p}_{d,0} \mathbf{I} + \delta \hat{\tau}_0 + \mathcal{O}(\delta^2, \varepsilon). \quad (3.13b)$$

Here,  $\hat{\mathbf{E}}_{a,0}$  denotes the leading-order rate-of-strain tensor of the ambient fluid, while  $\hat{\tau}_0$  is the leading-order deviatoric stress tensor of the droplet, related to its leading-order rate-of-strain tensor via the Maxwell model in Eqn. (3.8). Substituting these expansions into the dimensionless interfacial stress balance (3.9), and noting that the Bond number  $\text{Bo} \lesssim \varepsilon^2$ , we obtain:

$$\begin{aligned} \mathbf{n} \cdot \left[ (\delta^2 \text{Ca}_0^{-1}) \Delta \hat{P} \mathbf{I} + \varepsilon \left\{ \hat{p}_{d,0} \mathbf{I} - \delta \hat{\tau}_0 + \hat{\mu} \delta^2 \left( -\hat{p}_{a,d,0} \mathbf{I} + 2\hat{\mathbf{E}}_{a,0} \right) \right\} \right]_{\hat{r}=\hat{R}} + \mathcal{O}(\varepsilon \delta^2, \varepsilon^2) \\ = (\delta^2 \text{Ca}_0^{-1}) \mathbf{n} \left( \hat{\nabla}_{\parallel} \cdot \mathbf{n} \right), \end{aligned} \quad (3.14)$$

where the constant  $\Delta \hat{P} = \hat{P} - \hat{P}_a$  is the dimensionless Laplace pressure difference.

Taking the mean of the typical substrate radius range 10–100 μm as the characteristic radius, we set  $R = 5.5 \times 10^{-4}$  m. For an oscillation frequency  $\omega = 2\pi \text{s}^{-1}$  such that the Deborah number  $\text{De} = \lambda\omega = \mathcal{O}(1)$ , and a typical interfacial tension  $\gamma = 5 \times 10^{-2}$  N/m, the capillary number of a typical viscoelastic microdroplet is estimated as  $\text{Ca}_0 = \mu_0 R \omega / \gamma \approx 6.91 \times 10^{-3} \mu_0$ . For highly viscous (relative to water) viscoelastic microdroplets with zero-shear viscosity  $\mu_0 \approx 1.5\text{--}10$  Pa · s—such as concentrated aqueous polymer solutions, food-grade Boger fluids, xanthan gum solutions, or wormlike micellar solutions—we obtain  $\text{Ca}_0 \sim 10^{-2}\text{--}10^{-1}$ .

Accordingly, in experiments, one can select strain amplitudes  $\varepsilon$  in the range 1%–10%, and choose the gap aspect ratio such that  $\delta \sim \varepsilon^{1/2}$ , thereby ensuring that  $\text{Ca}_0 \sim \varepsilon \sim \delta^2$ . This scaling yields  $\delta^2 \text{Ca}_0^{-1} = \mathcal{O}(1)$ , so that curvature-induced capillary stresses appear at leading order in the interfacial stress balance (3.14). Physically, this implies that the capillary stresses dominate the bulk viscous stresses induced by lubrication pressure by a factor of  $\mathcal{O}(1/\delta^2)$ .

Before proceeding further, we note that in the small strain amplitude limit ( $\varepsilon \ll 1$ ), the dimensionless interface shape function  $\hat{r} = \hat{\mathcal{R}}(\hat{z}, \hat{t})$  and the interface unit normal  $\mathbf{n}(\hat{z}, \hat{t})$  can be expanded in a regular perturbation series in  $\varepsilon$  about their static configurations, neglecting corrections due to the weak gravitational effects at  $\text{Bo} \ll 1$ :

$$\hat{\mathcal{R}}(\hat{z}, \hat{t}) = 1 + \varepsilon \hat{\mathcal{R}}_1(\hat{z}, \hat{t}) + \mathcal{O}(\varepsilon^2), \quad (3.15a)$$

$$\mathbf{n}(\hat{z}, \hat{t}) = \mathbf{e}_r + \varepsilon \mathbf{n}_1(\hat{z}, \hat{t}) + \mathcal{O}(\varepsilon^2). \quad (3.15b)$$

Here,  $\hat{\mathcal{R}}_1(\hat{z}, \hat{t})$  and  $\mathbf{n}_1(\hat{z}, \hat{t})$  represent the leading-order corrections associated with the deformation of the interface.

From the expansion of the shape function  $\mathcal{R}(z, t)$  above, we note that although the interface shape scales with the substrate radius  $R$  and the axial deformation scale with  $H_0$ , this does not imply that the interface slope  $\mathcal{R}' = d\mathcal{R}/dz$  scales as  $R/H_0 = 1/\delta \gg 1$ . Such a scaling would contradict the presence of small interface slopes during small-amplitude oscillatory perturbations ( $\varepsilon \ll 1$ ) about a static cylindrical shape. Instead, the correct scaling obtained from the expansion is  $\mathcal{R}' \sim \varepsilon \mathcal{R}'_1 \sim \varepsilon/\delta$ , where  $\mathcal{R}'_1 = \partial \mathcal{R}_1/\partial z$ .

As established earlier, in typical experiments  $\varepsilon \sim \delta^2$ , yielding  $\mathcal{R}' \sim \delta \ll 1$ , which is physically consistent with the appearance of small slopes. For larger deformations about the static cylindrical shape, where  $\varepsilon \gtrsim \delta$ , the slope becomes  $\mathcal{R}' \gtrsim 1$ , indicating the emergence of steeper profiles as

expected. Throughout the remainder of the analysis, we adopt the small-slope approximation  $\mathcal{R}' \sim \varepsilon/\delta \sim \delta \ll 1$ , consistent with the scaling  $\varepsilon \sim \delta^2$ .

For highly viscous viscoelastic microdroplets satisfying the constraint  $\text{Ca}_0 \sim \delta^2$ , the leading-order interfacial stress balance (3.14), at  $\mathcal{O}(\delta^2 \text{Ca}_0^{-1})$ , reduces to the Young–Laplace equation, or the static interfacial stress balance, in the limit  $\text{Bo} \ll 1$ :

$$\Delta \hat{P} = 1, \quad (3.16)$$

as previously discussed. The deviatoric stresses of the droplet enter the interfacial stress balance at  $\mathcal{O}(\varepsilon \delta)$ , whereas the dynamic pressure and deviatoric stresses from the ambient fluid enter at  $\mathcal{O}(\hat{\mu} \varepsilon \delta^2)$ . Since  $\hat{\mu} \lesssim 1$ , these contributions are subdominant and do not influence the interfacial stress balance at  $\mathcal{O}(\varepsilon)$ . Thus, at  $\mathcal{O}(\varepsilon)$ , the interfacial stress balance (3.14) reduces to a balance between the leading-order dynamic pressure and the dynamic curvature stresses:

$$\hat{p}_{d,0}(\hat{R}, \hat{t}) = (\delta^2 \text{Ca}_0^{-1}) \hat{\nabla}_\parallel \cdot \mathbf{n}_1. \quad (3.17)$$

For low and moderate viscosity microdroplets, the capillary number satisfies  $\text{Ca}_0 \lesssim \varepsilon^2 \sim \delta^4$ , implying that  $\delta^2 \text{Ca}_0^{-1} \gtrsim 1/\delta^2$ . Proceeding as in the case of highly viscous droplets, the interfacial stress balance (3.14) yields the static balance (3.16) at leading order in  $\varepsilon$ , i.e., at  $\mathcal{O}(\delta^4 \text{Ca}_0^{-1})$ . However, in contrast to that case, at  $\mathcal{O}(\varepsilon \delta^4 \text{Ca}_0^{-1}) = \mathcal{O}(\varepsilon)$ , we obtain

$$0 = \hat{\nabla}_\parallel \cdot \mathbf{n}_1, \quad (3.18)$$

which implies that the shape of the interface remains unchanged at  $\mathcal{O}(\varepsilon)$ .

This arises because the capillary stresses dominate over the bulk viscous (and elastic) stresses induced by lubrication pressure by a factor of  $\mathcal{O}(1/\delta^4)$  or more, i.e., larger by an  $\mathcal{O}(1/\delta^2)$  compared to the highly viscous droplet case. As such, the bulk rheological stresses arising due to the thin gap are too weak to deform the interface at  $\mathcal{O}(\varepsilon)$ , rendering the interface effectively stiff at this order despite the  $\mathcal{O}(\varepsilon)$  perturbation from the upper substrate. Instead, the bulk rheological stresses balance the dynamic curvature stresses starting from the next order,  $\mathcal{O}(\varepsilon \delta^2) = \mathcal{O}(\varepsilon^2) = \mathcal{O}(\varepsilon^2 \delta^4 \text{Ca}_0^{-1})$ , and hence the shape of the interface changes at this order. Eqn. (3.18) also follows directly from Eqn. (3.17) by letting  $\text{Ca}_0 \lesssim \delta^4$ , which causes the leading-order dynamic pressure on the left-hand side to drop to  $\mathcal{O}(\varepsilon \delta^2)$  or lower.

There exist several viscoelastic fluids whose zero-shear viscosities lie in the range 100–1000 Pa·s, including low-density polyethylene (LDPE) melts, polydimethylsiloxane (PDMS) gums, lightly cross-linked silicone gels, and entangled synthetic polymer solutions. For microdroplets of these fluids, the capillary number satisfies  $1 \lesssim \text{Ca}_0 \lesssim \varepsilon^{-1} = \delta^{-2}$ , implying that the bulk rheological stresses are either comparable to capillary stresses when  $\text{Ca}_0 = \mathcal{O}(1)$ , or dominate over them by a factor of  $\mathcal{O}(1/\delta^2)$  when  $\text{Ca}_0 \sim 1/\delta^2$ . In the case  $\text{Ca}_0 = \mathcal{O}(1)$ , the static interfacial stress balance (3.16) enters Eqn. (3.14) at  $\mathcal{O}(\delta^2 \text{Ca}_0^{-1}) = \mathcal{O}(\delta^2)$ , whereas the zero dynamic pressure boundary condition

$$\hat{p}_{d,0}(\hat{R}, \hat{t}) = 0, \quad (3.19)$$

emerges at  $\mathcal{O}(\varepsilon)$  as the leading-order dynamic equation. The fact that the static curvature stresses and the bulk rheological stresses due to lubrication pressure effectively enter at the same order ( $\varepsilon \sim \delta^2$ ) is consistent with  $\text{Ca}_0 = \mathcal{O}(1)$ . The leading-order dynamic curvature stresses appear at  $\mathcal{O}(\varepsilon \delta^2 \text{Ca}_0^{-1}) = \mathcal{O}(\varepsilon^2)$  and hence influence the dynamic pressure starting at this order through the first-order correction  $\hat{p}_{d,1}$ .

On the other hand, when  $\text{Ca}_0 \sim 1/\delta^2$ , we have  $\delta^2 \text{Ca}_0^{-1} \sim \delta^4 \sim \varepsilon^2$ , and thus the leading-order interfacial stress balance (3.14), at  $\mathcal{O}(\varepsilon)$  yields the zero dynamic pressure boundary condition (3.19). This is consistent with the pressure boundary condition imposed by previous works such as Phan-Thien [55] and Wingstrand et al. [58] in the high-capillary-number ( $\text{Ca}_0 \gg 1$ ) regime. At the next order,  $\mathcal{O}(\varepsilon \delta)$ , Eqn. (3.14) yields the zero normal deviatoric stress condition:

$$\mathbf{n} \cdot \boldsymbol{\tau}_0 = \mathbf{0}.$$

At the subsequent order,  $\mathcal{O}(\delta^2 \text{Ca}_0^{-1}) = \mathcal{O}(\varepsilon^2)$ , the Young–Laplace equation (3.16) finally appears as the static equation. The zero dynamic pressure boundary condition (3.18) also follows directly from Eqn. (3.17) by letting  $\text{Ca}_0 \gtrsim 1$ , in which case the leading-order dynamic curvature stresses on the right-hand side shift to  $\mathcal{O}(\varepsilon \delta^2)$  or lower.

The foregoing analysis demonstrates that Eqn. (3.17) remains valid across all regimes of the capillary number  $\text{Ca}_0$  for viscoelastic droplets. Consequently, the analytical framework developed here applies to both highly and weakly viscous droplets, whether microscopic or macroscopic, with  $\text{Ca}_0$  serving as the principal dimensionless parameter governing the interplay between interfacial and bulk dynamics, as claimed at the outset of this section. In retrospect, we also identify the elasto-capillary number  $\text{Ec}_0 = G_0 R / \gamma$  as a relevant dimensionless group, comparing the bulk elastic stresses due to lubrication pressure to the capillary stresses.

Remarkably, among the various regimes considered, the case  $\text{Ca}_0 \sim \delta^2$ —typical of most viscoelastic microdroplets—is unique in that the leading-order dynamic pressure  $\hat{p}_{d,0}$  balances the leading-order dynamic curvature stresses  $\hat{\nabla}_\parallel \cdot \mathbf{n}_1$ . This framework has also been adopted by Barakat et al. [13] to model the oscillations of millimeter-scale Newtonian droplets (or thin films) with low shear viscosity or low oscillation frequencies. However, their work does not systematically examine how the interfacial stress balance (3.14) breaks down at successive orders in  $\varepsilon$  across different  $\text{Ca}_0$  regimes, beyond a general assertion that they operate in the  $\text{Ca}_0 \ll 1$  limit.

The leading-order, i.e.  $\mathcal{O}(\varepsilon)$ , correction to the kinematic boundary condition (3.10) is obtained by substituting the regular expansions of the interface shape function  $\hat{\mathcal{R}}(\hat{z}, \hat{t})$  and the droplet velocity field from Eqns. (3.15a) and (3.11a), respectively:

$$\frac{\partial \hat{\mathcal{R}}_1}{\partial \hat{t}}(\hat{z}, \hat{t}) = \hat{u}_{0,r}(\hat{\mathcal{R}}, \hat{z}, \hat{t}), \quad (3.20)$$

where  $\hat{u}_{0,r} = \mathbf{e}_r \cdot \hat{\mathbf{u}}_0$  denotes the leading-order radial component of the droplet velocity field. This equation indicates that the leading-order dynamic correction to the deforming interface shape  $\hat{\mathcal{R}}_1$  is determined solely by the radial component of the lubrication velocity field.

This shape correction then governs the lubrication pressure field  $\hat{p}_{d,0}$  via the leading-order dynamic interfacial stress balance (3.17). Under the small-slope approximation  $\mathcal{R}' \sim \varepsilon/\delta \ll 1$ , valid for small-amplitude oscillations ( $\varepsilon \ll 1$ ) in a thin gap ( $\delta^2 \ll 1$ ), this stress balance reduces to:

$$\hat{p}_{d,0}(\hat{\mathcal{R}}, \hat{t}) = -\text{Ca}_0^{-1} \left( \delta^2 \hat{\mathcal{R}}_1 + \hat{\mathcal{R}}_1'' \right). \quad (3.21)$$

Here, the first term on the right-hand side corresponds to the leading-order dynamic correction to the azimuthal curvature, and the second term represents the corresponding meridional contribution. As anticipated in the thin-gap limit, the meridional curvature term is asymptotically larger by a factor of  $\mathcal{O}(\delta^{-2})$  relative to the azimuthal counterpart. Details of this derivation are provided in Appendix A.

### 3.3.3 Post-transient response

Owing to the oscillatory motion of the upper substrate while the lower substrate remains fixed, the leading-order velocity and pressure fields of the droplet in the post-transient regime take the form of time-periodic solutions at the driving angular frequency  $\omega$ . As such, these fields may be expressed as  $\hat{\mathbf{u}}_0(\hat{\mathbf{x}}, \hat{t}) = \tilde{\mathbf{u}}_0(\hat{\mathbf{x}}) e^{i\hat{t}} + \text{cc}$  and  $\hat{p}_{d,0}(\hat{\mathbf{x}}, \hat{t}) = \tilde{p}_{d,0}(\hat{\mathbf{x}}) e^{i\hat{t}} + \text{cc}$ , where  $\tilde{\mathbf{u}}_0(\hat{\mathbf{x}})$  and  $\tilde{p}_{d,0}(\hat{\mathbf{x}})$  are complex-valued, spatially varying amplitudes,  $\hat{\mathbf{x}} = \mathbf{x}/R$  denotes the dimensionless position vector,  $i = \sqrt{-1}$ , and cc denotes the complex conjugate of the preceding term. Substituting these expressions into the governing lubrication equations (3.12a) and (3.12b), we obtain the following governing equations for the complex velocity and pressure fields of the droplet:

$$\frac{1}{\hat{r}} \frac{\partial}{\partial \hat{r}} (\hat{r} \tilde{u}_{0,r}) + \frac{\partial \tilde{u}_{0,z}}{\partial \hat{z}} = 0, \quad (3.22a)$$

$$\frac{d\tilde{p}_{d,0}}{d\hat{r}} = \mu^* \frac{\partial^2 \tilde{u}_{0,r}}{\partial \hat{z}^2}. \quad (3.22b)$$

Here,  $\mu^*$  is the dimensionless complex viscosity of the droplet, defined as

$$\mu^* = \int_0^\infty [\hat{G}(\hat{\tau}) e^{-i\hat{\tau}}] d\hat{\tau} = \frac{1}{\mu_0 \omega} (G'' - i G'),$$

with the explicit expressions of the loss and shear moduli given by  $G'' = \mu_0 \omega / (1 + De^2)$  and  $G' = G_0 / (1 + De^{-2})$ , respectively [31, 32, 34, 36, 146]. It is not necessary to solve the governing Stokes equations for the ambient fluid (3.12c) and (3.12d), as the ambient flow does not influence the leading-order dynamics at  $\mathcal{O}(\varepsilon)$ . As discussed in Section 3.3.2, its effect influences the droplet dynamics through the interfacial stress balance (3.14) only at the subdominant order  $\mathcal{O}(\varepsilon \delta^2 \hat{\mu})$ .

Integrating the momentum conservation equation (3.22b) twice with respect to  $\hat{z}$  yields a parabolic profile (at any fixed radial position) for the radial component of the droplet velocity field:

$$\tilde{u}_{0,r}(\hat{r}, \hat{z}) = -\frac{1}{2\mu^*} \frac{d\tilde{p}_{d,0}}{d\hat{r}} \hat{z}(1 - \hat{z}), \quad (3.23)$$

where the integration functions have been determined by invoking the no-slip boundary conditions at the lower substrate ( $\hat{z} = 0$ ) and the upper substrate [ $\hat{z} = 1 + \varepsilon \sin \hat{t} = 1 + \mathcal{O}(\varepsilon)$ ]. Substituting this velocity profile into the mass conservation equation (3.22a) and integrating over the entire substrate gap  $\hat{z} \in [0, 1 + \mathcal{O}(\varepsilon)]$ , while applying the no-slip (or no-penetration) boundary conditions for the axial velocity component  $\tilde{u}_{0,z}$  at both substrates, we obtain the following differential equation for the dynamic pressure:

$$\frac{d}{d\hat{r}} \left( \hat{r} \frac{d\tilde{p}_{d,0}}{d\hat{r}} \right) = 12\mu^* \hat{r}.$$

Solving this equation under the axisymmetric condition  $d\tilde{p}_{d,0}/d\hat{r} = 0$  at  $\hat{r} = 0$  leads to the following radially parabolic profile for the leading-order dynamic pressure field:

$$\tilde{p}_{d,0}(\hat{r}) = 3\mu^* \hat{r}^2 + \mathcal{P}, \quad (3.24)$$

where  $\mathcal{P}$  is a complex-valued integration constant, to be determined shortly by enforcing the  $\mathcal{O}(\varepsilon)$  stress boundary condition (3.21) at the interface  $\hat{r} = \hat{R} = 1 + \mathcal{O}(\varepsilon)$ .

Substituting the expression for the dynamic pressure field from Eqn. (3.24) into the radial velocity profile in Eqn. (3.23), we obtain the explicit post-transient parabolic profile of the radial velocity component  $\tilde{u}_{0,r}$ . Inserting this profile into the mass conservation equation (3.22a), and applying the

no-slip condition at the lower substrate, gives the explicit post-transient cubic, radially independent profile for the axial velocity component  $\hat{u}_{0,z}$ . These leading-order velocity components are given by:

$$\hat{u}_{0,r}(\hat{r}, \hat{z}, \hat{t}) = -3\hat{r}\hat{z}(1-\hat{z})\cos\hat{t}, \quad (3.25a)$$

$$\hat{u}_{0,z}(\hat{z}, \hat{t}) = \hat{z}^2(3-2\hat{z})\cos\hat{t}. \quad (3.25b)$$

To determine the pressure constant  $\mathcal{P}$ , we first evaluate the leading-order dynamic shape of the interface  $\hat{\mathcal{R}}_1(\hat{z}, \hat{t})$  by substituting the radial velocity profile  $\hat{u}_{0,r}$  from Eqn. (3.25a) at the interface  $\hat{r} = \hat{\mathcal{R}} = 1 + \mathcal{O}(\varepsilon)$  into the kinematic condition (3.20). Solving the resulting linear differential equation with the initial condition  $\hat{\mathcal{R}}_1(\hat{t}=0)=0$ , which enforces an initially undeformed interface, yields the following parabolic profile:

$$\hat{\mathcal{R}}_1(\hat{z}, \hat{t}) = -3\hat{z}(1-\hat{z})\sin\hat{t}. \quad (3.26)$$

As discussed earlier, we now substitute this shape into the interfacial stress balance (3.21), and retain only the dominant meridional curvature term while neglecting the  $\mathcal{O}(\delta^2)$  smaller azimuthal term. This gives us the following relation for the pressure constant  $\mathcal{P}$ :

$$\frac{1}{2}(\mathcal{P}e^{i\hat{t}} + cc) = -6Ca_0^{-1}\sin\hat{t} - \frac{3}{\mu_0\omega}(G'\sin\hat{t} + G''\cos\hat{t}).$$

Substituting the above relation for the pressure constant  $\mathcal{P}$  into Eqn. (3.24), we obtain the explicit form of the leading-order dynamic pressure field:

$$\hat{p}_{d,0}(\hat{r}, \hat{t}) = \frac{3}{\mu_0\omega}(G'\sin\hat{t} + G''\cos\hat{t})(\hat{r}^2 - 1) - 6Ca_0^{-1}\sin\hat{t}. \quad (3.27)$$

Although the lubrication velocity field, given in Eqn. (3.25), is independent of the material properties of the droplet and solely governs the leading-order interface deformation, the lubrication pressure field  $\hat{p}_{d,0}$  receives feedback both from this deformation and from the bulk rheological stresses of the droplet. As a result, in the linear (small deformation) regime, the dynamic pressure exhibits a linear dependence on the material parameters of the droplet. Specifically, the term proportional to the storage modulus  $G'$  reflects the contribution of bulk elastic stresses that are in-phase with the imposed strain  $(H/H_0 - 1) = \varepsilon \sin\hat{t}$ ; the term proportional to the loss modulus  $G''$  accounts for bulk viscous stresses that are out-of-phase by  $\pi/2$ ; and the in-phase term proportional to the inverse capillary number  $Ca_0^{-1}$  (dependent on the interfacial tension  $\gamma$ ) captures the contribution of curvature-induced interfacial stresses.

The force  $F\mathbf{e}_z$  exerted by the deforming droplet on the lower substrate, i.e., the force response, can be expressed as a regular perturbation expansion in  $\varepsilon$ :

$$\hat{F}(\hat{t}) = \hat{F}_0 + \varepsilon \hat{F}_1(\hat{t}) + \mathcal{O}(\varepsilon^2), \quad (3.28)$$

where the dimensionless force response  $\hat{F} = F/(\pi\gamma R)$ . The leading-order term  $\hat{F}_0 = 1$  refers to the static response, comprising two contributions: the Laplace pressure acting over the wetted area of the lower substrate, given by  $-\pi\gamma R\mathbf{e}_z$ , and the static interfacial tension force at the contact line (substrate rim), which exerts a vertical pull of  $2\pi\gamma R\mathbf{e}_z$ . The first-order correction  $\hat{F}_1$  represents the leading-order dynamic force response, consisting of the lubrication pressure field  $\hat{p}_{d,0}$  acting on the wetted area and the dynamic correction to the contact line tension. The latter vanishes at this order, since  $\sin\theta = 1 + \mathcal{O}(\varepsilon^2)$ , making its  $\mathcal{O}(\varepsilon)$  contribution zero.

Consequently, the dimensionless force response accurate up to  $\mathcal{O}(\varepsilon^2)$  becomes:

$$\hat{F}(\hat{t}) = 1 - \frac{2\varepsilon \text{Ca}_0}{\delta^2} \int_0^1 (\hat{r} \hat{p}_{d,0}) d\hat{r} = 1 + \frac{3\varepsilon}{2\delta^2} [(4 + \text{Ec}) \sin \hat{t} + \text{Ca} \cos \hat{t}], \quad (3.29)$$

where the elasto-capillary number based on the frequency-dependent storage modulus is defined as  $\text{Ec} = G'R/\gamma$ , and the capillary number based on the frequency-dependent loss modulus is  $\text{Ca} = G''R/\gamma$ . Here, the dimensionless groups Ec and Ca quantify the contributions of the bulk elastic and viscous stresses arising via the lubrication pressure, respectively, relative to the curvature-induced capillary stresses. As a consistency check, we note that the scaling  $\varepsilon/\delta^2 \sim 1$  ensures that the leading-order dynamic forces are comparable in magnitude to the static interfacial forces.

## 3.4 Results and discussion

In the preceding section, we demonstrated that for a viscoelastic microdroplet pinned (initially at a pinning angle  $\pi/2$ ) between two coaxial circular substrates and subjected to small-amplitude oscillations of the upper substrate (with strain amplitude  $\varepsilon \ll 1$ ), while maintaining a thin gap between the substrates (aspect ratio  $\delta \ll 1$ ), the dimensionless force response accurate to  $\mathcal{O}(\varepsilon^2)$  is given by Eqn. (3.29). It follows directly from this expression, or more clearly, when expressed in dimensional form:

$$F(t) = \pi R \gamma + \frac{3\varepsilon \pi R}{2\delta^2} [(4\gamma + RG') \sin(\omega t) + RG'' \cos(\omega t)], \quad (3.30)$$

that the dynamic part of the force response exhibits a linear dependence on all the material properties of the droplet—namely, the interfacial tension  $\gamma$ , the storage modulus  $G'$ , and the loss modulus  $G''$ —consistent with the form of the lubrication pressure in Eqn. (3.27). Specifically, the dynamic curvature stresses (proportional to  $\gamma$ ) and the bulk elastic stresses (proportional to  $G'$ ) appear in-phase with the imposed strain ( $H/H_0 - 1 = \varepsilon \sin(\omega t)$ ), while the bulk viscous stresses (proportional to  $G''$ ) are out-of-phase by  $\pi/2$ . Moreover, the static component of the force depends solely on  $\gamma$ , thereby providing a direct means for its measurement.

Once this force response is experimentally accessible—which is anticipated to be routine within the operational capabilities of the CCFA—each of the above three material properties can be extracted with an accuracy of  $\mathcal{O}(\varepsilon^2)$ . This establishes a robust and precise framework for characterizing the interfacial tension and the bulk rheology of viscoelastic microdroplets. In what follows, we first validate our analytical model by recovering known limiting results in Section 3.4.1, and subsequently demonstrate how the material properties may be systematically inferred from the measured force response in Section 3.4.2.

### 3.4.1 Validation

In the absence of bulk elasticity—or when bulk elastic stresses are negligible compared to dynamic curvature stresses—the force response of a viscoelastic microdroplet is determined by taking the elasto-capillary number  $\text{Ec} \rightarrow 0$  in Eqn. (3.29), or equivalently, by letting the storage modulus  $G' \rightarrow 0$  in Eqn. (3.30). This yields the following dimensional expression:

$$F(t) = \pi R \gamma \left[ 1 + \frac{6R^2}{H_0^2} \left( \frac{H}{H_0} - 1 \right) \right] + \frac{3\pi\mu R^4}{2H_0^3} \frac{dH}{dt}.$$

In this limit, the force comprises contributions from the static interfacial forces (Laplace pressure and contact line tension), dynamic curvature stresses, and bulk viscous stresses, which is precisely

the force response of a Newtonian microdroplet with the constant (frequency-independent) dynamic viscosity  $\mu = G''/\omega$ .

This result agrees exactly with the force response derived by Barakat et al. [13] for a small volume of Newtonian fluid undergoing small-amplitude oscillations between two millimeter-sized coaxial circular substrates (or plates) in a thin-gap configuration, provided the droplet viscosity is small or the actuation frequency is low such that the capillary number  $\bar{\text{Ca}} = \mu\omega R/\gamma \lesssim 1$ . In our case, the corresponding capillary number  $\text{Ca} = G''R/\gamma \lesssim 1$  arises from the micron-scale radius  $R$  of the substrates (or droplet), placing both cases in the same asymptotic regime.

For viscoelastic microdroplets with large storage and loss moduli, the bulk elastic and viscous stresses dominate over the dynamic curvature stresses, i.e.,  $\text{Ec} \gg 1$  and  $\text{Ca} \gg 1$ . In this limit, the force response in Eqn. (3.30) simplifies to:

$$F(t) = \frac{3\pi R^4}{2H_0^2} \left[ G' \left( \frac{H}{H_0} - 1 \right) + \frac{G''}{H_0\omega} \frac{dH}{dt} \right].$$

Here, the bulk rheological stresses are sufficiently strong that the contribution from the deforming interface becomes negligible in the leading-order dynamics—as if the interface were effectively absent. This result precisely matches the force response derived by Phan-Thien [55] and Wingstrand et al. [58] for a thin film of viscoelastic fluid subjected to small-amplitude oscillations between two millimeter-sized coaxial circular substrates, provided the storage and loss moduli of the fluid is sufficiently large to place the system in the asymptotic regime ( $\text{Ec}, \text{Ca} \gg 1$ ).

As a final validation, we consider the asymptotic regime where bulk viscous stresses dominate over curvature stresses, while bulk elastic stresses remain negligible; i.e.,  $\text{Ca} \gg 1$  and  $\text{Ec} \ll 1$ . In this limit, the interface again plays no role at the leading-order dynamics, and the force response reduces to that of a highly viscous Newtonian microdroplet, or equivalently, a thin film of a sufficiently viscous Newtonian fluid subjected to oscillatory squeezing between millimeter-sized coaxial circular substrates. The classical result in this regime, originally derived by Stefan [135], is recovered as:

$$F(t) = \frac{3\pi\mu R^4}{2H_0^3} \frac{dH}{dt},$$

where  $\mu = G''/\omega$  is the constant dynamic viscosity of the droplet. Conversely, in the regime where bulk elastic stresses dominate over curvature stresses and viscous stresses are negligible, i.e.,  $\text{Ec} \gg 1$  and  $\text{Ca} \ll 1$ , the force response reflects the behaviour of a highly elastic, Hookean solid with constant (frequency-independent) shear modulus  $G = G'$  [145]:

$$F(t) = \frac{3\pi GR^4}{2H_0^2} \left( \frac{H}{H_0} - 1 \right).$$

### 3.4.2 Determination of the material properties

The force response given in Eqn. (3.30) may be recast as a single phase-shifted sinusoid with a time-independent offset:

$$F(t) = A + B \sin(\omega t + \phi), \quad (3.31)$$

where

$$A = \pi R\gamma, \quad B = \frac{3\varepsilon\pi R^2}{2\delta^2} (G'_{\text{eff}}^2 + G''^2)^{1/2}, \quad \phi = \arctan \left( \frac{G''}{G'_{\text{eff}}} \right),$$

with  $G'_{\text{eff}} = G' + 4\gamma/R$  denoting the effective storage modulus. In this representation,  $A$  represents the static (offset) component,  $B$  the amplitude of oscillation, and  $\phi$  the phase lag relative to the imposed strain. In typical measurements using the OSFR or CCFA, a function of the form (3.31) is fitted to the measured force data to extract the parameters  $A$ ,  $B$ , and  $\phi$ .

The offset  $A$  provides a direct measurement of the interfacial tension via  $\gamma = A/(\pi R)$ . Substituting this into the expressions for  $B$  and  $\phi$ , the storage and loss moduli are recovered as

$$G' = \left( \frac{2\delta^2 B}{3\varepsilon\pi R^2} \right) \cos \phi - \frac{4A}{\pi R^2}, \quad G'' = \left( \frac{2\delta^2 B}{3\varepsilon\pi R^2} \right) \sin \phi. \quad (3.32)$$

Thus, by performing a frequency sweep, measuring the force response at each frequency, and recording  $A$  (which is ideally independent of frequency),  $B$ , and  $\phi$ , one can determine the interfacial tension  $\gamma$  and the frequency dependence of the viscoelastic moduli  $G'(\omega)$  and  $G''(\omega)$ . Finally, the intrinsic material properties of the viscoelastic microdroplet can be inferred using the relations:

$$\lambda = \frac{G'}{\omega G''}, \quad \mu_0 = \frac{G''}{\omega} (1 + \text{De}^2), \quad G_0 = G' (1 + \text{De}^{-2}),$$

where  $\lambda$  is the relaxation time,  $\mu_0$  the zero-shear viscosity,  $G_0$  the infinite-frequency modulus, and  $\text{De} = \lambda\omega$  is the Deborah number.

### 3.4.3 Limitations

The present model inherits limitations that stem directly from the key assumptions made in its development. Chief among these are that the upper substrate oscillates with small strain amplitudes ( $\varepsilon \ll 1$ ), the gap between the substrates is sufficiently thin ( $\delta^2 \ll 1$ ), the droplet oscillates about an initially cylindrical shape, and axisymmetry is preserved throughout the deformation. Under these conditions, the interface slopes remain small and a lubrication flow field is valid across the droplet. Consequently, the leading-order dynamic interface shape is governed by the radial component of the velocity field. However, this framework becomes questionable when the initial pinning angle takes obtuse values that deviate significantly from  $\pi/2$ .

This point is particularly relevant because the initial cylindrical configuration of the microdroplet considered here is typical and more readily achieved in the OSFR, which primarily operates on macroscopic fluid volumes recast as thin films. In the microdroplet setting of the CCFA, however, attaining an initial pinning angle of  $\pi/2$  while maintaining a thin gap between the capillaries is considerably more challenging. Instead, oscillations are more readily initiated from an obtuse pinning angle that deviates significantly from  $\pi/2$ . In this regime, the droplet may bulge substantially outside the thin-gap region, and the lubrication approximation may no longer remain valid across the entire droplet domain, violating the small-slope approximation. It is then unclear whether the lubrication flow in the thin-gap region continues to dictate the interface shape, or whether a distinct Stokes flow field develops in the bulged-out region—one that couples with the evolving interface shape through the governing conservation equations themselves, rather than solely via the interfacial stress balance and kinematic condition as in the former case.

In the latter scenario, a matched asymptotic framework is required. In this formulation, the lubrication flow is assumed to hold within and near the thin-gap region, while the deforming interface shape is incorporated into the governing Stokes equations in the bulged-out section, yielding a distinct outer flow field. The two regions are then asymptotically matched at their interface to ensure continuity of velocity and stress.

If the thin-gap assumption is relaxed, i.e.  $\delta^2 \gtrsim 1$ , the flow field is no longer governed by lubrication theory, and the full Stokes equations must be solved. While this might appear tractable, the validity

of assuming that the interface remains axisymmetric throughout the oscillatory deformation—even under small strain amplitudes—is questionable. Moreover, even if axisymmetry were preserved, the increased substrate separation introduces new challenges: the true bulk rheological stresses of the droplet (as opposed to those arising from lubrication pressure in the thin-gap case) and the bulk viscous stresses of the ambient Newtonian fluid both enter the interfacial stress balance (3.14) at leading dynamic order.

These stresses then compete among themselves and with the leading dynamic curvature stresses to determine the droplet deformation and interface shape. Consequently, the force response is also modified, and it is unclear whether the bulk rheology and interfacial tension can still be decoupled from this response. Wingstrand et al. [58] introduced corrections for enhanced substrate separations, but their analysis is restricted to macroscopic viscoelastic droplets (or thin films) where  $\text{Ca} \gg 1$  and  $\text{Ec} \gg 1$ , rendering a similar perturbative treatment of the interface unnecessary beyond enforcing the zero-pressure boundary condition (3.16) at each order of correction.

We also briefly remark that the Maxwell constitutive relation, used here to model the bulk behaviour of the viscoelastic microdroplet, is valid only at the leading dynamic order under the small strain amplitude assumption. Once this assumption is relaxed ( $\varepsilon \gtrsim 1$ ), the Maxwell model breaks down, and the full nonlinear Oldroyd-B model [34] must instead be employed to describe the bulk behaviour. In this regime, analytical treatments are no longer feasible, and one must resort to numerical simulations or experiments to track the droplet dynamics, as has already been explored in the  $\text{Ca} \gg 1$  and  $\text{Ec} \gg 1$  regime by multiple studies [45, 57, 137].

Finally, the present analytical framework requires validation through numerical simulations and/or experiments. For numerical validation, a two-dimensional axisymmetric finite element method (FEM) solution of the incompressible Stokes equations within the viscoelastic droplet and ambient Newtonian fluid is sufficient, coupled with a deforming interface of constant interfacial tension [151, 152]. At the interface, the normal and tangential stress balances, the kinematic boundary condition, and continuity of velocity must all be enforced. This setup can be implemented in COMSOL Multiphysics or Ansys using an arbitrary Lagrangian–Eulerian (ALE) moving-mesh formulation with curvature (interfacial tension) forces applied at the interface [13, 153–155].

The droplet bulk behaviour may be represented using the Maxwell model available in COMSOL’s Microfluidics Module (Non-Newtonian Flow) or in Ansys Polyflow/Fluent. No-slip and no-penetration conditions should be imposed on both substrates, with the lower substrate fixed and the upper substrate executing a prescribed small-amplitude oscillatory motion. The initial droplet shape is taken to be a rectangle (i.e. a cylinder in three dimensions) with a small aspect ratio (reflecting the thin gap between the substrates), and the contact lines at the rims are pinned. The force response then follows from integrating the traction on the lower substrate and can be compared directly with the prediction of the present analytical framework. By progressively increasing the gap from the thin-gap limit to  $\mathcal{O}(1)$ , such simulations can also be used to estimate the aspect ratio  $\delta$  at which the theory ceases to remain valid.

For experimental validation, the CCFA can be employed to generate clean-interface (surfactant-free) microdroplets of viscoelastic fluids whose interfacial tension with the selected ambient fluid (typically water) and storage and loss moduli are already reported in the literature. Such a droplet should be pinned between the rigid and cantilevered capillaries of equal inner radius in the CCFA, with the contact lines fixed, and the capillaries adjusted so that the initial configuration is cylindrical with a small gap, ensuring the aspect ratio  $\delta \ll 1$ . Small-strain oscillations can then be applied to the rigid capillary over a frequency sweep restricted to sufficiently low frequencies such that the elasto-capillary and capillary numbers remain small ( $\text{Ec} \ll 1$  and  $\text{Ca} \ll 1$ ).

The resulting oscillatory force response on the cantilevered capillary should be recorded as a function of time and compared directly with the predictions of the analytical framework. As with

the numerical simulations, progressively increasing the gap from the thin-gap limit to  $\mathcal{O}(1)$  and repeating the experiments will provide an estimate of the aspect ratio  $\delta$  at which the theory ceases to remain valid. Following successful validation with several well-characterized viscoelastic micro-droplets, the CCFA may then be employed to determine both the interfacial tension and bulk rheology of previously uncharacterized systems.

## 3.5 Conclusions

### 3.5.1 Key findings

In this chapter, we developed an analytical framework to describe the oscillatory deformation of a viscoelastic microdroplet, initially pinned at a contact angle of  $\pi/2$  between two closely spaced coaxial circular substrates, with small-amplitude oscillations imposed on the upper substrate. The flow field within the droplet was modeled using a regular perturbation expansion in the small strain amplitude ( $\varepsilon \ll 1$ ) and small aspect ratio ( $\delta^2 \ll 1$ ), with the droplet's bulk rheology described by the Maxwell model for the leading-order deviatoric stress. The flow field in the surrounding Newtonian fluid was similarly treated via a regular perturbation expansion in the small strain amplitude.

Due to the thin-gap geometry and small-amplitude deformations about the cylindrical base state, the interface slopes remain small, and the leading-order post-transient velocity field within the droplet is governed entirely by the oscillatory motion of the upper substrate. In this regime, viscous stresses from the ambient Newtonian fluid do not influence the dynamics at leading order. The radial component of the velocity field drives the evolution of the droplet interface shape via the kinematic boundary condition, leading to a parabolic interface shape that oscillates in phase with the imposed strain. This evolving shape, in turn, feeds back into the lubrication pressure as an in-phase response from the deforming interface, captured through the interfacial stress balance. In addition to this interfacial response, the pressure field contains in-phase components from the bulk elastic stresses and out-of-phase components from the bulk viscous stresses, all of which combine linearly.

Consequently, the leading-order force response consists of a static component—arising from Laplace pressure and contact line tension—and a dynamic component composed of linear in-phase contributions from the interfacial curvature and bulk elasticity, and an out-of-phase contribution from the bulk viscosity. In the limit of negligible bulk elasticity, i.e., small elasto-capillary number  $Ec \rightarrow 0$ , the model reduces to the force response derived by Barakat et al. [13] for a weakly viscous Newtonian droplet (or film) undergoing oscillatory squeeze flow in a thin-gap configuration, where interfacial stresses remain significant and the capillary number satisfies  $Ca \lesssim 1$ . Conversely, when the storage and loss moduli are sufficiently large such that  $Ec \gg 1$  and  $Ca \gg 1$ , the model asymptotically recovers the classical squeeze-flow response of a viscoelastic thin film [37, 55, 58], wherein interfacial contributions are negligible at leading order.

We also demonstrate that the resulting force response assumes the form of a phase-shifted sinusoidal signal with a time-independent offset. The offset provides a direct estimate of the interfacial tension  $\gamma$ , which, when combined with the amplitude and phase lag of the signal (relative to the imposed strain), enables the extraction of the frequency-dependent storage and loss moduli,  $G'(\omega)$  and  $G''(\omega)$ . Accordingly, if the force response of a viscoelastic microdroplet is measured using the CCFA, its intrinsic bulk material properties—the zero-shear viscosity  $\mu_0$ , infinite-frequency modulus  $G_0$ , and relaxation time  $\lambda = \mu_0/G_0$ —can be inferred. The present analytical framework thus offers the first simple yet robust method for extracting both the bulk rheology and interfacial tension of a viscoelastic microdroplet solely from its oscillatory force response.

In contrast to previous theories of thin-film oscillatory squeeze flow [37, 55, 58, 59], which ne-

glected interfacial effects by operating in the asymptotic regime  $\text{Ca} \gg 1$  and  $\text{Ec} \gg 1$ , the present model explicitly accounts for the significant role of interfacial stresses that are dominant over or comparable to bulk rheological stresses at the micron scale, i.e., when  $\text{Ca} \lesssim 1$  and  $\text{Ec} \lesssim 1$ . As such, applying these earlier models to microdroplets would result in significant errors in estimating the bulk rheological properties, underscoring the necessity of the present framework for accurate characterization of single viscoelastic microdroplets. Moreover, since the present theory remains valid across the entire range of capillary and elasto-capillary numbers, it is not limited to viscoelastic microdroplets alone. It may also be employed more broadly to characterize the material properties of macroscale viscoelastic droplets (or films) subjected to thin-gap, small-amplitude oscillatory squeeze flow, in macroscopic rheometers such as the OSFR and those that can be made to operate on the same principle [13, 37], including the compressional rheometer [39, 40], MFR [45], and FiSER [46].

### 3.5.2 Future directions

A primary direction of current interest is to investigate how the force response changes when the viscoelastic microdroplet is replaced by an incompressible viscoelastic solid microparticle. In this setting, the particle's momentum conservation is governed by the Newton–Cauchy equations [156–158], and the leading-order deviatoric stress is described by the Kelvin–Voigt model [34]. While numerical investigations of axisymmetric Kelvin–Voigt soft solids under thin-gap oscillatory deformation have been carried out for macroscopic slices [145], the applicability of such models to viscoelastic microparticles remains largely unexplored.

In particular, it is not evident how the solid–fluid interface behaves at the microscale, nor whether the classical interfacial stress balance employed in fluid–fluid systems holds in this regime. Even in the static limit, it is unclear whether a Young–Laplace-like equation governs the interface shape, since, unlike static fluids, the equilibrium configuration of a soft solid retains internal (bulk) elastic stresses in addition to interfacial tension forces. Recent developments in the field of elastocapillarity, which incorporate solid interfacial tension (also referred to as solid interfacial stress) into continuum descriptions of deformable solids [159–162], may offer a promising path toward formulating appropriate interfacial boundary conditions for such systems.

Another related extension of interest is to examine whether the present framework can be adapted to extract the material properties of microgels, which consist of a crosslinked viscoelastic polymer network permeated by a solvent. Owing to this dual-phase structure, microgels are expected to exhibit either a viscoelastic response—if the network relaxes quickly and the solvent drains rapidly—or a poroviscoelastic response—if solvent drainage and network relaxation occur on comparable time scales [91, 163, 164].

A final, and perhaps most natural, extension is to investigate how surfactant loading at the droplet–ambient fluid interface modifies the interface shape and, in turn, the force response under oscillatory deformation. In such systems, the local interfacial tension  $\gamma$  depends on the local surfactant surface concentration  $\Gamma$  and thus varies both spatially and temporally as the droplet is displaced from its initial configuration. Moreover, the surfactant monolayer may introduce additional interfacial rheology—including surface shear and dilatational viscosity and elasticity—depending on the surfactant type [15, 72, 97, 161].

Although interfacial effects in surfactant-laden systems have been extensively studied, either at isolated fluid–fluid interfaces or in capillary bridges subjected to large-strain deformations [14, 15, 72, 97–99, 165], there is, to our knowledge, no prior work addressing the oscillatory deformation of a surfactant-laden viscoelastic microdroplet in the OSFR configuration. In particular, it remains unclear how surfactant redistribution during oscillatory deformation generates surface concentration gradients, drives Marangoni flows, alters the spatiotemporal distribution of interfacial tension, in-

troduces surface rheology, and ultimately influences the measured force response. Whether the bulk rheology and interfacial tension can still be accurately extracted from such a modified response—and what additional complexities arise in doing so—remains an open question.

# Chapter 4

## Conclusions

In this thesis, we have developed two complementary analytical frameworks to capture the behaviour of axisymmetric microdroplets of size  $10\text{--}1000\,\mu\text{m}$  pinned between two coaxial circular substrates of equal radius, as they depart from a chosen initial configuration under small imposed strains. At this micron length scale, gravitational and inertial effects are negligible in both the droplet and the surrounding (Newtonian) fluid, owing to the small Bond number ( $\text{Bo} \ll 1$ ) and Reynolds numbers ( $\{\text{Re}, \text{Re}_a\} \ll 1$ ). In addition, curvature-induced capillary stresses are comparable to, or dominant over, bulk viscous and elastic stresses, since the relevant capillary and elasto-capillary numbers satisfy  $\text{Ca} \lesssim 1$  and  $\text{Ec} \lesssim 1$ .

Consequently, unlike macroscopic droplets of size  $\sim 1\text{--}10\,\text{mm}$ , which typically operate in the  $\text{Ca} \gg 1$  and  $\text{Ec} \gg 1$  limit, the measured force response here receives a significant contribution from interfacial tension in addition to bulk rheology. If this force response—which typically lies in the sensitive range  $1\,\text{nN}\text{--}1\,\text{mN}$ —can be reliably measured, it offers a powerful means to directly probe the material properties of the droplet, namely its interfacial tension and bulk rheology, together with its evolving bulk and interfacial deformation dynamics. The central challenge, however, is whether such delicate force responses can indeed be measured with sufficient accuracy.

This challenge is addressed by the cantilevered capillary force apparatus (CCFA) introduced by Frostad et al. [1], which is, at present, the only known instrument capable of measuring with high accuracy the force response of a broad range of soft microparticles, including microdroplets. However, the absence of a theoretical framework to interpret, analyze, and extract material properties from these measurements has limited its application as a tensiometer and rheometer. This thesis fills that gap. In Chapter 2, we extended the work of Kusumaatmaja and Lipowsky [2] by developing a second-order asymptotic model that captures both the linear and leading-order nonlinear force–displacement relationship, together with the evolving shape of a pinned, axisymmetric Newtonian microdroplet under quasi-static deformation from its initial (spherical, zero-force) state when the substrates are displaced by equal and opposite small strains. Here, the force response recorded by the CCFA serves as a means of measuring the droplet interfacial tension.

In Chapter 3, we built on prior studies of macroscopic viscoelastic droplets where interfacial effects are negligible [58], and of macroscopic Newtonian droplets where interfacial effects are significant [13], to develop an asymptotic model for the leading-order dynamics of a small-amplitude, thin-gap oscillatory squeezing of an initially cylindrical, pinned, axisymmetric viscoelastic microdroplet. In this configuration, the upper substrate is oscillated while the lower remains fixed, and the droplet bulk behaviour at leading dynamic order is described by the Maxwell linear viscoelastic constitutive equation. We outlined a procedure for simultaneously extracting both the bulk rheology and interfacial tension from the post-transient force response measured using the CCFA when operated in the manner of the oscillatory squeeze flow rheometer (OSFR).

Together, these analytical models elucidate the coupling between bulk rheological stresses within the deforming droplet and curvature-induced stresses at its evolving interface with the ambient Newtonian medium, and how this interplay governs both the droplet shape and the net force transmitted to the substrates under different types of strain. In doing so, they provide simple inversion formulae for extracting the droplet’s material properties directly from the measured force response, in a manner aligned with the measurement capabilities of the CCFA. This, in turn, enables the instrument to function as both a tensiometer and a rheometer, as required. In short, these models establish a practical route to characterizing the material properties of individual microdroplets, thereby enriching our understanding of multiphase systems composed of such droplets—ranging from food emulsions and cosmetics to drug-delivery vehicles and stimuli-responsive soft materials. The remainder of this chapter summarizes the key findings in Section 4.1, outlines the limitations of the present models in Section 4.2, and proposes avenues for future research in Section 4.3.

## 4.1 Key findings

First, in Chapter 2, we considered small imposed compressions and dilations of a pinned Newtonian microdroplet, which enabled us to derive second-order regular asymptotic expansions (in the small dimensionless displacement of the capillaries from the undeformed state) for both the force response and the droplet shape about its undeformed (spherical, zero-force) state. Since the system is allowed to relax to mechanical equilibrium at each deformation, the resulting force response is devoid of bulk viscous stresses and is governed solely by the static Laplace pressure and contact line tension. Corrections at successive orders are obtained through shape-mediated boundary conditions at the contact rims and a global volume conservation constraint, and depend only on the undeformed pinning angle  $\theta_0$ .

Here, the first-order corrections predominantly set the magnitude of each quantity and may therefore be interpreted as a “magnitude mode.” The second-order coefficients govern the asymmetry between compression and dilation, introducing nonlinear effects, and may thus be viewed as a “deformation-type mode.” Together, these corrections capture the key physical trend that the incremental force required to displace a droplet between successive equilibrium states increases under compression and decreases under dilation, with this incremental force at each displacement step growing with capillary radius. We also find that the accuracy of the asymptotic expansions depends systematically on the capillary radius.

Thus, by specifying  $\theta_0$  (or equivalently, the capillary-to-droplet radius ratio  $R/R_d = \sin \theta_0$ ), one can compute the evolving force response, mean curvature, pinning angle, and droplet shape at any prescribed displacement well into the leading-order nonlinear regime—without solving the full Young–Laplace equation numerically at each step. While numerical solutions remain feasible, they are cumbersome for routine validation and analysis of CCFA experiments. In this respect, the present work provides the first analytical model that extends substantially beyond the linear force–displacement regime studied by Kusumaatmaja and Lipowsky [2] and the weak Taylor-expansion-based quadratic correction proposed by Sariola [3]. In doing so, it furnishes a practical and efficient tool for experimentalists interpreting quasi-static microdroplet deformation data in the CCFA, and more broadly for analyzing pinned, axisymmetric Newtonian capillary bridges undergoing quasi-static deformation in natural or industrial contexts.

Next, in Chapter 3, we showed that owing to the thin-gap geometry and small-amplitude oscillations about the cylindrical base state of the viscoelastic microdroplet, the interface slopes remain small, and the leading-order (in  $\delta^2 \ll 1$  and  $\varepsilon \ll 1$ ) post-transient velocity field within the droplet is governed entirely by the oscillatory motion of the upper substrate. In this regime, viscous stresses

from the surrounding Newtonian fluid do not contribute at leading order. The radial component of the velocity field drives the evolution of the droplet interface via the kinematic boundary condition, producing a parabolic interface that oscillates in phase with the imposed strain. This evolving shape, in turn, feeds back into the lubrication pressure as an in-phase contribution from the deforming interface, captured through the interfacial stress balance. Alongside this interfacial response, the pressure field also contains in-phase contributions from bulk elastic stresses and out-of-phase contributions from bulk viscous stresses, all of which superpose linearly.

Consequently, the leading-order force response consists of a static component—arising from Laplace pressure and contact line tension—together with a dynamic component composed of linear in-phase contributions from interfacial curvature and bulk elasticity, and an out-of-phase contribution from the bulk viscosity. In contrast to previous theories of thin-film oscillatory squeeze flow [37, 55, 58, 59], which neglected interfacial effects by assuming the asymptotic regime  $\text{Ca} \gg 1$  and  $\text{Ec} \gg 1$ , the present model explicitly accounts for the significant role of interfacial stresses that are comparable to, or dominant over, bulk rheological stresses at the micron scale, i.e. when  $\text{Ca} \lesssim 1$  and  $\text{Ec} \lesssim 1$ .

This resulting force response assumes the form of a phase-shifted sinusoidal signal with a time-independent offset. The offset provides a direct estimate of the interfacial tension  $\gamma$ , which, when combined with the amplitude and phase lag of the signal (relative to the imposed strain), enables the extraction of the frequency-dependent storage and loss moduli,  $G'(\omega)$  and  $G''(\omega)$ . Accordingly, if the force response of a viscoelastic microdroplet is measured using the CCFA, its intrinsic bulk material properties—the zero-shear viscosity  $\mu_0$ , infinite-frequency modulus  $G_0$ , and relaxation time  $\lambda = \mu_0/G_0$ —can be inferred. The present analytical framework thus provides the first simple yet robust method for simultaneously extracting the bulk rheology and interfacial tension of a viscoelastic microdroplet solely from its oscillatory force response.

## 4.2 Limitations

The analytical models developed in Chapters 2 and 3 share several limitations that arise directly from the assumptions underlying their formulation. First, they are restricted to small-strain displacements of the substrates (or capillaries) and assume that the droplet remains axisymmetric throughout its deformation. As a result, their accuracy degrades under relatively large imposed displacements or once axisymmetry is broken beyond a critical deformation, as analyzed by Elfring and Lauga [127].

For droplets of typical size 10–100  $\mu\text{m}$ , the Bond number  $\text{Bo} \ll 1$  and Reynolds number  $\text{Re} \ll 1$ , so gravitational and inertial effects are neglected. This implies that before applying these theories to macroscopic droplets—by simply altering the regimes of the capillary and elasto-capillary numbers—gravitational effects must be incorporated. Likewise, before applying them to high-frequency oscillatory systems, inertial contributions must be included. Both gravitational and inertial effects have been examined extensively in prior studies [37, 56, 166–168].

We further assumed that the bounding substrates are rigid and do not deform in response to the droplet forces—an assumption that omits soft (elastic) substrate effects considered by Wexler et al. [169]—and that the droplet contact lines remain pinned throughout the deformation, thereby excluding advancing or receding motion (contact line hysteresis) as investigated by De Souza et al. [170] and Chen et al. [171]. Further, to capture the essential physics, the models were restricted to circular substrates of equal radius. Leading-order geometric asymmetry in the quasi-static force response of Newtonian droplets due to unequal substrate radii has been examined by Kusumaatmaja and Lipowsky [2] and Sariola [3], though such effects do not qualitatively alter the dominant physical trends.

Related studies of squeeze flow in other geometries, such as sphere–sphere [143] and sphere–plane [144] configurations, have also been carried out, but their extension to oscillatory flows remains unexplored; however, no qualitative changes in the key trends identified here are anticipated. The substrates are additionally assumed to be smooth, which is generally not the case in most experiments. The influence of surface roughness in related contexts has been explored in detail by Meeten [172].

Furthermore, the droplet–ambient interface in both models is assumed to be clean, with constant interfacial tension and no Marangoni stresses arising from surfactant concentration gradients. This excludes interfacial effects on the force response and droplet shape that can arise in surfactant-laden systems, which have been extensively investigated in related contexts [97–99, 149, 165]. The droplets in both models are also assumed to maintain a fixed volume and remain in thermal equilibrium with the ambient fluid, so that evaporation or mass transfer with the surrounding medium is absent—phenomena explored in earlier works [173, 174]. In addition, although the analytical framework developed in Chapter 2 has been validated against RK45 shooting solutions, experimental validation using the CCFA remains lacking and is required for completeness. For the framework in Chapter 3, this limitation is even more pronounced, as it has not yet been validated either numerically (via FEM simulations) or experimentally using the CCFA, leaving the accuracy of this model still uncertain.

We now highlight some specific limitations of each model (more detailed discussions are provided in the Conclusions sections of the respective chapters), beginning with that developed in Chapter 2. This framework assumes that the relative change in droplet bridge volume remains below 5%—for both pinned droplets and those held at the capillary rims by constant suction pressure—across the range of capillary radii and suction pressures typically used in the CCFA (see Appendix B). Accordingly, the bridge volume is approximated as constant.

However, when larger capillary radii or suction pressures are employed, this approximation progressively breaks down owing to increased volume exchange between the bridge and the spherical caps confined within the capillaries. In such cases, the correct constraint to enforce, provided there is no mass exchange with the ambient fluid, is that the total droplet volume (i.e. the sum of the bridge volume and the cap volumes) remains constant. Consequently, the first- and second-order coefficients of the force response, mean curvature, pinning angle, and droplet shape will differ from those reported in the chapter, although the underlying perturbative methodology for their derivation remains unchanged.

We now turn to the analytical framework developed in Chapter 3. In addition to assuming small strain amplitudes ( $\varepsilon \ll 1$ ), this model requires that the gap between the substrates is sufficiently thin ( $\delta^2 \ll 1$ ) and that the droplet oscillates about an initially cylindrical base state. Under these assumptions, interface slopes remain small and a lubrication flow field is valid across the droplet, such that the leading-order dynamic interface shape is governed by the radial velocity component.

However, the framework becomes questionable when the initial pinning angle takes obtuse values that deviate significantly from  $\pi/2$ . In such cases, even for small strain amplitudes and thin gaps, the droplet may bulge substantially outside the thin-gap region, violating the small-slope approximation. It is then unclear whether the lubrication flow in the thin-gap region continues to dictate the interface shape or whether a distinct Stokes flow field develops in the bulged-out region.

We also remark that the Maxwell constitutive relation, used here to model the bulk behaviour of the viscoelastic microdroplet, is valid only at the leading dynamic order under the small strain amplitude assumption. Once this assumption is relaxed ( $\varepsilon \gtrsim 1$ ), the Maxwell model ceases to provide an accurate description, and the full nonlinear Oldroyd-B model [34] must instead be employed. In this regime, analytical treatments are no longer feasible, and one must resort to numerical (FEM) simulations or experiments to resolve the droplet dynamics, as has already been explored in the  $\text{Ca} \gg 1$  and  $\text{Ec} \gg 1$  limits by multiple studies [45, 57, 137].

### 4.3 Future directions

A natural and perhaps most immediate extension of the analytical models developed in Chapters 2 and 3 is to examine how the droplet shape, force response, and overall dynamics are modified when the droplet–ambient interface is laden with surfactants. In such systems, the local interfacial tension  $\gamma$  depends on the local surfactant surface concentration  $\Gamma$ , and therefore varies both spatially and temporally as the droplet is displaced from its chosen initial configuration. Moreover, the presence of a surfactant monolayer may introduce additional interfacial rheology—including surface shear and dilatational viscosity and elasticity—depending on the surfactant type [15, 72, 97, 161]. These effects are expected to contribute additional terms to the measured force response. It remains an open and compelling question whether, and under what conditions, one can disentangle the coupled contributions of bulk rheology, interfacial tension, and interfacial rheology from the force response, and what new complexities may arise in attempting to do so.

A second direction follows from the validation limitations highlighted in the previous section. Although the analytical framework developed in Chapter 2 has been validated against RK45 shooting solutions, experimental validation using the CCFA remains essential for completeness. Likewise, for the framework in Chapter 3, validation should involve CCFA experiments on viscoelastic microdroplets whose interfacial tension with the chosen ambient fluid (typically water) and storage and loss moduli are already reported in the literature. Once validated, the framework can then be employed to determine both the interfacial tension and bulk rheology of previously uncharacterized systems.

Numerical validation is also required (and is planned next), entailing a two-dimensional axisymmetric finite element method (FEM) solution of the incompressible Stokes equations within the viscoelastic droplet and surrounding Newtonian fluid, coupled with a deforming interface of constant interfacial tension [151, 152]. Such a setup may be implemented in COMSOL Multiphysics or Ansys using an arbitrary Lagrangian–Eulerian (ALE) moving-mesh formulation with curvature (surface-tension) forces applied at the interface [13, 153–155]. The droplet bulk behaviour may be represented using the Maxwell model available in COMSOL’s Microfluidics Module (Non-Newtonian Flow) or in Ansys Polyflow/Fluent.

A further direction, specific to Chapter 3, is to investigate how the oscillatory force response is altered when the viscoelastic microdroplet is replaced by an incompressible viscoelastic solid microparticle. Numerical studies of axisymmetric Kelvin–Voigt solids subjected to thin-gap oscillatory deformation have been reported for macroscopic slices [145], but the relevance of such models at the microscale remains largely unexplored. In particular, it is not evident how the solid–fluid interface behaves at the microscale, nor whether the classical interfacial stress balance employed in fluid–fluid systems holds in this regime.

Recent developments in the field of elastocapillarity, which incorporate solid interfacial tension (also referred to as solid interfacial stress) into continuum descriptions of deformable solids [159–162], may offer a promising path toward formulating appropriate interfacial boundary conditions for such systems. A related extension of particular interest is to examine whether the present framework can be adapted to extract material properties of microparticles with more complex bulk rheology, such as microgels. These systems, consisting of a crosslinked viscoelastic polymer network permeated by solvent, exhibit poroviscoelastic responses that depend on the relative timescales of network relaxation and solvent drainage [91, 163, 164].

# Bibliography

- [1] John M. Frostad, Martha C. Collins, and L. Gary Leal. Cantilevered-capillary force apparatus for measuring multiphase fluid interactions. *Langmuir*, 29(15):4715–4725, April 2013. ISSN 1520-5827. doi: 10.1021/la304115k. URL <http://dx.doi.org/10.1021/la304115k>.
- [2] Halim Kusumaatmaja and Reinhard Lipowsky. Equilibrium morphologies and effective spring constants of capillary bridges. *Langmuir*, 26(24):18734–18741, December 2010. ISSN 1520-5827. doi: 10.1021/la102206d. URL <http://dx.doi.org/10.1021/la102206d>.
- [3] Veikko Sariola. Analytical expressions for spring constants of capillary bridges and snap-in forces of hydrophobic surfaces. *Langmuir*, 35(22):7129–7135, April 2019. ISSN 1520-5827. doi: 10.1021/acs.langmuir.9b00152. URL <http://dx.doi.org/10.1021/acs.langmuir.9b00152>.
- [4] Christos N. Likos. Soft matter with soft particles. *Soft Matter*, 2(6):478, 2006. ISSN 1744-6848. doi: 10.1039/b601916c. URL <http://dx.doi.org/10.1039/b601916c>.
- [5] Eunseo Kim and Hyomin Lee. Mechanical characterization of soft microparticles prepared by droplet microfluidics. *Journal of Polymer Science*, 60(11):1670–1699, April 2022. ISSN 2642-4169. doi: 10.1002/pol.20220110. URL <http://dx.doi.org/10.1002/pol.20220110>.
- [6] Pei-Hsun Wu, Dikla Raz-Ben Aroush, Atef Asnacios, Wei-Chiang Chen, Maxim E. Dokukin, Bryant L. Doss, Pauline Durand-Smet, Andrew Ekpenyong, Jochen Guck, Natalia V. Guz, Paul A. Janmey, Jerry S. H. Lee, Nicole M. Moore, Albrecht Ott, Yeh-Chuin Poh, Robert Ros, Mathias Sander, Igor Sokolov, Jack R. Staunton, Ning Wang, Graeme Whyte, and Denis Wirtz. A comparison of methods to assess cell mechanical properties. *Nature Methods*, 15(7):491–498, June 2018. ISSN 1548-7105. doi: 10.1038/s41592-018-0015-1. URL <http://dx.doi.org/10.1038/s41592-018-0015-1>.
- [7] Adnan Morshed, Buddini Iroshika Karawdeniya, Y.M. Nuwan D.Y. Bandara, Min Jun Kim, and Prashanta Dutta. Mechanical characterization of vesicles and cells: A review. *Electrophoresis*, 41(7–8):449–470, February 2020. ISSN 1522-2683. doi: 10.1002/elps.201900362. URL <http://dx.doi.org/10.1002/elps.201900362>.
- [8] Alexander Kumachev, Ethan Tumarkin, Gilbert C. Walker, and Eugenia Kumacheva. Characterization of the mechanical properties of microgels acting as cellular microenvironments. *Soft Matter*, 9(10):2959, 2013. ISSN 1744-6848. doi: 10.1039/c3sm27400d. URL <http://dx.doi.org/10.1039/c3sm27400d>.
- [9] David Julian McClements. *Food Emulsions: Principles, Practices, and Techniques, Third Edition*. CRC Press, August 2015. ISBN 9780429154034. doi: 10.1201/b18868. URL <http://dx.doi.org/10.1201/b18868>.

- [10] R. Brummer. *Rheology Essentials of Cosmetic and Food Emulsions*. Springer Laboratory. Springer Berlin Heidelberg, 2006. ISBN 9783540290872. URL [https://books.google.ca/books?id=H\\_6-BTTXr38C](https://books.google.ca/books?id=H_6-BTTXr38C).
- [11] Saeed Saber-Samandari, Kadhim Alamara, and Samaneh Saber-Samandari. Calcium phosphate coatings: Morphology, micro-structure and mechanical properties. *Ceramics International*, 40(1):563–572, January 2014. ISSN 0272-8842. doi: 10.1016/j.ceramint.2013.06.038. URL <http://dx.doi.org/10.1016/j.ceramint.2013.06.038>.
- [12] Detlef Lohse. Fundamental fluid dynamics challenges in inkjet printing. *Annual Review of Fluid Mechanics*, 54(1):349–382, January 2022. ISSN 1545-4479. doi: 10.1146/annurev-fluid-022321-114001. URL <http://dx.doi.org/10.1146/annurev-fluid-022321-114001>.
- [13] J. M. Barakat, Z. Hinton, N. J. Alvarez, and T. W. Walker. Surface-tension effects in oscillatory squeeze flow rheometry. *Physics of Fluids*, 33(12), December 2021. ISSN 1089-7666. doi: 10.1063/5.0072869. URL <http://dx.doi.org/10.1063/5.0072869>.
- [14] José M. Montanero and Alberto Ponce-Torres. Review on the dynamics of isothermal liquid bridges. *Applied Mechanics Reviews*, 72(1), October 2019. ISSN 2379-0407. doi: 10.1115/1.4044467. URL <http://dx.doi.org/10.1115/1.4044467>.
- [15] Harishankar Manikantan and Todd M. Squires. Surfactant dynamics: hidden variables controlling fluid flows. *Journal of Fluid Mechanics*, 892, April 2020. ISSN 1469-7645. doi: 10.1017/jfm.2020.170. URL <http://dx.doi.org/10.1017/jfm.2020.170>.
- [16] John C. Slattery. *Interfacial Transport Phenomena*. Springer New York, 1990. ISBN 9781475720907. doi: 10.1007/978-1-4757-2090-7. URL <http://dx.doi.org/10.1007/978-1-4757-2090-7>.
- [17] Pierre-Gilles de Gennes, Françoise Brochard-Wyart, and David Quéré. *Capillarity and Wetting Phenomena*. Springer New York, 2004. ISBN 9780387216560. doi: 10.1007/978-0-387-21656-0. URL <http://dx.doi.org/10.1007/978-0-387-21656-0>.
- [18] Jean Berthier, Kenneth A Brakke, et al. *The physics of microdroplets*. Wiley Online Library, 2012. URL <https://onlinelibrary.wiley.com/doi/abs/10.1002/9781118401323>.
- [19] E. Evans, K. Ritchie, and R. Merkel. Sensitive force technique to probe molecular adhesion and structural linkages at biological interfaces. *Biophysical Journal*, 68(6):2580–2587, June 1995. ISSN 0006-3495. doi: 10.1016/s0006-3495(95)80441-8. URL [http://dx.doi.org/10.1016/s0006-3495\(95\)80441-8](http://dx.doi.org/10.1016/s0006-3495(95)80441-8).
- [20] K. Moran, A. Yeung, and J. Masliyah. Measuring interfacial tensions of micrometer-sized droplets: A novel micromechanical technique. *Langmuir*, 15(24):8497–8504, September 1999. ISSN 1520-5827. doi: 10.1021/la990363g. URL <http://dx.doi.org/10.1021/la990363g>.
- [21] Hans-Jürgen Butt, Brunero Cappella, and Michael Kappl. Force measurements with the atomic force microscope: Technique, interpretation and applications. *Surface Science Reports*, 59(1–6):1–152, October 2005. ISSN 0167-5729. doi: 10.1016/j.surfrept.2005.08.003. URL <http://dx.doi.org/10.1016/j.surfrept.2005.08.003>.

- [22] Hans M. Wyss, Thomas Franke, Elisa Mele, and David A. Weitz. Capillary micromechanics: Measuring the elasticity of microscopic soft objects. *Soft Matter*, 6(18):4550, 2010. ISSN 1744-6848. doi: 10.1039/c003344h. URL <http://dx.doi.org/10.1039/c003344h>.
- [23] Adam R. Abate, Lloyd Han, Lihua Jin, Zhigang Suo, and David A. Weitz. Measuring the elastic modulus of microgels using microdrops. *Soft Matter*, 8(39):10032, 2012. ISSN 1744-6848. doi: 10.1039/c2sm26108a. URL <http://dx.doi.org/10.1039/c2sm26108a>.
- [24] Blanca González-Bermúdez, Gustavo V. Guinea, and Gustavo R. Plaza. Advances in micropipette aspiration: Applications in cell biomechanics, models, and extended studies. *Bioophysical Journal*, 116(4):587–594, February 2019. ISSN 0006-3495. doi: 10.1016/j.bpj.2019.01.004. URL <http://dx.doi.org/10.1016/j.bpj.2019.01.004>.
- [25] Yun-Han Huang, Fleur Salmon, Abhijeet Kamble, April Xu Xu, Mariano Michelon, Bruna C. Leopercio, Marcio S. Carvalho, and John M. Frostad. Models for the mechanical characterization of core-shell microcapsules under uniaxial deformation. *Food Hydrocolloids*, 119:106762, October 2021. ISSN 0268-005X. doi: 10.1016/j.foodhyd.2021.106762. URL <http://dx.doi.org/10.1016/j.foodhyd.2021.106762>.
- [26] Achu Yango, Jens Schäpe, Carmela Rianna, Holger Doschke, and Manfred Radmacher. Measuring the viscoelastic creep of soft samples by step response afm. *Soft Matter*, 12(40):8297–8306, 2016. ISSN 1744-6848. doi: 10.1039/c6sm00801a. URL <http://dx.doi.org/10.1039/c6sm00801a>.
- [27] Kaili Xie and Marc Leonetti. Mechanical characterization of core-shell microcapsules. *Comptes Rendus. Mécanique*, 351(S2):163–182, November 2023. ISSN 1873-7234. doi: 10.5802/crmeca.148. URL <http://dx.doi.org/10.5802/crmeca.148>.
- [28] Kuo-Kang Liu. Deformation behaviour of soft particles: a review. *Journal of Physics D: Applied Physics*, 39(11):R189–R199, May 2006. ISSN 1361-6463. doi: 10.1088/0022-3727/39/11/r01. URL <http://dx.doi.org/10.1088/0022-3727/39/11/r01>.
- [29] L. Gary Leal. *Advanced Transport Phenomena: Fluid Mechanics and Convective Transport Processes*. Cambridge University Press, June 2007. ISBN 9780511800245. doi: 10.1017/cbo9780511800245. URL <http://dx.doi.org/10.1017/cbo9780511800245>.
- [30] Constantine Pozrikidis. *Fluid Dynamics: Theory, Computation, and Numerical Simulation*. Springer US, 2009. ISBN 9780387958712. doi: 10.1007/978-0-387-95871-2. URL <http://dx.doi.org/10.1007/978-0-387-95871-2>.
- [31] R.B. Bird. *Dynamics of Polymeric Liquids, Volume 1: Fluid Mechanics*. Dynamics of Polymeric Liquids. Wiley, 1987. ISBN 9780471802457. URL <https://books.google.ca/books?id=posvAQAAIAAJ>.
- [32] Dominique Barthes-Biesel. *Microhydrodynamics and Complex Fluids*. CRC Press, June 2012. ISBN 9781466566910. doi: 10.1201/b12147. URL <http://dx.doi.org/10.1201/b12147>.
- [33] Saverio E Spagnolie. *Complex Fluids in Biological Systems: Experiment, Theory, and Computation*. Springer New York, 2015. ISBN 9781493920655. doi: 10.1007/978-1-4939-2065-5. URL <http://dx.doi.org/10.1007/978-1-4939-2065-5>.

- [34] Michael D. Graham. *Microhydrodynamics, Brownian Motion, and Complex Fluids*. Cambridge University Press, August 2018. ISBN 9781107695931. doi: 10.1017/9781139175876. URL <http://dx.doi.org/10.1017/9781139175876>.
- [35] P. G. de Gennes. Soft matter. *Science*, 256(5056):495–497, April 1992. ISSN 1095-9203. doi: 10.1126/science.256.5056.495. URL <http://dx.doi.org/10.1126/science.256.5056.495>.
- [36] R.G. Larson. *The Structure and Rheology of Complex Fluids*. Topics in Chemical Engineering. OUP USA, 1999. ISBN 9780195121971. URL [https://books.google.ca/books?id=Vt9fw\\_pf1LUC](https://books.google.ca/books?id=Vt9fw_pf1LUC).
- [37] D. Bell, D. M. Binding, and K. Walters. The oscillatory squeeze flow rheometer: comprehensive theory and a new experimental facility. *Rheologica Acta*, 46(1):111–121, May 2006. ISSN 1435-1528. doi: 10.1007/s00397-006-0097-z. URL <http://dx.doi.org/10.1007/s00397-006-0097-z>.
- [38] Sidney R. Nagel. Experimental soft-matter science. *Reviews of Modern Physics*, 89(2), April 2017. ISSN 1539-0756. doi: 10.1103/revmodphys.89.025002. URL <http://dx.doi.org/10.1103/revmodphys.89.025002>.
- [39] William E Van Arsdale and Hatim Motivala. Device for determining viscoelastic properties of liquids and a method for use, October 19 1993. US Patent 5,253,513.
- [40] PR Whittingstall and WE Van Arsdale. A compressional rheometer for viscoelastic fluids. In *Book of Abstracts of The 70th Annual Meeting of the Society of Rheology, Monterey CA*, 1998.
- [41] Reema H. Alasfar, Said Ahzi, Nicolas Barth, Viktor Kochkodan, Marwan Khraisheh, and Muammer Koç. A review on the modeling of the elastic modulus and yield stress of polymers and polymer nanocomposites: Effect of temperature, loading rate and porosity. *Polymers*, 14(3):360, January 2022. ISSN 2073-4360. doi: 10.3390/polym14030360. URL <http://dx.doi.org/10.3390/polym14030360>.
- [42] Karol Miller. Method of testing very soft biological tissues in compression. *Journal of Biomechanics*, 38(1):153–158, January 2005. ISSN 0021-9290. doi: 10.1016/j.jbiomech.2004.03.004. URL <http://dx.doi.org/10.1016/j.jbiomech.2004.03.004>.
- [43] Jyoti R. Seth, Michel Cloitre, and Roger T. Bonnecaze. Elastic properties of soft particle pastes. *Journal of Rheology*, 50(3):353–376, May 2006. ISSN 1520-8516. doi: 10.1122/1.2186982. URL <http://dx.doi.org/10.1122/1.2186982>.
- [44] Yu-Li Lin, Da-Ming Wang, Wei-Ming Lu, Yu-Shen Lin, and Kuo-Lun Tung. Compression and deformation of soft spherical particles. *Chemical Engineering Science*, 63(1):195–203, January 2008. ISSN 0009-2509. doi: 10.1016/j.ces.2007.09.028. URL <http://dx.doi.org/10.1016/j.ces.2007.09.028>.
- [45] J.S. Field, M.V. Swain, and N. Phan-Thien. An experimental investigation of the use of random squeezing to determine the complex modulus of viscoelastic fluids. *Journal of Non-Newtonian Fluid Mechanics*, 65(2–3):177–194, August 1996. ISSN 0377-0257. doi: 10.1016/0377-0257(96)01445-0. URL [http://dx.doi.org/10.1016/0377-0257\(96\)01445-0](http://dx.doi.org/10.1016/0377-0257(96)01445-0).
- [46] Gareth H. McKinley and Tamarapu Sridhar. Filament-stretching rheometry of complex fluids. *Annual Review of Fluid Mechanics*, 34(1):375–415, January 2002. ISSN 1545-4479. doi: 10.

- 1146/annurev.fluid.34.083001.125207. URL <http://dx.doi.org/10.1146/annurev.fluid.34.083001.125207>.
- [47] M. Stelter, G. Brenn, A. L. Yarin, R. P. Singh, and F. Durst. Validation and application of a novel elongational device for polymer solutions. *Journal of Rheology*, 44(3):595–616, May 2000. ISSN 1520-8516. doi: 10.1122/1.551102. URL <http://dx.doi.org/10.1122/1.551102>.
- [48] Shelley L. Anna and Gareth H. McKinley. Elasto-capillary thinning and breakup of model elastic liquids. *Journal of Rheology*, 45(1):115–138, January 2001. ISSN 1520-8516. doi: 10.1122/1.1332389. URL <http://dx.doi.org/10.1122/1.1332389>.
- [49] A. Gaillard, M. A. Herrada, A. Deblais, J. Eggers, and D. Bonn. Beware of caber: Filament thinning rheometry does not always give ‘the’ relaxation time of polymer solutions. *Physical Review Fluids*, 9(7), July 2024. ISSN 2469-990X. doi: 10.1103/physrevfluids.9.073302. URL <http://dx.doi.org/10.1103/physrevfluids.9.073302>.
- [50] Jianyi Du, Hiroko Ohtani, Kevin Ellwood, and Gareth H. McKinley. Capillarity-driven thinning and breakup of weakly rate-thickening fluids. *Journal of Non-Newtonian Fluid Mechanics*, 331:105294, September 2024. ISSN 0377-0257. doi: 10.1016/j.jnnfm.2024.105294. URL <http://dx.doi.org/10.1016/j.jnnfm.2024.105294>.
- [51] H.A. Barnes, J.F. Hutton, and K. Walters. *An Introduction to Rheology*. Rheology series. Elsevier, 1989. ISBN 9780720420104. URL <https://books.google.ca/books?id=k6n8PgAACAAJ>.
- [52] Howard A. Barnes. A review of the slip (wall depletion) of polymer solutions, emulsions and particle suspensions in viscometers: its cause, character, and cure. *Journal of Non-Newtonian Fluid Mechanics*, 56(3):221–251, March 1995. ISSN 0377-0257. doi: 10.1016/0377-0257(94)01282-m. URL [http://dx.doi.org/10.1016/0377-0257\(94\)01282-m](http://dx.doi.org/10.1016/0377-0257(94)01282-m).
- [53] Randy H. Ewoldt, Michael T. Johnston, and Lucas M. Caretta. *Experimental Challenges of Shear Rheology: How to Avoid Bad Data*, page 207–241. Springer New York, October 2014. ISBN 9781493920655. doi: 10.1007/978-1-4939-2065-5\_6. URL [http://dx.doi.org/10.1007/978-1-4939-2065-5\\_6](http://dx.doi.org/10.1007/978-1-4939-2065-5_6).
- [54] Beyza Büyükgurgancı, Santanu Kumar Basu, Markus Neuner, Jochen Guck, Andreas Wierschem, and Felix Reichel. Shear rheology of methyl cellulose based solutions for cell mechanical measurements at high shear rates. *Soft Matter*, 19(9):1739–1748, 2023. ISSN 1744-6848. doi: 10.1039/d2sm01515c. URL <http://dx.doi.org/10.1039/d2sm01515c>.
- [55] N. Phan-Thien. Small strain oscillatory squeeze film flow of simple fluids. *The Journal of the Australian Mathematical Society. Series B. Applied Mathematics*, 22(1):22–27, July 1980. ISSN 1839-4078. doi: 10.1017/s0334270000002514. URL <http://dx.doi.org/10.1017/s0334270000002514>.
- [56] Nhan Phan-Thien, John S. Field, and Michael V. Swain. Micro-fourier rheometer: Inertial effects. *Rheologica Acta*, 35(5):410–416, 1996. ISSN 1435-1528. doi: 10.1007/bf00368992. URL <http://dx.doi.org/10.1007/bf00368992>.
- [57] Benoît Debbaut and Ken Thomas. Simulation and analysis of oscillatory squeeze flow. *Journal of Non-Newtonian Fluid Mechanics*, 124(1–3):77–91, December 2004. ISSN 0377-0257. doi: 10.1016/j.jnnfm.2004.07.006. URL <http://dx.doi.org/10.1016/j.jnnfm.2004.07.006>.

- [58] Sara L. Wingstrand, Nicolas J. Alvarez, Ole Hassager, and John M. Dealy. Oscillatory squeeze flow for the study of linear viscoelastic behavior. *Journal of Rheology*, 60(3):407–418, May 2016. ISSN 1520-8516. doi: 10.1122/1.4943984. URL <http://dx.doi.org/10.1122/1.4943984>.
- [59] Rui Yang, Ivan C. Christov, Ian M. Griffiths, and Guy Z. Ramon. Time-averaged transport in oscillatory squeeze flow of a viscoelastic fluid. *Physical Review Fluids*, 5(9), September 2020. ISSN 2469-990X. doi: 10.1103/physrevfluids.5.094501. URL <http://dx.doi.org/10.1103/physrevfluids.5.094501>.
- [60] G. Mederos, O. Bautista, F. Méndez, and J. Arcos. Squeeze force of a maxwell fluid between circular smooth surfaces with simple harmonic motion. *Physics of Fluids*, 36(9), September 2024. ISSN 1089-7666. doi: 10.1063/5.0228832. URL <http://dx.doi.org/10.1063/5.0228832>.
- [61] Joseph D. Berry, Michael J. Neeson, Raymond R. Dagastine, Derek Y.C. Chan, and Rico F. Tabor. Measurement of surface and interfacial tension using pendant drop tensiometry. *Journal of Colloid and Interface Science*, 454:226–237, September 2015. ISSN 0021-9797. doi: 10.1016/j.jcis.2015.05.012. URL <http://dx.doi.org/10.1016/j.jcis.2015.05.012>.
- [62] Bruce Gash and D.R. Parrish. A simple spinning-drop interfacial tensiometer. *Journal of Petroleum Technology*, 29(01):30–31, January 1977. ISSN 1944-978X. doi: 10.2118/5987-pa. URL <http://dx.doi.org/10.2118/5987-pa>.
- [63] Y. Seeto and L. E. Scriven. Precision spinning drop interfacial tensiometer. *Review of Scientific Instruments*, 53(11):1757–1761, November 1982. ISSN 1089-7623. doi: 10.1063/1.1136893. URL <http://dx.doi.org/10.1063/1.1136893>.
- [64] O.H Soo-Gun and John C Slattery. Disk and biconical interfacial viscometers. *Journal of Colloid and Interface Science*, 67(3):516–525, December 1978. ISSN 0021-9797. doi: 10.1016/0021-9797(78)90242-4. URL [http://dx.doi.org/10.1016/0021-9797\(78\)90242-4](http://dx.doi.org/10.1016/0021-9797(78)90242-4).
- [65] Yia-Ching Ray, Hae Ok Lee, Tsung Leo Jiang, and Tsung-Shann Jiang. Oscillatory torsional interfacial viscometer. *Journal of Colloid and Interface Science*, 119(1):81–99, September 1987. ISSN 0021-9797. doi: 10.1016/0021-9797(87)90247-5. URL [http://dx.doi.org/10.1016/0021-9797\(87\)90247-5](http://dx.doi.org/10.1016/0021-9797(87)90247-5).
- [66] Hae Ok Lee, Tsung-Shann Jiang, and Kostas S Avramidis. Measurements of interfacial shear viscoelasticity with an oscillatory torsional viscometer. *Journal of Colloid and Interface Science*, 146(1):90–122, October 1991. ISSN 0021-9797. doi: 10.1016/0021-9797(91)90009-w. URL [http://dx.doi.org/10.1016/0021-9797\(91\)90009-w](http://dx.doi.org/10.1016/0021-9797(91)90009-w).
- [67] R. Nagarajan, S.I. Chung, and D.T. Wasan. Biconical bob oscillatory interfacial rheometer. *Journal of Colloid and Interface Science*, 204(1):53–60, August 1998. ISSN 0021-9797. doi: 10.1006/jcis.1998.5583. URL <http://dx.doi.org/10.1006/jcis.1998.5583>.
- [68] Sven Reynaert, Carlton F. Brooks, Paula Moldenaers, Jan Vermant, and Gerald G. Fuller. Analysis of the magnetic rod interfacial stress rheometer. *Journal of Rheology*, 52(1):261–285, January 2008. ISSN 1520-8516. doi: 10.1122/1.2798238. URL <http://dx.doi.org/10.1122/1.2798238>.
- [69] Yun-Han Huang and John M. Frostad. A new instrument for interfacial dilational rheology. *Review of Scientific Instruments*, 94(11), November 2023. ISSN 1089-7623. doi: 10.1063/5.0168137. URL <http://dx.doi.org/10.1063/5.0168137>.

- [70] Yun-Han Huang and John M. Frostad. Establishing physiologically relevant conditions for measuring the interfacial rheology of lung surfactants. *Soft Matter*, 21(31):6207–6219, 2025. ISSN 1744-6848. doi: 10.1039/d5sm00323g. URL <http://dx.doi.org/10.1039/d5sm00323g>.
- [71] Jaroslaw Drelich, Ch Fang, and CL White. Measurement of interfacial tension in fluid-fluid systems. *Encyclopedia of surface and colloid science*, 3:3158–3163, 2002. URL [https://www.academia.edu/download/43355891/Measurement\\_of\\_interfacial\\_tension\\_in\\_Fl20160304-7580-16cuc8r.pdf](https://www.academia.edu/download/43355891/Measurement_of_interfacial_tension_in_Fl20160304-7580-16cuc8r.pdf).
- [72] Gerald G. Fuller and Jan Vermant. Complex fluid-fluid interfaces: Rheology and structure. *Annual Review of Chemical and Biomolecular Engineering*, 3(1):519–543, July 2012. ISSN 1947-5446. doi: 10.1146/annurev-chembioeng-061010-114202. URL <http://dx.doi.org/10.1146/annurev-chembioeng-061010-114202>.
- [73] Leonard M.C. Sagis and Peter Fischer. Nonlinear rheology of complex fluid–fluid interfaces. *Current Opinion in Colloid & Interface Science*, 19(6):520–529, December 2014. ISSN 1359-0294. doi: 10.1016/j.cocis.2014.09.003. URL <http://dx.doi.org/10.1016/j.cocis.2014.09.003>.
- [74] Nick O. Jaensson, Patrick D. Anderson, and Jan Vermant. Computational interfacial rheology. *Journal of Non-Newtonian Fluid Mechanics*, 290:104507, April 2021. ISSN 0377-0257. doi: 10.1016/j.jnnfm.2021.104507. URL <http://dx.doi.org/10.1016/j.jnnfm.2021.104507>.
- [75] E. Evans, R. Merkel, K. Ritchie, S. Tha, and A. Zilker. *Picoforce Method to Probe Submicroscopic Actions in Biomembrane Adhesion*, page 125–139. Springer Berlin Heidelberg, 1994. ISBN 9783662030080. doi: 10.1007/978-3-662-03008-0\_9. URL [http://dx.doi.org/10.1007/978-3-662-03008-0\\_9](http://dx.doi.org/10.1007/978-3-662-03008-0_9).
- [76] Jacob N. Israelachvili and Patricia M. McGuiggan. Adhesion and short-range forces between surfaces. part i: New apparatus for surface force measurements. *Journal of Materials Research*, 5(10):2223–2231, October 1990. ISSN 2044-5326. doi: 10.1557/jmr.1990.2223. URL <http://dx.doi.org/10.1557/jmr.1990.2223>.
- [77] J Israelachvili, Y Min, M Akbulut, A Alig, G Carver, W Greene, K Kristiansen, E Meyer, N Pesika, K Rosenberg, and H Zeng. Recent advances in the surface forces apparatus (sfa) technique. *Reports on Progress in Physics*, 73(3):036601, January 2010. ISSN 1361-6633. doi: 10.1088/0034-4885/73/3/036601. URL <http://dx.doi.org/10.1088/0034-4885/73/3/036601>.
- [78] Jeffrey R. Moffitt, Yann R. Chemla, Steven B. Smith, and Carlos Bustamante. Recent advances in optical tweezers. *Annual Review of Biochemistry*, 77(1):205–228, June 2008. ISSN 1545-4509. doi: 10.1146/annurev.biochem.77.043007.090225. URL <http://dx.doi.org/10.1146/annurev.biochem.77.043007.090225>.
- [79] Keir C Neuman and Attila Nagy. Single-molecule force spectroscopy: optical tweezers, magnetic tweezers and atomic force microscopy. *Nature Methods*, 5(6):491–505, May 2008. ISSN 1548-7105. doi: 10.1038/nmeth.1218. URL <http://dx.doi.org/10.1038/nmeth.1218>.
- [80] A. Yeung, T. Dabros, and J. Masliyah. Does equilibrium interfacial tension depend on method of measurement? *Journal of Colloid and Interface Science*, 208(1):241–247, December 1998. ISSN 0021-9797. doi: 10.1006/jcis.1998.5807. URL <http://dx.doi.org/10.1006/jcis.1998.5807>.

- [81] Robert M Hochmuth. Micropipette aspiration of living cells. *Journal of Biomechanics*, 33(1):15–22, January 2000. ISSN 0021-9290. doi: 10.1016/s0021-9290(99)00175-x. URL [http://dx.doi.org/10.1016/s0021-9290\(99\)00175-x](http://dx.doi.org/10.1016/s0021-9290(99)00175-x).
- [82] Z. Zhang, M. A. Ferenczi, A. C. Lush, and C. R. Thomas. A novel micromanipulation technique for measuring the bursting strength of single mammalian cells. *Applied Microbiology and Biotechnology*, 36(2):208–210, November 1991. ISSN 1432-0614. doi: 10.1007/bf00164421. URL <http://dx.doi.org/10.1007/bf00164421>.
- [83] Z. Zhang. Mechanical strength of single microcapsules determined by a novel micromanipulation technique. *Journal of Microencapsulation*, 16(1):117–124, January 1999. ISSN 1464-5246. doi: 10.1080/026520499289365. URL <http://dx.doi.org/10.1080/026520499289365>.
- [84] G Sun and Z Zhang. Mechanical strength of microcapsules made of different wall materials. *International Journal of Pharmaceutics*, 242(1–2):307–311, August 2002. ISSN 0378-5173. doi: 10.1016/s0378-5173(02)00193-x. URL [http://dx.doi.org/10.1016/s0378-5173\(02\)00193-x](http://dx.doi.org/10.1016/s0378-5173(02)00193-x).
- [85] Michael Kappl and Hans-Jürgen Butt. The colloidal probe technique and its application to adhesion force measurements. *Particle & Particle Systems Characterization*, 19(3):129, July 2002. ISSN 1521-4117. doi: 10.1002/1521-4117(200207)19:3<129::aid-ppsc129>3.0.co;2-g. URL [http://dx.doi.org/10.1002/1521-4117\(200207\)19:3<129::aid-ppsc129>3.0.co;2-g](http://dx.doi.org/10.1002/1521-4117(200207)19:3<129::aid-ppsc129>3.0.co;2-g).
- [86] Mahdi Farshchi-Tabrizi, Michael Kappl, Yajun Cheng, Jochen Gutmann, and Hans-Jürgen Butt. On the adhesion between fine particles and nanocontacts: An atomic force microscope study. *Langmuir*, 22(5):2171–2184, February 2006. ISSN 1520-5827. doi: 10.1021/la052760z. URL <http://dx.doi.org/10.1021/la052760z>.
- [87] Yun-Han Huang, Xiran Li, Mariano Michelon, Bruna C. Leopercio, Marcio S. Carvalho, and John M. Frostad. Effects of aging on the shelf life and viscoelasticity of gellan gum microcapsules. *Food Hydrocolloids*, 121:106982, December 2021. ISSN 0268-005X. doi: 10.1016/j.foodhyd.2021.106982. URL <http://dx.doi.org/10.1016/j.foodhyd.2021.106982>.
- [88] Qi Feng, Dingguo Li, Qingtao Li, Haofei Li, Zetao Wang, Shuangli Zhu, Zefeng Lin, Xiaodong Cao, and Hua Dong. Assembling microgels via dynamic cross-linking reaction improves printability, microporosity, tissue-adhesion, and self-healing of microgel bioink for extrusion bio-printing. *ACS Applied Materials & Interfaces*, 14(13):15653–15666, March 2022. ISSN 1944-8252. doi: 10.1021/acsami.2c01295. URL <http://dx.doi.org/10.1021/acsami.2c01295>.
- [89] Leyan Xuan, Yingying Hou, Lu Liang, Jialin Wu, Kai Fan, Liming Lian, Jianhua Qiu, Yingling Miao, Hossein Ravanbakhsh, Ming Xu, and Guosheng Tang. Microgels for cell delivery in tissue engineering and regenerative medicine. *Nano-Micro Letters*, 16(1), June 2024. ISSN 2150-5551. doi: 10.1007/s40820-024-01421-5. URL <http://dx.doi.org/10.1007/s40820-024-01421-5>.
- [90] Shalini Saxena, Caroline E. Hansen, and L. Andrew Lyon. Microgel mechanics in biomaterial design. *Accounts of Chemical Research*, 47(8):2426–2434, May 2014. ISSN 1520-4898. doi: 10.1021/ar500131v. URL <http://dx.doi.org/10.1021/ar500131v>.
- [91] Yuhang Hu and Zhigang Suo. Viscoelasticity and poroelasticity in elastomeric gels. *Acta Mechanica Solida Sinica*, 25(5):441–458, October 2012. ISSN 0894-9166. doi: 10.1016/s0894-9166(12)60039-1. URL [http://dx.doi.org/10.1016/s0894-9166\(12\)60039-1](http://dx.doi.org/10.1016/s0894-9166(12)60039-1).

- [92] A.H.D. Cheng. *Poroelasticity*. Theory and Applications of Transport in Porous Media. Springer International Publishing, 2016. ISBN 9783319252025. URL <https://books.google.ca/books?id=SZkFDAAAQBAJ>.
- [93] Huai Nyin Yow and Alexander F. Routh. Formation of liquid core–polymer shell microcapsules. *Soft Matter*, 2(11):940–949, 2006. ISSN 1744-6848. doi: 10.1039/b606965g. URL <http://dx.doi.org/10.1039/b606965g>.
- [94] Xiu-Lan Yang, Xiao-Jie Ju, Xiao-Ting Mu, Wei Wang, Rui Xie, Zhuang Liu, and Liang-Yin Chu. Core–shell chitosan microcapsules for programmed sequential drug release. *ACS Applied Materials & Interfaces*, 8(16):10524–10534, April 2016. ISSN 1944-8252. doi: 10.1021/acsami.6b01277. URL <http://dx.doi.org/10.1021/acsami.6b01277>.
- [95] Chike K. Okwara, Roza Vaez Ghaemi, Charlotte Yu, Melissa Le, Vikramaditya G. Yadav, and John M. Frostad. The mechanical properties of neurospheres. *Advanced Engineering Materials*, 23(8), May 2021. ISSN 1527-2648. doi: 10.1002/adem.202100172. URL <http://dx.doi.org/10.1002/adem.202100172>.
- [96] Yun-Han Huang, Roza Vaez Ghaemi, James Cheon, Vikramaditya G. Yadav, and John M. Frostad. The mechanical effects of chemical stimuli on neurospheres. *Biomechanics and Modeling in Mechanobiology*, 23(4):1319–1329, April 2024. ISSN 1617-7940. doi: 10.1007/s10237-024-01841-7. URL <http://dx.doi.org/10.1007/s10237-024-01841-7>.
- [97] D. Langevin. Rheology of adsorbed surfactant monolayers at fluid surfaces. *Annual Review of Fluid Mechanics*, 46(1):47–65, January 2014. ISSN 1545-4479. doi: 10.1146/annurev-fluid-010313-141403. URL <http://dx.doi.org/10.1146/annurev-fluid-010313-141403>.
- [98] Alberto Ponce-Torres, Miguel A. Herrada, José M. Montanero, and José M. Vega. Linear and nonlinear dynamics of an insoluble surfactant-laden liquid bridge. *Physics of Fluids*, 28(11), November 2016. ISSN 1089-7666. doi: 10.1063/1.4967289. URL <http://dx.doi.org/10.1063/1.4967289>.
- [99] Gwynn J. Elfring, L. Gary Leal, and Todd M. Squires. Surface viscosity and marangoni stresses at surfactant laden interfaces. *Journal of Fluid Mechanics*, 792:712–739, March 2016. ISSN 1469-7645. doi: 10.1017/jfm.2016.96. URL <http://dx.doi.org/10.1017/jfm.2016.96>.
- [100] Kenneth A. Brakke. The surface evolver. *Experimental Mathematics*, 1(2):141–165, January 1992. ISSN 1944-950X. doi: 10.1080/10586458.1992.10504253. URL <http://dx.doi.org/10.1080/10586458.1992.10504253>.
- [101] Robert Phelan, Denis Weaire, and Kenneth Brakke. Computation of equilibrium foam structures using the surface evolver. *Experimental Mathematics*, 4(3):181–192, January 1995. ISSN 1944-950X. doi: 10.1080/10586458.1995.10504320. URL <http://dx.doi.org/10.1080/10586458.1995.10504320>.
- [102] CH Delaunay. On the surface of revolution whose mean curvature is constant. *Journal of Pure and Applied Mathematics*, 6:309–315, 1841. URL [http://www.numdam.org/item/JMPA\\_1841\\_1\\_6\\_\\_309\\_0.pdf](http://www.numdam.org/item/JMPA_1841_1_6__309_0.pdf).
- [103] Robert Finn. *Equilibrium Capillary Surfaces*. Springer New York, 1986. ISBN 9781461385844. doi: 10.1007/978-1-4613-8584-4. URL <http://dx.doi.org/10.1007/978-1-4613-8584-4>.

- [104] I.M. Gelfand and S.V. Fomin. *Calculus of Variations*. Dover Books on Mathematics. Dover Publications, 2012. ISBN 9780486135014. URL <https://books.google.ca/books?id=CeC7AQAAQBAJ>.
- [105] P. H. Saksono and D. Perić. On finite element modelling of surface tension variational formulation and applications – part i: Quasistatic problems. *Computational Mechanics*, 38(3):265–281, November 2005. ISSN 1432-0924. doi: 10.1007/s00466-005-0747-5. URL <http://dx.doi.org/10.1007/s00466-005-0747-5>.
- [106] Timm Krüger, Halim Kusumaatmaja, Alexandr Kuzmin, Orest Shardt, Goncalo Silva, and Erlend Magnus Viggen. *The Lattice Boltzmann Method: Principles and Practice*. Springer International Publishing, 2017. ISBN 9783319446493. doi: 10.1007/978-3-319-44649-3. URL <http://dx.doi.org/10.1007/978-3-319-44649-3>.
- [107] Bernard P. Binks and Tommy S. Horozov. *Colloidal Particles at Liquid Interfaces: An Introduction*, page 1–74. Cambridge University Press, August 2006. ISBN 9780511536670. doi: 10.1017/cbo9780511536670.002. URL <http://dx.doi.org/10.1017/cbo9780511536670.002>.
- [108] David Julian McClements. *Food Emulsions: Principles, Practices, and Techniques, Third Edition*. CRC Press, August 2015. ISBN 9780429154034. doi: 10.1201/b18868. URL <http://dx.doi.org/10.1201/b18868>.
- [109] Tharwat F. Tadros. Emulsion formation, stability, and rheology, January 2013. URL <http://dx.doi.org/10.1002/9783527647941.ch1>.
- [110] Katharina Hauf and Erin Koos. Structure of capillary suspensions and their versatile applications in the creation of smart materials. *MRS Communications*, 8(2):332–342, March 2018. ISSN 2159-6867. doi: 10.1557/mrc.2018.28. URL <http://dx.doi.org/10.1557/mrc.2018.28>.
- [111] Frank Bossler and Erin Koos. Structure of particle networks in capillary suspensions with wetting and nonwetting fluids. *Langmuir*, 32(6):1489–1501, February 2016. ISSN 1520-5827. doi: 10.1021/acs.langmuir.5b04246. URL <http://dx.doi.org/10.1021/acs.langmuir.5b04246>.
- [112] Thomas Young. An essay on the cohesion of fluids. *Abstracts of the Papers Printed in the Philosophical Transactions of the Royal Society of London*, 1:171–172, December 1832. ISSN 2053-9142. doi: 10.1098/rstl.1800.0095. URL <http://dx.doi.org/10.1098/rstl.1800.0095>.
- [113] Pierre Simon Laplace. *Traité de mécanique céleste*, volume 5. Chez JBM Duprat, libraire pour les mathématiques, quai des Augustins, 1825.
- [114] Carolo Friderico Gauss. *Principia Generalia Theoriae Figurae Fluidorum in Statu Aequilibrii*, page 29–77. Springer Berlin Heidelberg, 1877. ISBN 9783642493195. doi: 10.1007/978-3-642-49319-5\_3. URL [http://dx.doi.org/10.1007/978-3-642-49319-5\\_3](http://dx.doi.org/10.1007/978-3-642-49319-5_3).
- [115] S.D. Poisson. *Traité De Mécanique*. Creative Media Partners, LLC, 2022. ISBN 9781019059661. URL <https://books.google.ca/books?id=rjGGzwEACAAJ>.
- [116] Augustin-Louis Cauchy. Mémoire sur la pression et la traction qu'exerce un fluide sur les surfaces qu'il mouille. *Mémoires de l'Académie des Sciences de Paris*, 13:279–296, 1832.
- [117] Joseph Antoine Ferdinand Plateau. *Experimental and theoretical statics of liquids subjected to molecular forces alone*, volume 2. Gauthier-Villars, 1873. URL <https://libarch.nmu.org.ua/bitstream/handle/GenofondUA/18567/d1b069e4addb625425c954ae762b2d9f.pdf?sequence=1>.

- [118] Willy Howe. *Die Rotations-Flächen welche bei vorgeschriebener Flächengrösse ein möglichst grosses oder kleines Volumen enthalten.* Carl Koepsel's Buchdr., 1887. doi: 10.18452/203. URL <https://doi.org/10.18452/203>.
- [119] F. M. Orr, L. E. Scriven, and A. P. Rivas. Pendular rings between solids: meniscus properties and capillary force. *Journal of Fluid Mechanics*, 67(4):723–742, February 1975. ISSN 1469-7645. doi: 10.1017/s0022112075000572. URL <http://dx.doi.org/10.1017/s0022112075000572>.
- [120] Katsuei Kenmotsu. Surfaces of revolution with prescribed mean curvature. *Tohoku Mathematical Journal*, 32(1), January 1980. ISSN 0040-8735. doi: 10.2748/tmj/1178229688. URL <http://dx.doi.org/10.2748/tmj/1178229688>.
- [121] S. Herminghaus. Dynamics of wet granular matter. *Advances in Physics*, 54(3):221–261, May 2005. ISSN 1460-6976. doi: 10.1080/00018730500167855. URL <http://dx.doi.org/10.1080/00018730500167855>.
- [122] Shelley Lynn Anna. Droplets and bubbles in microfluidic devices. *Annual Review of Fluid Mechanics*, 48(1):285–309, January 2016. ISSN 1545-4479. doi: 10.1146/annurev-fluid-122414-034425. URL <http://dx.doi.org/10.1146/annurev-fluid-122414-034425>.
- [123] Jan-Henning Dirks and Walter Federle. Fluid-based adhesion in insects – principles and challenges. *Soft Matter*, 7(23):11047, 2011. ISSN 1744-6848. doi: 10.1039/c1sm06269g. URL <http://dx.doi.org/10.1039/c1sm06269g>.
- [124] Jun Shintake, Vito Cacucciolo, Dario Floreano, and Herbert Shea. Soft robotic grippers. *Advanced Materials*, 30(29), May 2018. ISSN 1521-4095. doi: 10.1002/adma.201707035. URL <http://dx.doi.org/10.1002/adma.201707035>.
- [125] J.N. Israelachvili. *Intermolecular and Surface Forces.* Intermolecular and Surface Forces. Academic Press, 2010. ISBN 9780080923635. URL <https://books.google.ca/books?id=MVbWBhubrgIC>.
- [126] Carl M. Bender and Steven A. Orszag. *Advanced Mathematical Methods for Scientists and Engineers I.* Springer New York, 1999. ISBN 9781475730692. doi: 10.1007/978-1-4757-3069-2. URL <http://dx.doi.org/10.1007/978-1-4757-3069-2>.
- [127] Gwynn J. Elfring and Eric Lauga. Buckling instability of squeezed droplets. *Physics of Fluids*, 24(7), July 2012. ISSN 1089-7666. doi: 10.1063/1.4731795. URL <http://dx.doi.org/10.1063/1.4731795>.
- [128] Karine Guevorkian, Marie-Josée Colbert, Mélanie Durth, Sylvie Dufour, and Françoise Brochard-Wyart. Aspiration of biological viscoelastic drops. *Physical Review Letters*, 104(21), May 2010. ISSN 1079-7114. doi: 10.1103/physrevlett.104.218101. URL <http://dx.doi.org/10.1103/physrevlett.104.218101>.
- [129] Victoria C. Harrold, Maxime Paven, Doris Vollmer, and James S. Sharp. Rheological properties of viscoelastic drops on superamphiphobic substrates. *Langmuir*, 32(16):4071–4076, April 2016. ISSN 1520-5827. doi: 10.1021/acs.langmuir.6b00779. URL <http://dx.doi.org/10.1021/acs.langmuir.6b00779>.

- [130] Nicole Taylor, Shana Elbaum-Garfinkle, Nilesh Vaidya, Huaiying Zhang, Howard A. Stone, and Clifford P. Brangwynne. Biophysical characterization of organelle-based rna/protein liquid phases using microfluidics. *Soft Matter*, 12(45):9142–9150, 2016. ISSN 1744-6848. doi: 10.1039/c6sm01087c. URL <http://dx.doi.org/10.1039/c6sm01087c>.
- [131] Edward M Courchaine, Alice Lu, and Karla M Neugebauer. Droplet organelles? *The EMBO Journal*, 35(15):1603–1612, June 2016. ISSN 1460-2075. doi: 10.15252/embj.201593517. URL <http://dx.doi.org/10.15252/embj.201593517>.
- [132] Eric Dickinson. Hydrocolloids at interfaces and the influence on the properties of dispersed systems. *Food Hydrocolloids*, 17(1):25–39, January 2003. ISSN 0268-005X. doi: 10.1016/s0268-005x(01)00120-5. URL [http://dx.doi.org/10.1016/s0268-005x\(01\)00120-5](http://dx.doi.org/10.1016/s0268-005x(01)00120-5).
- [133] Maytal Foox and Meital Zilberman. Drug delivery from gelatin-based systems. *Expert Opinion on Drug Delivery*, 12(9):1547–1563, May 2015. ISSN 1744-7593. doi: 10.1517/17425247.2015.1037272. URL <http://dx.doi.org/10.1517/17425247.2015.1037272>.
- [134] Aswini Rajendran, Veronica Elumalai, Saranya Balasubramaniyam, and Karthikeyan Elumalai. Transfersome formulations as innovative carriers for transdermal drug delivery: Composition, properties, and therapeutic applications. *Biomedical Materials & Devices*, January 2025. ISSN 2731-4820. doi: 10.1007/s44174-024-00269-y. URL <http://dx.doi.org/10.1007/s44174-024-00269-y>.
- [135] Josef Stefan. Versuche über die scheinbare adhäsion. *Annalen der Physik*, 230(2):316–318, 1875.
- [136] N. Phan-Thien and R. I. Tanner. Viscoelastic squeeze-film flows – maxwell fluids. *Journal of Fluid Mechanics*, 129(1):265, April 1983. ISSN 1469-7645. doi: 10.1017/s0022112083000762. URL <http://dx.doi.org/10.1017/s0022112083000762>.
- [137] N. Phan-Thien and R.I. Tanner. Lubrication squeeze-film theory for the oldroyd-b fluid. *Journal of Non-Newtonian Fluid Mechanics*, 14:327–335, January 1984. ISSN 0377-0257. doi: 10.1016/0377-0257(84)80051-8. URL [http://dx.doi.org/10.1016/0377-0257\(84\)80051-8](http://dx.doi.org/10.1016/0377-0257(84)80051-8).
- [138] N. Phan-thien, F. Sugeng, and R.I. Tanner. The squeeze-film flow of a viscoelastic fluid. *Journal of Non-Newtonian Fluid Mechanics*, 24(1):97–119, January 1987. ISSN 0377-0257. doi: 10.1016/0377-0257(87)85006-1. URL [http://dx.doi.org/10.1016/0377-0257\(87\)85006-1](http://dx.doi.org/10.1016/0377-0257(87)85006-1).
- [139] N. Phan-Thien and H.T. Low. Squeeze-film flow of a viscoelastic fluid a lubrication model. *Journal of Non-Newtonian Fluid Mechanics*, 28(2):129–148, January 1988. ISSN 0377-0257. doi: 10.1016/0377-0257(88)85036-5. URL [http://dx.doi.org/10.1016/0377-0257\(88\)85036-5](http://dx.doi.org/10.1016/0377-0257(88)85036-5).
- [140] J.D Sherwood and D Durban. Squeeze-flow of a herschel–bulkley fluid. *Journal of Non-Newtonian Fluid Mechanics*, 77(1–2):115–121, May 1998. ISSN 0377-0257. doi: 10.1016/s0377-0257(97)00099-2. URL [http://dx.doi.org/10.1016/s0377-0257\(97\)00099-2](http://dx.doi.org/10.1016/s0377-0257(97)00099-2).
- [141] Larisa Muravleva. Squeeze plane flow of viscoplastic bingham material. *Journal of Non-Newtonian Fluid Mechanics*, 220:148–161, June 2015. ISSN 0377-0257. doi: 10.1016/j.jnnfm.2015.01.012. URL <http://dx.doi.org/10.1016/j.jnnfm.2015.01.012>.

- [142] Larisa Muravleva. Axisymmetric squeeze flow of a viscoplastic bingham medium. *Journal of Non-Newtonian Fluid Mechanics*, 249:97–120, November 2017. ISSN 0377-0257. doi: 10.1016/j.jnnfm.2017.09.006. URL <http://dx.doi.org/10.1016/j.jnnfm.2017.09.006>.
- [143] Zhaolin Zheng, Haiou Xie, Xuedong Chen, Xuhui Liu, Wei Yang, Yong Xu, and Wenbin Huang. Squeeze flow of a maxwell fluid between two parallel disks or two spheres. *Physics of Fluids*, 35(8), August 2023. ISSN 1089-7666. doi: 10.1063/5.0161828. URL <http://dx.doi.org/10.1063/5.0161828>.
- [144] Zhaolin Zheng, Xuedong Chen, and Wei Yang. Squeeze flow of a maxwell fluid between a sphere and a plate. *Physics of Fluids*, 36(1), January 2024. ISSN 1089-7666. doi: 10.1063/5.0185335. URL <http://dx.doi.org/10.1063/5.0185335>.
- [145] Nhan Phan-Thien. Squeezing flow of a viscoelastic solid. *Journal of Non-Newtonian Fluid Mechanics*, 95(2–3):343–362, December 2000. ISSN 0377-0257. doi: 10.1016/s0377-0257(00)00175-0. URL [http://dx.doi.org/10.1016/s0377-0257\(00\)00175-0](http://dx.doi.org/10.1016/s0377-0257(00)00175-0).
- [146] A. C. Pipkin. *Lectures on Viscoelasticity Theory*. Springer New York, 1986. ISBN 9781461210788. doi: 10.1007/978-1-4612-1078-8. URL <http://dx.doi.org/10.1007/978-1-4612-1078-8>.
- [147] B. I. Nelson and J. M. Dealy. *Dynamic mechanical analysis using complex waveforms*, page 138–164. Springer Netherlands, 1998. ISBN 9789401149341. doi: 10.1007/978-94-011-4934-1\_4. URL [http://dx.doi.org/10.1007/978-94-011-4934-1\\_4](http://dx.doi.org/10.1007/978-94-011-4934-1_4).
- [148] V. Tirtaatmadja and T. Sridhar. A filament stretching device for measurement of extensional viscosity. *Journal of Rheology*, 37(6):1081–1102, November 1993. ISSN 1520-8516. doi: 10.1122/1.550372. URL <http://dx.doi.org/10.1122/1.550372>.
- [149] Harishankar Manikantan and Todd M. Squires. Surfactant dynamics: hidden variables controlling fluid flows. *Journal of Fluid Mechanics*, 892, April 2020. ISSN 1469-7645. doi: 10.1017/jfm.2020.170. URL <http://dx.doi.org/10.1017/jfm.2020.170>.
- [150] Jan Engmann, Colin Servais, and Adam S. Burbidge. Squeeze flow theory and applications to rheometry: A review. *Journal of Non-Newtonian Fluid Mechanics*, 132(1–3):1–27, December 2005. ISSN 0377-0257. doi: 10.1016/j.jnnfm.2005.08.007. URL <http://dx.doi.org/10.1016/j.jnnfm.2005.08.007>.
- [151] V. Girault and P.A. Raviart. *Finite Element Methods for Navier-Stokes Equations: Theory and Algorithms*. Springer Series in Computational Mathematics. Springer Berlin Heidelberg, 2012. ISBN 9783642616235. URL <https://books.google.com/books?id=8C7vCAAAQBAJ>.
- [152] A.J. Baker. *Finite Element Computational Fluid Mechanics*. International student edition. Hemisphere Publishing Corporation, 1983. ISBN 9780070034655. URL <https://books.google.com/books?id=85RRAAAAMAAJ>.
- [153] W.B.J. Zimmerman. *Multiphysics Modelling with Finite Element Methods*. Series on stability. London, 2006. ISBN 9789812568434. URL <https://books.google.com/books?id=Cox9QgAACAAJ>.
- [154] Roger W. Pryor. *Multiphysics Modeling Using COMSOL®4*. De Gruyter, January 2012. ISBN 9781937585730. doi: 10.1515/9781937585730. URL <http://dx.doi.org/10.1515/9781937585730>.

- [155] J.E. Matsson. *An Introduction to Ansys Fluent 2023*. SDC Publications, 2023. ISBN 9781630576486. URL <https://books.google.com/books?id=XLTFAAAQBAJ>.
- [156] J. R. Barber. *Elasticity*. Springer Netherlands, 2010. ISBN 9789048138098. doi: 10.1007/978-90-481-3809-8. URL <http://dx.doi.org/10.1007/978-90-481-3809-8>.
- [157] Phillip L. Gould. *Introduction to Linear Elasticity*. Springer New York, 2013. ISBN 9781461448334. doi: 10.1007/978-1-4614-4833-4. URL <http://dx.doi.org/10.1007/978-1-4614-4833-4>.
- [158] Jacob Lubliner and Panayiotis Papadopoulos. *Introduction to Solid Mechanics: An Integrated Approach*. Springer New York, 2014. ISBN 9781461467687. doi: 10.1007/978-1-4614-6768-7. URL <http://dx.doi.org/10.1007/978-1-4614-6768-7>.
- [159] Bruno Andreotti, Oliver Bäumchen, François Boulogne, Karen E. Daniels, Eric R. Dufresne, Hugo Perrin, Thomas Salez, Jacco H. Snoeijer, and Robert W. Style. Solid capillarity: when and how does surface tension deform soft solids? *Soft Matter*, 12(12):2993–2996, 2016. ISSN 1744-6848. doi: 10.1039/c5sm03140k. URL <http://dx.doi.org/10.1039/c5sm03140k>.
- [160] Qin Xu, Katharine E. Jensen, Rostislav Boltyanskiy, Raphaël Sarfati, Robert W. Style, and Eric R. Dufresne. Direct measurement of strain-dependent solid surface stress. *Nature Communications*, 8(1), September 2017. ISSN 2041-1723. doi: 10.1038/s41467-017-00636-y. URL <http://dx.doi.org/10.1038/s41467-017-00636-y>.
- [161] Robert W. Style, Anand Jagota, Chung-Yuen Hui, and Eric R. Dufresne. Elastocapillarity: Surface tension and the mechanics of soft solids. *Annual Review of Condensed Matter Physics*, 8(1):99–118, March 2017. ISSN 1947-5462. doi: 10.1146/annurev-conmatphys-031016-025326. URL <http://dx.doi.org/10.1146/annurev-conmatphys-031016-025326>.
- [162] Jin Young Kim, Stefanie Heyden, Dominic Gerber, Nicolas Bain, Eric R. Dufresne, and Robert W. Style. Measuring surface tensions of soft solids with huge contact-angle hysteresis. *Physical Review X*, 11(3), July 2021. ISSN 2160-3308. doi: 10.1103/physrevx.11.031004. URL <http://dx.doi.org/10.1103/physrevx.11.031004>.
- [163] Romain Marcombe, Shengqiang Cai, Wei Hong, Xuanhe Zhao, Yuri Lapusta, and Zhigang Suo. A theory of constrained swelling of a ph-sensitive hydrogel. *Soft Matter*, 6(4):784, 2010. ISSN 1744-6848. doi: 10.1039/b917211d. URL <http://dx.doi.org/10.1039/b917211d>.
- [164] Sengqiang Cai, Yuhang Hu, Xuanhe Zhao, and Zhigang Suo. Poroelasticity of a covalently crosslinked alginate hydrogel under compression. *Journal of Applied Physics*, 108(11), December 2010. ISSN 1089-7550. doi: 10.1063/1.3517146. URL <http://dx.doi.org/10.1063/1.3517146>.
- [165] Luis M. Carrión, Miguel A. Herrada, José M. Montanero, and José M. Vega. Mean flow produced by small-amplitude vibrations of a liquid bridge with its free surface covered with an insoluble surfactant. *Physical Review E*, 96(3), September 2017. ISSN 2470-0053. doi: 10.1103/physreve.96.033101. URL <http://dx.doi.org/10.1103/physreve.96.033101>.
- [166] E.A Boucher and M.J.B Evans. Capillary phenomena. xii. properties of fluid bridges between solids in a gravitational field. *Journal of Colloid and Interface Science*, 75(2):409–418, June 1980. ISSN 0021-9797. doi: 10.1016/0021-9797(80)90466-x. URL [http://dx.doi.org/10.1016/0021-9797\(80\)90466-x](http://dx.doi.org/10.1016/0021-9797(80)90466-x).

- [167] E.A. Boucher, M.J.B. Evans, and T.G.J. Jones. The computation of interface shapes for capillary systems in a gravitational field. *Advances in Colloid and Interface Science*, 27(1–2): 43–79, May 1987. ISSN 0001-8686. doi: 10.1016/0001-8686(87)85009-1. URL [http://dx.doi.org/10.1016/0001-8686\(87\)85009-1](http://dx.doi.org/10.1016/0001-8686(87)85009-1).
- [168] Jong-In Yang and Jooyoo Hong. Determination of the young's angle using static friction in capillary bridges. *arXiv preprint arXiv:2411.15021*, 2024. URL <https://doi.org/10.48550/arXiv.2411.15021>.
- [169] Jason S. Wexler, Tiara M. Heard, and Howard A. Stone. Capillary bridges between soft substrates. *Physical Review Letters*, 112(6), February 2014. ISSN 1079-7114. doi: 10.1103/physrevlett.112.066102. URL <http://dx.doi.org/10.1103/physrevlett.112.066102>.
- [170] E. J. De Souza, L. Gao, T. J. McCarthy, E. Arzt, and A. J. Crosby. Effect of contact angle hysteresis on the measurement of capillary forces. *Langmuir*, 24(4):1391–1396, October 2007. ISSN 1520-5827. doi: 10.1021/la702188t. URL <http://dx.doi.org/10.1021/la702188t>.
- [171] H. Chen, A. Amirfazli, and T. Tang. Modeling liquid bridge between surfaces with contact angle hysteresis. *Langmuir*, 29(10):3310–3319, March 2013. ISSN 1520-5827. doi: 10.1021/la304870h. URL <http://dx.doi.org/10.1021/la304870h>.
- [172] Gerald Henry Meeten. Squeeze flow of soft solids between rough surfaces. *Rheologica Acta*, 43(1):6–16, February 2004. ISSN 1435-1528. doi: 10.1007/s00397-003-0311-1. URL <http://dx.doi.org/10.1007/s00397-003-0311-1>.
- [173] Nobuo Maeda, Jacob N. Israelachvili, and Mika M. Kohonen. Evaporation and instabilities of microscopic capillary bridges. *Proceedings of the National Academy of Sciences*, 100(3): 803–808, January 2003. ISSN 1091-6490. doi: 10.1073/pnas.0234283100. URL <http://dx.doi.org/10.1073/pnas.0234283100>.
- [174] Mradul Ojha, Lalit Kumar, and Rajneesh Bhardwaj. Evaporating capillary bridges of pure and binary liquids. *Physics of Fluids*, 36(11), November 2024. ISSN 1089-7666. doi: 10.1063/5.0234646. URL <http://dx.doi.org/10.1063/5.0234646>.

## Appendix A

# Asymptotic expansion of the interface mean curvature

The regular perturbation expansions in  $\varepsilon$  for the dimensionless interface shape function  $\hat{\mathcal{R}}(\hat{z}, \hat{t})$  and the interface unit normal  $\mathbf{n}$  are given in Eqn. (3.15). Substituting these expansions into the expression of the dimensionless mean curvature  $\hat{\mathcal{H}} = R\mathcal{H}$  of the interface in Eqn. (3.5), we derive:

$$\begin{aligned} 1 + (\hat{\nabla}_\parallel \cdot \mathbf{n}_1) \varepsilon + \mathcal{O}(\varepsilon^2) &= \left[ 1 + \varepsilon \hat{\mathcal{R}}_1 + \mathcal{O}(\varepsilon^2) \right]^{-1} \left[ 1 + \left( \frac{\varepsilon}{\delta} \right)^2 \hat{\mathcal{R}}'_1 + \mathcal{O}\left( \frac{\varepsilon^3}{\delta^2} \right) \right]^{-1/2} \\ &\quad - \left[ \left( \frac{\varepsilon}{\delta^2} \right) \hat{\mathcal{R}}''_1 + \left( \frac{\varepsilon}{\delta} \right)^2 \hat{\mathcal{R}}''_2 + \mathcal{O}\left( \frac{\varepsilon^3}{\delta^2} \right) \right] \\ &\quad \times \left[ 1 + \left( \frac{\varepsilon}{\delta} \right)^2 \hat{\mathcal{R}}'_1 + \mathcal{O}\left( \frac{\varepsilon^3}{\delta^2} \right) \right]^{-3/2}. \end{aligned} \quad (\text{A.1})$$

In accordance with the scaling relation  $\varepsilon \sim \delta^2$ , we have retained terms effectively up to  $\mathcal{O}(\varepsilon)$ . Specifically, contributions of  $\mathcal{O}(\varepsilon/\delta^2) = \mathcal{O}(1)$  and  $\mathcal{O}((\varepsilon/\delta)^2) = \mathcal{O}(\varepsilon)$  are included, while terms of  $\mathcal{O}(\varepsilon^3/\delta^2) = \mathcal{O}(\varepsilon^2)$  and higher are neglected to ensure consistency in the expansion.

In the above expansion, the term  $\mathcal{R}^{-1}$  admits the following Taylor series under the small strain amplitude approximation,  $\varepsilon \ll 1$ :

$$\left[ 1 + \varepsilon \hat{\mathcal{R}}_1 + \mathcal{O}(\varepsilon^2) \right]^{-1} = 1 - \varepsilon \hat{\mathcal{R}}_1 + \mathcal{O}(\varepsilon^2).$$

The term  $(1 + \mathcal{R}'^2)^{-1/2}$  admits the following expansion under the small-slope approximation,  $\varepsilon/\delta \sim \delta \ll 1$ :

$$\left[ 1 + \left( \frac{\varepsilon}{\delta} \right)^2 \hat{\mathcal{R}}'_1 + \mathcal{O}\left( \frac{\varepsilon^3}{\delta^2} \right) \right]^{-1/2} = 1 - \frac{1}{2} \left( \frac{\varepsilon}{\delta} \right)^2 \hat{\mathcal{R}}'_1 + \mathcal{O}\left( \left( \frac{\varepsilon}{\delta} \right)^4 \right).$$

Similarly, for the term  $(1 + \mathcal{R}'^2)^{-3/2}$ , we obtain:

$$\left[ 1 + \left( \frac{\varepsilon}{\delta} \right)^2 \hat{\mathcal{R}}'_1 + \mathcal{O}\left( \frac{\varepsilon^3}{\delta^2} \right) \right]^{-3/2} = 1 - \frac{3}{2} \left( \frac{\varepsilon}{\delta} \right)^2 \hat{\mathcal{R}}'_1 + \mathcal{O}\left( \left( \frac{\varepsilon}{\delta} \right)^4 \right).$$

In all cases, the expansions are truncated at  $\mathcal{O}((\varepsilon/\delta)^4) = \mathcal{O}(\varepsilon^2)$ .

Substituting the above expansions into Eqn. (A.1), we obtain the  $\mathcal{O}(\varepsilon)$  correction to the mean curvature  $\hat{\mathcal{H}}$ , denoted by  $\hat{\mathcal{H}}_1$ , which captures the leading-order dynamic contribution arising from the deformation of the interface:

$$2\hat{\mathcal{H}}_1 = \hat{\nabla}_\parallel \cdot \mathbf{n}_1 = -\hat{\mathcal{R}}_1 - \delta^{-2} \hat{\mathcal{R}}_1''. \quad (\text{A.2})$$

Here, the first term on the right-hand side corresponds to the leading-order dynamic correction to the azimuthal curvature, and the second term represents the corresponding correction to the meridional curvature. As expected in a thin substrate gap ( $\delta^2 \ll 1$ ), the meridional curvature correction dominates, being asymptotically larger by a factor of  $\mathcal{O}(\delta^{-2})$  relative to the azimuthal counterpart.

## Appendix B

# Validity of the bridge volume conservation constraint

### B.1 Pinned droplet case

In terms of the mean curvature  $\mathcal{H}$  and the capillary radius  $R$ , the bridge volume  $V_b$  can be written as:

$$\begin{aligned}
V_b(\mathcal{H}, R) &= 2\pi \int_0^{L/2} \mathcal{R}(z)^2 dz = 2\pi \int_0^{\pi/2-\theta} \left\{ \mathcal{R}(\phi)^2 \frac{dz}{d\phi} \right\} d\phi \\
&= -\frac{\pi}{4\mathcal{H}^3} \left[ 4\cos\theta - \frac{4}{3}\cos^3\theta - 4\mathcal{F}\cos\theta \right. \\
&\quad \left. + \int_0^{\pi/2-\theta} \left\{ 3\cos^2\xi (\cos^2\xi - 4\mathcal{F})^{1/2} + \frac{\cos^4\xi}{(\cos^2\xi - 4\mathcal{F})^{1/2}} \right\} d\xi \right] \\
&= V_d - 2V_c \\
&= \frac{2\pi}{3} \left[ 2R_d^3 - \frac{1}{\mathcal{H}^3} (2 - 3\sin\phi_L + \sin^3\phi_L) \right] \\
&= \frac{2\pi}{3} \left[ 2R_d^3 - \frac{1}{\mathcal{H}^3} \left\{ 2 - 3(1 - \mathcal{H}^2 R^2)^{1/2} + (1 - \mathcal{H}^2 R^2)^{3/2} \right\} \right], \tag{B.1}
\end{aligned}$$

where  $V_d = 4\pi R_d^3/3$  is the total droplet volume,  $V_c$  is the volume of either cap (within the left or right capillary), and  $\phi_L = \arccos(\mathcal{H}R)$  is the local tilt angle at the capillary rim for the left cap. The undeformed bridge volume  $V_{b,0}$  is obtained by substituting the undeformed mean curvature  $\mathcal{H} = \mathcal{H}_0 = 1/R_d$  into the above expression, and using the relation  $R/R_d = \sin\theta_0$ :

$$V_{b,0} = \frac{2\pi R_d^3}{3} \cos\theta_0 (\cos^2\theta_0 - 3).$$

This enables us to quantify the absolute relative change in bridge volume for any displacement from the undeformed state as:

$$\left| \frac{\Delta V_b}{V_{b,0}} \right| = \left| 1 - \left[ 2 - \hat{\mathcal{H}}^{-3} \left\{ 2 - 3(1 - \hat{\mathcal{H}}^2 \hat{R}^2)^{1/2} + (1 - \hat{\mathcal{H}}^2 \hat{R}^2)^{3/2} \right\} \right] \right| / [\cos\theta_0 (\cos^2\theta_0 - 3)],$$

where  $\hat{\mathcal{H}} = R_d \mathcal{H}$  is the dimensionless mean curvature and  $\hat{R} = R/R_d$  is the dimensionless capillary radius.

As shown in Fig. B.1, for any *admissible* mean curvature  $\hat{\mathcal{H}} \neq 1$  satisfying  $\hat{\mathcal{H}}\hat{R} \leq 1$ , the relative bridge volume change increases monotonically with the capillary radius  $\hat{R}$ , vanishing in the limit  $\hat{R} \rightarrow 0$ . Thus, smaller capillary radii yield smaller deviations in bridge volume. During both dilation ( $\hat{\mathcal{H}} < 1$ ) and compression ( $\hat{\mathcal{H}} > 1$ ) in the small-strain regime ( $|\Delta L/L_0| \ll 1$ ), the range of capillary radii over which volume remains approximately conserved expands as the mean curvature approaches the undeformed value  $\hat{\mathcal{H}} = 1$ , and shrinks as the deviation increases. Specifically, for a fixed capillary radius, the relative volume change increases with increasing deviation from the undeformed curvature (and hence with increasing strain). Additionally, in this regime, for symmetric curvature deviations in dilation and compression, the volume change is always greater during compression due to a higher curvature, as illustrated by the curvature pairs  $\hat{\mathcal{H}} = 0.9$  and  $1.1$ , and  $\hat{\mathcal{H}} = 0.7$  and  $1.3$ .

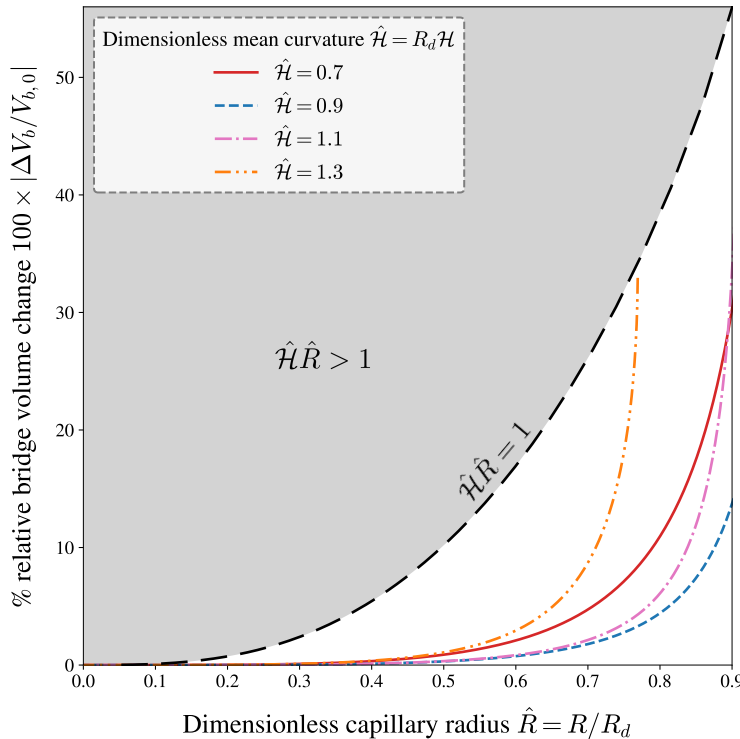


**Figure B.1:** Percentage relative change in bridge volume,  $100 \times |\Delta V_b/V_{b,0}|$ , plotted versus capillary radius  $\hat{R} = R/R_d$  (up to 0.9) for fixed mean curvatures  $\hat{\mathcal{H}} = R_d\mathcal{H} \in \{0.7, 0.9, 1.1, 1.3\}$  (*distinct line styles and colours*). These  $\hat{\mathcal{H}}$  values are representative of the small-strain regime, with  $R_d$  denoting the undeformed droplet radius. Each curve obeys the physical constraint  $\hat{\mathcal{H}}\hat{R} \leq 1$ . Consequently, in the small-strain regime, compression curves ( $\hat{\mathcal{H}} > 1$ ) are valid only for  $\hat{R} \leq 1/\hat{\mathcal{H}}$ , whereas dilation curves ( $\hat{\mathcal{H}} < 1$ ) are valid for all  $\hat{R}$ . Accordingly, all compression curves terminate at the *black long-dashed line*  $\hat{\mathcal{H}}\hat{R} = 1$ , while all dilation curves remain below it. The *light grey shaded region* above this line corresponds to the unphysical regime  $\hat{\mathcal{H}}\hat{R} > 1$ .

We referred to the concept of admissible mean curvature in the previous paragraph, which arises due to the appearance of the term  $(1 - \hat{\mathcal{H}}^2 \sin^2 \theta_0)^{1/2} = (1 - \hat{\mathcal{H}}^2 \hat{R}^2)^{1/2}$  in the bridge volume expression. This imposes the physical constraint  $\mathcal{H}\hat{R} \leq 1$ , reflecting the fundamental requirement that the radius of curvature  $1/\mathcal{H}$  of the caps—identical to that of the bridge—must be at least as large as the capillary radius  $R$ . As a result, for all capillary radii, any mean curvature smaller than the undeformed value  $\mathcal{H}_0 = 1/R_d$  can be attained during dilation. However, during compression ( $\mathcal{H} > 1/R_d$ ), there exists a maximum allowable mean curvature  $\mathcal{H} = 1/R$ , corresponding to the formation of hemispherical caps. Conversely, for a desired mean curvature during compression, the

largest capillary radius that can physically accommodate such curvature is  $R = 1/\mathcal{H}$ .

Following the above discussion, as shown in Fig. B.1, if we choose the capillary radius such that  $\hat{R} = R/R_d \in [0.3, 0.6]$ —a range typical for the CCFA—the relative change in bridge volume remains confined to under 5% for representative small-strain curvatures varying between  $\hat{\mathcal{H}} \approx 0.7$  (dilation) and  $\hat{\mathcal{H}} \approx 1.3$  (compression). Therefore, we can safely assume that the bridge volume remains constant throughout the quasi-static deformation of the droplet in the CCFA under small strain. As a result, in this limit, the bridge volume constraint (B.1) simplifies to:

$$\begin{aligned} V_b &= -\frac{\pi}{4\mathcal{H}^3} \left[ 4\cos\theta - \frac{4}{3}\cos^3\theta - 4\mathcal{F}\cos\theta \right. \\ &\quad \left. + \int_0^{\frac{\pi}{2}-\theta} \left\{ 3\cos^2\xi (\cos^2\xi - 4\mathcal{F})^{1/2} + \frac{\cos^4\xi}{(\cos^2\xi - 4\mathcal{F})^{1/2}} \right\} d\xi \right] \\ &= V_{b,0} = \frac{2\pi R_d^3}{3} \cos\theta_0 (\cos^2\theta_0 - 3). \end{aligned} \quad (\text{B.2})$$

## B.2 Constant capillary suction pressure case

Although the primary objective of Chapter 2 has been to lay down an analytical framework to study the equilibrium states and force response of an initially pinned, undeformed droplet undergoing quasi-static deformation, we briefly extend the formulation here to the case where the droplet is not pinned but instead held at the capillary rims by a constant suction pressure, as commonly implemented in the CCFA or microcantilever technique [1, 20]. We show that for the typical range of suction pressures and capillary radii used in the CCFA, the relative change in bridge volume remains confined to within 5% in the small-strain regime. Consequently, the shape-mediated equations governing the force response, bridge mean curvature, and pinning angle—Eqns. (2.7)–(2.9)—remain unchanged from the pinned droplet case, except that the zero-force state bridge radius is now smaller than the undeformed droplet radius, and is selected as the characteristic length scale instead.

Accordingly, the asymptotic analysis in Section 2.3 carries over without modification. Similarly, the curvature of the caps changes due to suction, and hence their profiles also differ. We detail these differences in the discussion that follows.

In this configuration, the droplet is not pinned in its undeformed spherical shape of radius  $R_d$ . Instead, it is held at the capillary rims by maintaining the ambient pressure inside the capillaries at a constant value  $P_c$  that is lower than the ambient pressure  $P_a$  outside. This pressure difference imposes a constant capillary suction pressure  $\Delta P_c = P_a - P_c$  on the droplet caps. As a result, the initial shape of the droplet is no longer a continuous sphere. Rather, it consists of a bridge—formed by truncating a sphere of radius  $R_b \neq R_d$  (noting that a truncated sphere is the only configuration that exerts zero net force on the capillary rim planes)—flanked by left and right caps that no longer belong to the same spherical surface, in contrast to the pinned case ( $P_c = P_a$ ).

We refer to this configuration as the new *zero-force state*, and it is described by the truncated spherical shape:

$$\mathcal{R}_0(\phi) = \frac{R_b \cos\phi}{\mathcal{H}}, \quad z_0(\phi) = -R_b \sin\phi,$$

where  $\phi \in [\pi/2 - \theta_0, \theta_0 - \pi/2]$ , and  $\theta_0$  is the new pinning angle in this zero-force configuration. In this case, the Young–Laplace equation (2.1) continues to govern the shape of both the bridge and the caps as the droplet is displaced. The boundary conditions remain unchanged, and the mean

curvature of the bridge is still given by  $\mathcal{H} = (P - P_a)/(2\gamma)$ —although this value differs from the pinned droplet case due to the altered bridge pressure  $P$ . The curvature of the caps increases to:

$$\mathcal{H}_c = \frac{P - P_c}{2\gamma} = \frac{\Delta P}{2\gamma} + \frac{\Delta P_c}{2\gamma} = \mathcal{H} + \mathcal{H}_s,$$

where  $\Delta P = P - P_a$  is the pressure drop across the bridge, and  $\mathcal{H}_s = \Delta P_c/(2\gamma)$  is the excess mean curvature induced by suction.

Following the above discussion, the parameterized shape of the bridge interface in terms of the tilt angle  $\phi$  remains governed by Eqns. (2.5) and (2.6), and the bridge volume constraint (prior to simplification) remains as given in Eqn. (B.1). The total droplet volume remains  $V_d = 4\pi R_d^3/3$ , as mass conservation holds regardless of the pressure configuration. However, the shapes of the left and right spherical caps must now be obtained by replacing the mean curvature  $\mathcal{H}$  with the cap curvature  $\mathcal{H}_c$  in Eqn. (2.3).

The caps are parameterized over  $\phi \in [\phi_L, \pi/2]$  for the left cap and  $\phi \in [-\pi/2, -\phi_L]$  for the right cap, where the local tilt angle of the left cap at the capillary rim is now given by  $\phi_L = \arccos(\mathcal{H}_c R)$ . Consequently, the complete cap profiles are described by:

$$\mathcal{R}^2 + \left[ z - \left( \pm \frac{L}{2} \mp \left\{ \frac{1}{\mathcal{H}_c^2} - R^2 \right\}^{1/2} \right) \right]^2 = \frac{1}{\mathcal{H}_c^2},$$

for the right and left caps, respectively. Since  $\mathcal{H}_c \geq \mathcal{H}$ , these expressions indicate that the spherical caps possess a higher mean curvature—and therefore a smaller radius—when the suction pressure  $\Delta P_c \neq 0$ , compared to the zero-suction (pinned) case.

Following this formulation, the total cap volume  $2V_c$  is obtained by replacing the bridge mean curvature  $\mathcal{H}$  with the cap curvature  $\mathcal{H}_c$  in the pinned droplet bridge volume expression (B.1). Consequently, the resulting bridge volume becomes:

$$\begin{aligned} V_b &= -\frac{\pi}{4\mathcal{H}^3} \left[ 4 \cos \theta - \frac{4}{3} \cos^3 \theta - 4\mathcal{F} \cos \theta \right. \\ &\quad \left. + \int_0^{\frac{\pi}{2}-\theta} \left\{ 3 \cos^2 \xi (\cos^2 \xi - 4\mathcal{F})^{1/2} + \frac{\cos^4 \xi}{(\cos^2 \xi - 4\mathcal{F})^{1/2}} \right\} d\xi \right] \\ &= \frac{2\pi}{3} \left[ 2R_d^3 - \frac{1}{\mathcal{H}_c^3} (2 - 3 \sin \phi_L + \sin^3 \phi_L) \right], \end{aligned} \quad (\text{B.3})$$

where  $\sin \phi_L = (1 - \mathcal{H}_c^2 R^2)^{1/2}$ . We note that a direct relationship between the radius  $R_b$  of the zero-force spherical bridge and the radius  $R_d$  of the undeformed droplet has not yet been established. Although both quantities can be independently measured in experiments, it is practically useful to express one in terms of the other.

Specifically, if  $R_b$  is known, the zero-force state pinning angle  $\theta_0$  satisfies  $\cos \theta_0 = -\left[1 - (R_b/R)^2\right]^{1/2}$ . Conversely, if  $\theta_0$  is known, then  $R_b = R \csc \theta_0$ . Furthermore, the mean curvature of the caps in the zero-force state is given by  $\mathcal{H}_{c,0} = \mathcal{H}_0 + \mathcal{H}_s = 1/R_b + \mathcal{H}_s$ , from which we can relate the corresponding tilt angle at the left capillary rim by  $\sin \phi_{L,0} = (1 - \mathcal{H}_{c,0}^2 R^2)^{1/2}$ . Substituting  $\mathcal{F} = 0$  into Eqn. (B.3), we arrive at the following expression relating  $R_b$  and  $R_d$ :

$$R_d^3 = \frac{1}{2} \left[ R_b^3 \cos \theta_0 (\cos^2 \theta_0 - 3) + \frac{1}{\mathcal{H}_{c,0}^3} (2 - 3 \sin \phi_{L,0} + \sin^3 \phi_{L,0}) \right]. \quad (\text{B.4})$$

Now, similar to the zero suction pressure case discussed in Appendix B.1, the bridge volume  $V_b$  in Eqn. (B.3) can be rewritten in terms of the cap mean curvature  $\mathcal{H}_c$  and capillary radius  $R$  as:

$$V_b(\mathcal{H}_c, R) = \frac{2\pi}{3} \left[ 2R_d^3 - \frac{1}{\mathcal{H}_c^3} \left\{ 2 - 3(1 - \mathcal{H}_c^2 R^2)^{1/2} + (1 - \mathcal{H}_c^2 R^2)^{3/2} \right\} \right].$$

The zero-force state bridge volume  $V_{b,0}$  is obtained by substituting  $\mathcal{H}_c = \mathcal{H}_{c,0}$  into the above expression, and using the equation for  $R_d^3$  in Eqn. (B.4):

$$V_{b,0} = \frac{2\pi R_b^3}{3} \cos \theta_0 (\cos^2 \theta_0 - 3).$$

This expression allows us to quantify the absolute relative change in bridge volume due to any deviation from the zero-force state as:

$$\left| \frac{\Delta V_b}{V_{b,0}} \right| = \left| 1 - \left[ 2\hat{R}_d^3 - \hat{\mathcal{H}}_c^{-3} \left\{ 2 - 3(1 - \hat{\mathcal{H}}_c^2 \sin^2 \theta_0)^{1/2} + (1 - \hat{\mathcal{H}}_c^2 \sin^2 \theta_0)^{3/2} \right\} \right] \right/ [\cos \theta_0 (\cos^2 \theta_0 - 3)],$$

where  $\hat{R}_d = R_d/R_b$  is the dimensionless undeformed droplet radius, and  $\hat{\mathcal{H}}_c = R_b \mathcal{H}_c = \hat{\mathcal{H}} + \hat{\mathcal{H}}_s$  is the dimensionless cap mean curvature, with  $\hat{\mathcal{H}} = R_b \mathcal{H}$  being the dimensionless bridge mean curvature, and  $\hat{\mathcal{H}}_s = R_b \mathcal{H}_s$  denoting the dimensionless excess mean curvature.

Before proceeding further with our analysis to determine the conditions under which the bridge volume can be assumed to remain approximately constant, we note that the cap mean curvature  $\mathcal{H}_c$  imposes a physical constraint on the maximum suction pressure  $\Delta P_{c,m}$  that can be applied before the droplet is completely drawn into the capillaries. This constraint arises from the requirement that the radius of curvature of the caps,  $1/\mathcal{H}_c$ , must be at least as large as the capillary radius  $R$ , leading to the inequality  $\mathcal{H}_s \leq 1/R - \mathcal{H}$ . Consequently, the maximum allowable suction pressure as a function of the bridge mean curvature is given by  $\Delta P_{c,m} = 2\gamma(1/R - \mathcal{H})$ .

For small dilations from the zero-force state, the mean curvature  $\mathcal{H}$  decreases, and since the suction pressure remains constant throughout, the maximum suction pressure permissible at the zero-force state,  $\Delta P_{c,m} = 2\gamma(1/R - 1/R_b)$ , remains valid for such dilation. On the other hand, during compression, the bridge curvature increases ( $\mathcal{H} > 1/R_b$ ), thereby lowering the allowable suction pressure according to the above constraint. Therefore, to avoid the droplet being completely sucked into the capillaries at any point during the quasi-static deformation in the CCFA, the applied constant suction pressure must be chosen such that it does not exceed the maximum value corresponding to the largest curvature desired during compression. Moreover, for any given bridge mean curvature at the zero-force state and during compression ( $\mathcal{H} \geq 1/R_b$ ), choosing a smaller capillary radius accommodates higher suction pressures by increasing the maximum  $\Delta P_{c,m}$ , while conversely, a larger capillary radius permits only lower suction pressures. Fig. B.2 illustrates this trend at the zero-force state.

The physical constraint  $\mathcal{H}_c R \leq 1$ , analogous to the zero-suction pressure case, imposes a restriction on the allowable capillary radius  $R$ . To elaborate, consider compressing the droplet by a displacement  $\Delta L \leq 0$  and with constant suction pressure  $\Delta P_c$ , such that the bridge attains a mean curvature  $\mathcal{H} \geq 1/R_b$ , where  $R_b$  is the zero-force state bridge radius. Then the capillary radius must satisfy the inequality  $R \leq 1/(\mathcal{H} + \mathcal{H}_s)$  to avoid the droplet being sucked into the capillaries, where  $\mathcal{H}_s = \Delta P_c/(2\gamma)$  is the suction-induced excess mean curvature. Choosing a capillary radius that satisfies this bound ensures that all bridge curvatures attained during compression from the

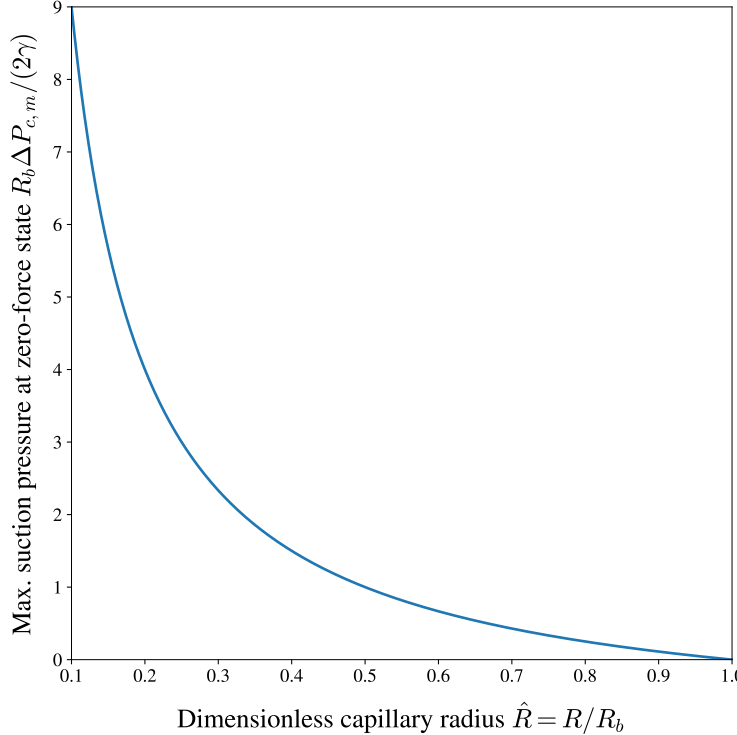


**Figure B.2:** Maximum dimensionless suction pressure (excess mean curvature)  $R_b \Delta P_{c,m} / (2\gamma)$  versus capillary radius  $\hat{R} = R/R_b$ . Here,  $R_b$  is the bridge radius at the zero-force state, and  $\Delta P_{c,m}$  is the maximum suction pressure permitted at the zero-force state beyond which the droplet is completely drawn into the capillaries.

zero-force state to the displacement  $\Delta L$ , as well as any curvature  $\mathcal{H} < 1/R_b$  encountered during small dilations, remain physically realizable.

Therefore, when compression is of primary interest, the capillary radius must satisfy the constraint for the maximum curvature reached at the most compressed state. All smaller curvatures, whether attained during milder compression, at the zero-force state, or during subsequent dilation, will then automatically satisfy the physical constraint. When only dilation is considered, the maximum allowable capillary radius is dictated by the zero-force bridge mean curvature  $\mathcal{H}_0 = 1/R_b$ , and must satisfy  $R \leq 1/(1/R_b + \mathcal{H}_s)$ ; all smaller curvatures  $\mathcal{H} < 1/R_b$  attained during dilation naturally fall within this bound.

These admissibility conditions are illustrated in the percentage relative bridge volume change versus dimensionless capillary radius plots in Fig. B.3, shown for zero suction pressure ( $\hat{\mathcal{H}}_s = 0$ ) and for non-zero suction pressures: a small value  $\hat{\mathcal{H}}_s = 0.05$  [panel (a)], and a value an order of magnitude larger,  $\hat{\mathcal{H}}_s = 0.5$  [panel (b)]. All compression curves ( $\hat{\mathcal{H}} > 1$ ) terminate at the upper bound  $\mathcal{H}_c R = 1$  of the physical regime  $\mathcal{H}_c R \leq 1$ , which reduces to  $\mathcal{H} R \leq 1$  in the zero-suction limit. On the other hand, all dilation curves ( $\hat{\mathcal{H}} < 1$ ) terminate at the upper bound of the zero-force state constraint  $\mathcal{H}_{c,0} R = (1/R_b + \mathcal{H}_s)R \leq 1$ , which simplifies to  $\hat{R} = R/R_d \leq 1$  in the absence of suction pressure and is hence satisfied by all radii.

The inequality  $R \leq 1/(\mathcal{H} + \mathcal{H}_s)$  also implies that accommodating higher bridge curvatures and larger suction pressures necessitates progressively smaller upper bounds on the capillary radius. This means that for a fixed bridge mean curvature, the maximum allowable capillary radius under a non-zero suction pressure is always smaller than that under zero or smaller suction pressures.

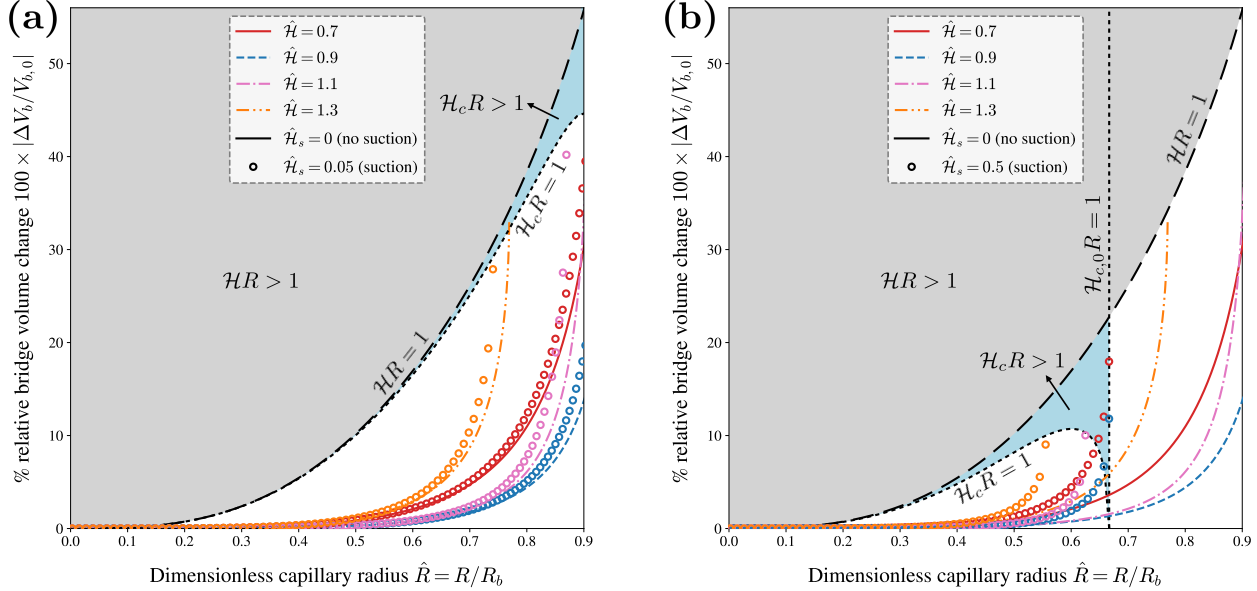


**Figure B.3:** Percentage relative change in bridge volume,  $100 \times |\Delta V_b/V_{b,0}|$ , versus capillary radius  $\hat{R} = R/R_b$  (up to 0.9) for fixed bridge mean curvatures  $\hat{\mathcal{H}} = R_b \mathcal{H} \in \{0.7, 0.9, 1.1, 1.3\}$ , where  $R_b$  is the zero-force state bridge radius. Results are shown for zero suction ( $\hat{\mathcal{H}}_s = 0$ ; *curves with distinct line styles and colours*) and non-zero suction ( $\hat{\mathcal{H}}_s \neq 0$ ; *matching-colour open circles*). Panels: (a)  $\hat{\mathcal{H}}_s = 0.05$ , (b)  $\hat{\mathcal{H}}_s = 0.5$ . All compression curves ( $\hat{\mathcal{H}} > 1$ ) terminate at the upper bound  $\mathcal{H}_c R = 1$  (*short-dashed curved black line*) of the physical regime  $\mathcal{H}_c R \leq 1$ , which reduces to the upper bound  $\mathcal{H}R = 1$  (*long-dashed black line*) in the zero-suction limit. All dilation curves ( $\hat{\mathcal{H}} < 1$ ) terminate at the upper bound  $\mathcal{H}_{c,0} R = 1$  (*short-dashed straight line*) of the zero-force state constraint  $\mathcal{H}_{c,0} R = (1/R_b + \mathcal{H}_s)R \leq 1$ , which simplifies to  $\hat{R} = R/R_d \leq 1$  in the absence of suction and is therefore satisfied by all radii. The *light grey shaded region* denotes the unphysical regime  $\mathcal{H}R > 1$ , while the *sky blue shaded region* corresponds to the unphysical regime  $\mathcal{H}_c R > 1$ .

The inequality also implies that for a fixed suction pressure, increasing the bridge mean curvature leads to a maximum permissible radius that is either unchanged (during dilation) or reduced (during compression). These trends are illustrated in Fig. B.3.

Returning to our discussion of when the bridge volume can be assumed to remain approximately constant, we observe from Fig. B.3 that for any bridge mean curvature  $\hat{\mathcal{H}} \neq 1$  and prescribed suction pressure  $\Delta P_c$  (i.e., a given excess mean curvature  $\hat{\mathcal{H}}_s$ ), the relative change in bridge volume increases monotonically with the capillary radius  $\hat{R}$ , provided the physical constraint  $\hat{\mathcal{H}}_c = \hat{\mathcal{H}} + \hat{\mathcal{H}}_s \leq 1/\hat{R}$  is satisfied. This change vanishes in the limit  $\hat{R} \rightarrow 0$ , implying that, as in the zero-suction pressure case, smaller capillary radii produce smaller deviations in bridge volume. All other conclusions drawn for the zero-suction pressure scenario in Section B.1 remain valid for the non-zero suction pressure case.

However, an important distinction arises due to suction: as the suction pressure increases, the bridge radius at the zero-force state progressively decreases from its maximum value attained at zero suction, while the caps—due to their suction-induced excess curvature—attain a radius even smaller than the bridge and thus penetrate deeper into the capillaries. Consequently, to conserve the droplet volume, the cap volume increases and the bridge volume decreases. For a fixed displacement from the zero-force state, the volume added to (during dilation) or subtracted from (during compression) the bridge by the caps, and thus the total relative bridge volume change, must increase to accommodate the growing curvature mismatch between the bridge and the caps induced by increasing suction. As a result, Fig. B.3 shows that for a given mean curvature and fixed capillary radius (within the

physical regime), the relative bridge volume change increases with suction pressure: the smallest change occurs in the zero-suction case, followed by the case with  $\hat{\mathcal{H}}_s = 0.05$  [panel (a)], and the largest deviation appears in the case with  $\hat{\mathcal{H}}_s = 0.5$  [panel (b)].

Following the above discussion, and as shown in Fig. B.1, if we choose the typical CCFA capillary radius range,  $\hat{R} = R/R_d \in [0.3, 0.6]$ , the relative change in bridge volume remains confined to under 5% for representative small-strain curvatures varying between  $\hat{\mathcal{H}} = 0.7$  (dilation) and  $\hat{\mathcal{H}} = 1.3$  (compression), provided the suction pressure is sufficiently small such that  $\hat{\mathcal{H}}_s \leq 0.5$ , which is typical for the CCFA (for instance, a 50  $\mu\text{m}$  water droplet in an oil bath with interfacial tension  $\gamma = 50 \text{ mN}$  held at the capillary rims with suction pressure  $\Delta P_c = 500 \text{ Pa}$  admits  $\hat{\mathcal{H}}_s = 0.5$ ). Therefore, under these conditions, we can safely assume that the bridge volume remains approximately constant throughout the quasi-static deformation of the droplet in the CCFA, with the contact lines fixed at the capillary rims by suction pressure rather than by pinning.

As a result, in this small-strain and small-suction-pressure limit, the bridge volume constraint (B.3) simplifies to:

$$\begin{aligned} V_b &= -\frac{\pi}{4\mathcal{H}^3} \left[ 4\cos\theta - \frac{4}{3}\cos^3\theta - 4\mathcal{F}\cos\theta \right. \\ &\quad \left. + \int_0^{\frac{\pi}{2}-\theta} \left\{ 3\cos^2\xi (\cos^2\xi - 4\mathcal{F})^{1/2} + \frac{\cos^4\xi}{(\cos^2\xi - 4\mathcal{F})^{1/2}} \right\} d\xi \right] \\ &= V_{b,0} = \frac{2\pi R_b^3}{3} \cos\theta_0 (\cos^2\theta_0 - 3), \end{aligned} \quad (\text{B.5})$$

where  $R_b$  is the bridge radius at the zero-force state. However, for larger suction pressures, the relative volume change can no longer be considered negligible. In such cases, the assumption of bridge volume constancy breaks down, and the full bridge volume constraint (B.3)—which only considers the fact that the total droplet volume remains constant—must be used in subsequent analysis.